Strain Heterogeneity in the Anterior Cruciate Ligament and Constitutive Modeling with Full-Field Methods

by

Callan M. Luetkemeyer

A dissertation submitted in partial fulfillment
of the requirements for the degree of
Doctor of Philosophy
(Mechanical Engineering)
in The University of Michigan
2020

Doctoral Committee:

Professor Ellen Arruda, Chair
Professor James Ashton-Miller
Professor John Shaw
Professor Michael Thouless
Professor Alan Wineman

Callan M. Luetkemeyer

cmluetke@umich.edu

Orcid ID: 0000-0002-5632-3656

For my grandparents, whose resilience and benevolence will forever be my inspiration.

ACKNOWLEDGEMENTS

This research was generously supported by the National Science Foundation (NSF GRFP No. 1256260 and grant No. 1537711), the Bob and Betty Beyster Foundation (J. Robert Beyster Computational Innovation Graduate Fellowship), and the University of Michigan Rackham Graduate School (Rackham Merit Fellowship).

Numerous people in my professional and personal life supported, encouraged, and taught me over the course of my graduate studies, and for that, I am tremendously grateful. I especially thank my advisor, Dr. Ellen Arruda, whose support, guidance, and expertise have been crucial to this work. Ellen is a renowned researcher, but she is also a great leader. She demands excellence, but not conformity, empowering her students to find independent success. The freedom to pursue many of my own (somewhat high-risk) ideas helped me develop creativity and independence, and most importantly, gave me confidence in my own ability and vision. I am forever grateful for the many technical and non-technical skills that Ellen taught me.

I consider myself to be extremely fortunate to have been taught and shaped by several other great researchers: Drs. Alan Wineman, Michael Thouless, James Ashton-Miller, and Edward Wojtys. The diversity of thought offered by this group of people provided me with a unique set of skills and perspective.

I especially want to thank my colleagues/co-authors who made significant contirubtions to this work and to my development as a scientist: Ulrich Scheven, Jon Estrada, Benjamin Marchi, and Ryan Rosario. The quality of this work is largely attributed to their expertise and collaborative effort, and I am tremendously grateful for all that these four colleagues taught me, both personally and professionally.

I also want to thank my colleagues who have taught me many invaluable lessons,

both technical and non-technical: Marie Rice, Aritra Sasmal, Rachel Vitali, Alison Hake, James Gorman, Kaitlyn Mallett, Michael Kimiecik, Will LePage, Dandan Wang, Isha Gupta, and Michael Quann.

The first full-volume displacement data in Chapter 3 was a foundational part of this dissertation. It was made possible by a collaboration with Corey Neu and Luyao Cai, to whom I am forever grateful for generously sharing their equipment, expertise, and time. Their support played a critical role in my success.

I'd also like to express the deep gratitude I have for Andy Poli for his unwavering support and encouragement. His mastery of experimental mechanics and engineering science, his can-do attitude, and his willingness to go out of his way to help people is what makes him a personal role model of mine, both as a scientist and a person.

Many undergraduates worked on small projects under my supervision, and I am grateful for their enthusiasm and effort. They taught me how to lead. In particular, I'd like to thank Jack Weeks, who made significant contributions to my work.

I also sincerely thank all of the faculty and staff who shared their suggestions and expertise and provided support, including Dr. John Shaw, Dr. Rhima Coleman, Dr. Joan Greve, John Laidlaw, and Kent Pruss.

I'd be remiss if I did not also thank my mentors who have supported me since I was an undergraduate student, especially Drs. Jessica Wagenseil, Gary Bledsoe, Scott Sell, and Cecil Thomas. Their encouragement and influence are the reason I pursued a graduate degree, and for that, I am deeply grateful.

My father, Brice, mother, Beverly, my brother and sister-in-law, CJ and Jessica, and close family friend, Rachel, have been incredibly supportive of my endeavor, despite it causing my absence from many family gatherings and celebrations over the years. I am thankful for their patience, encouragement, and love. I especially thank my mother for proofreading countless abstracts, even though my work is certainly not her favorite genre to read.

Finally, I am most grateful for the love and support that my fiancé, Zachary, has given me throughout my time as a graduate student. Thank you, Zach, for supporting me and my work. Thank you for making me laugh. Thank you for inspiring me to be a better version of myself. Thank you for being my best friend.

PREFACE

Chapters 2-5 have been written as separate manuscripts. For this reason, there is some repetition of information, particularly in the motivating material, as well as small discrepancies in mathematical notations.

TABLE OF CONTENTS

LIST OF FIGURES

Figure

LIST OF TABLES

Table

LIST OF APPENDICES

Appendix

ABSTRACT

Anterior cruciate ligament (ACL) injury rates are rising, particularly for women and young people. These injuries are debilitative; they typically require surgical reconstruction and lead to osteoarthritis within ten years. Still, there is little consensus about what puts someone at risk for an ACL injury, and this knowledge is critical to the development of injury prevention strategies. Finite element models provide an effective platform for systemically determining the effect of proposed injury risk factors on ACL strain concentrations, and thus, determining whether they predispose an individual to injury. However, the accuracy of a finite element model relies on the accuracy of the material models used in its construction.

Initially, I examined how the shape of the ligament-bone attachment (enthesis) might affect injury risk. Two factors were found to increase effective strain concentrations: more acute attachment angles and more concave enthesis shapes, both of which are more common in women. However, I also discovered that enthesis shape significantly affects the macroscopic (global) mechanical response of the model ligament. As such, I concluded that enthesis geometry (and the deformation heterogeneity it creates) would need to be considered in the construction of material models.

I also explored the effect of collagen fiber splay (material direction heterogeneity) on the macroscopic mechanical response of the ACL bundles and the patellar tendon (PT), a commonly used graft for ACL reconstruction. Using analytical, computational, and experimental approaches, results clearly demonstrate that splay geometry significantly affects the macroscopic mechanical response of ligaments. Since material properties are, by definition, independent of geometry, this indicates fiber splay is a structural property that prevents the identification of true material properties with standard modeling techniques.

Hence, in the finale of this work, I used displacement-encoded magnetic resonance

imaging (MRI) to measure full-volume deformation fields of the ovine PT and both ACL bundles under tension. I then employed the virtual fields method (VFM) – a full-field inverse method – to calibrate material models with this data, accounting for strain heterogeneity, material direction heterogeneity (fiber splay), and enthesis shape. Most constitutive parameters were consistent among all specimen groups, demonstrating the universality of ligament material constituents. A material parameter describing the degree of anisotropy, or collagen fiber alignment, however, showed statistically significant differences between groups. It indicated that collagen fibers in the anteromedial (AM) bundle of the ACL were significantly more aligned than those in the posterolateral (PL), which is congruent with optical measurements. My work demonstrates that (when strain heterogeneity and structural properties are accounted for) ligament material microstructure is detectable with measures of mechanical function.

CHAPTER 1

Introduction

1.1 Motivation

1.1.1 The consequences of ACL injury

The anterior cruciate ligament (ACL) is the most commonly injured knee ligament, affecting more than 200,000 people each year in the United States alone. ACL injuries often occur during non-contact athletic maneuvers such as cutting or jumping, which contributes to the particularly high rates of ACL injury incidence in soccer, basketball, football, lacrosse, and alpine skiing [2, 124]. ACL tears are painful, debilitating, and costly, in terms of both their short-term and long-term consequences.

Due to its avascularity and low cellularity, the ACL has very limited ability to heal, and the body cannot repair its functionality following a complete tear. At the same time, the ACL is a crucial mechanical structure that provides the knee with stability and facilitates movement. Thus, ACL reconstruction surgery is generally considered the best treatment option for an ACL injury, particularly for those interested in resuming a high or moderate level of physical activity. ACL deficient patients who choose non-surgical treatments consistently report more dissatisfaction with knee function and lower quality of life compared to those who opt for ACL reconstruction surgery [10]. Surgical reconstruction of the ACL involves removal of the torn ACL and replacement with a graft material (shown in Fig. 1.1), which,

depending on the surgeon, is most commonly a section of the patient's own patellar tendon (PT) or hamstrings tendon, or a cadaver ACL.

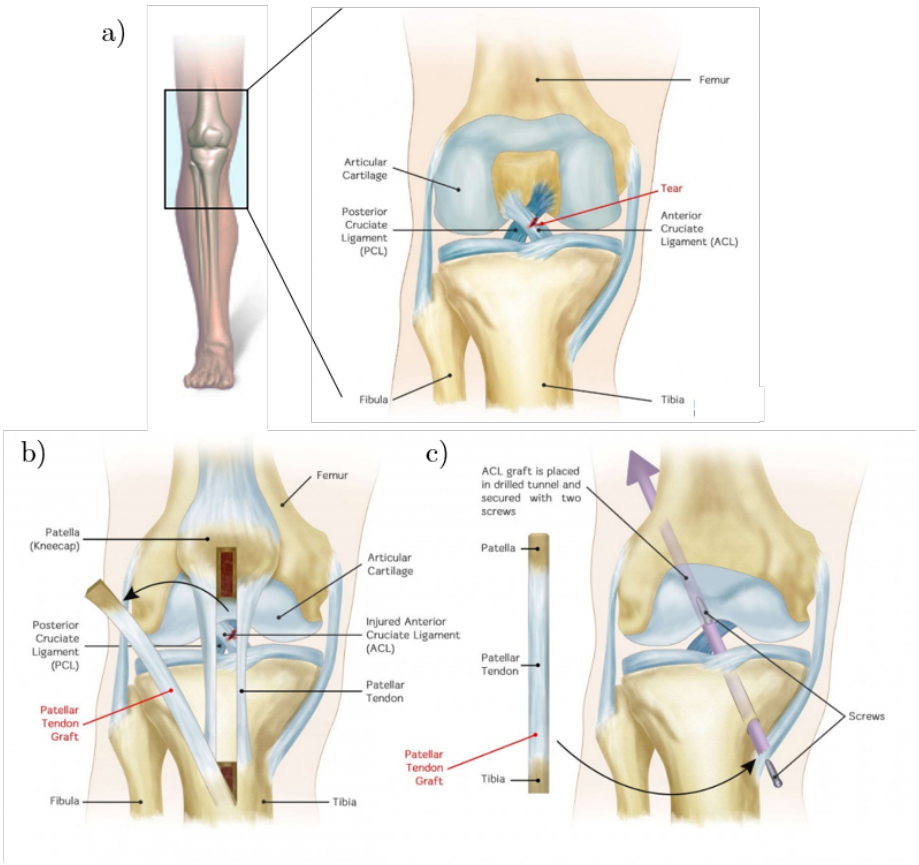

Figure 1.1: The ACL is a commonly injured ligament in the center of the knee (a). Surgical reconstruction of the ACL using a patellar tendon (PT) graft involves removing the center third of the patient's own PT (b), suturing the two remaining thirds together, drilling bone tunnels through the femur and tibia, and replacing the torn ACL by securing the PT graft in the bone tunnels (c). Images are reproduced with permission from `rehabmypatient.com`.

However, within 15 years of ACL reconstruction, approximately 10% of patients will experience reinjury of their ACL grafts and 15% will tear their contralateral ACL [27, 89]. Moreover, while 93% of those undergoing ACL reconstruction surgery attempt to return to their sport, less than half return to playing at their pre-injury

level 2-7 years after surgery [11]. It is believed that this poor rate of return to sport contributes to the increased rate of clinical depression following ACL injury [12].

Furthermore, medical expenses for treatment of a single ACL injury average more than $15,000. Thus, medical care for ACL injuries is a major contributor to the $170 billion spent on treatment of musculoskeletal problems in the United States every year, second only to circulatory conditions and basic care [67].

In addition to these immediate consequences of injury, the long-term consequences are arguably more troublesome. The majority of individuals with an ACL injury will develop knee osteoarthritis (OA) and associated chronic knee pain within 10-20 years [91, 113]. The biochemical changes causing this cartilage degeneration are detectable within just 18 months of an ACL injury [119].

For a young person, an ACL injury means more than just the end of an athletic career, a painful surgery, and large medical bills; it typically means altered knee function and chronic knee pain from OA, permanently impacting his/her mobility and quality of life. Hence, a considerable amount of research has been dedicated to the development of strategies for ACL injury prevention. Meanwhile, these injuries are becoming increasingly common.

1.1.2 ACL injury prevalence

Despite efforts to develop injury prevention measures, the rate of ACL injuries continues to rise, particularly for children and females. While the majority of ACL tears affect adults aged 20 and over, more than a quarter of ACL injuries in the United States affect adolescents, ages 15 to 19. Especially troublesome is the particularly large increase in ACL injury rates for 10-19 year old girls (5% per year) and 5-9 year old girls (7% per year), compared with their male counterparts (3% and 0% per year, respectively) [158].

Furthermore, the consistent increase in the rate of ACL tears – especially among young people – extends beyond America, making it an international problem [139]. The rate of ACL reconstruction surgeries is rising for Australian children, with a 9% per year increase in girls and 8% per year increase in boys (ages 5-14) from 2000 to

2015 [164]. Similarly, between 1997 and 2014, Finland saw a 59% increase in ACL tears for 13-15 year old boys, 81% increase for 16-17 year old girls, and an astonishing 143% increase for 13-15 year old girls (an average of 8% per year) [157].

1.1.3 Risk factors for ACL injury

Risk factors are anatomical features or kinematic tendencies which increase an individual's susceptibility to ACL injury. Many injury prevention efforts aim to develop strategies to modify risk factors and thus, decrease injury risk [4]. Thus, a large number of studies dedicated to the identification of risk factors have been published in the literature, most of which search for correlations between injury prevalence and anatomical or kinematic measurements. For example, anatomical features such steeper posterolateral tibial slope and smaller intercondylar notch width have been found by a number of studies to exhibit a positive correlation with ACL injury incidence [22, 26, 62, 114, 146, 159]. Similarly, the tendency to use more valgus loading (e.g. larger knee abduction loads) during athletic maneuvers has been correlated with ACL injury [68]. Neuromuscular training programs can aim to retrain athletes to use kinematics that are less likely to cause injury [4], and it is possible that some less advantageous anatomical features may be modified using warm-up exercises that stimulate bone remodeling to create a less injury-prone anatomy [108].

Still, the most cogent risk factors for ACL injury remain unclear. Several studies have reported conflicting evidence, finding no correlation between previously reported factors of interest and injury prevalence [5, 92, 154, 156]. Moreover, while correlations are a powerful statistics tool, they do not imply causation. The factors which directly cause increased ACL injury risk must have a mechanistic underpinning.

Clinical and experimental studies on the ACL are limited in their ability to probe the effect of particular variables and hold others fixed; computational methods, however, excel at this task. Finite element (FE) modeling provides a systematic and deterministic way to assess how changes in a single potential risk factor affect mechanical strain concentrations in the ACL [94, 98, 121], and thus, might predispose an individual to injury. To construct these models, an understanding of knee anatomy,

ACL structure and function, and theory involving large deformations of solid materials is required.

1.2 Background

1.2.1 ACL anatomy and function

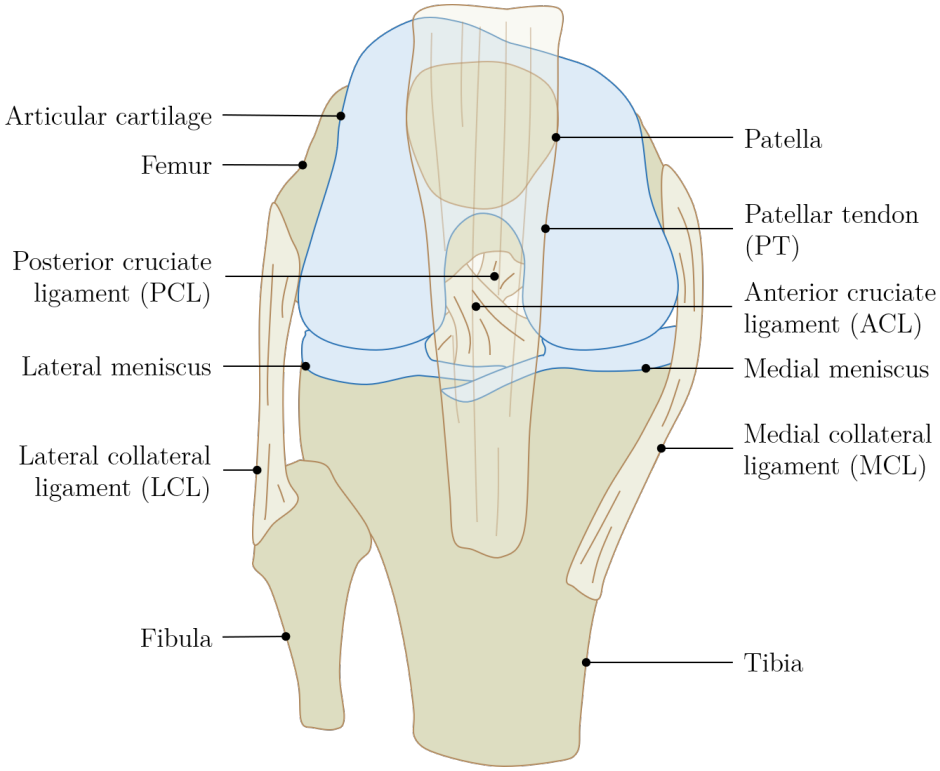

Figure 1.2: Soft tissues in the (right) knee include the ACL, posterior cruciate ligament, medial and lateral collateral ligaments, patellar tendon (ligament), and menisci.

The ACL is located in the center of the knee joint, attaching the central anterior (front) edge of the tibia (shin bone) to the medial (towards the person's center-line) edge of the lateral (away from the person's center-line) condyle of the femur (thigh bone), as shown in Fig. 1.2. It works in conjunction with the posterior cruciate

ligament, medial and lateral collateral ligaments, menisci, and patellar tendon to provide the knee with both rotational flexibility about its primary rotational axis (pitch) and stability to limit all translation freedom and rotational freedom about the orthogonal axes (yaw and roll). The collateral ligaments on the medial and lateral sides of the knee are positioned to primarily withstand moments that create roll as well as distal (away from the person's core) and medial/lateral translations of tibia relative to the femur. The ACL and PCL restrict yaw, or internal and external rotations of the tibia with respect to the femur, in addition to anterior and posterior translations of the tibia, respectively.

Therefore, the ACL serves two main functions: prevent excessive anterior tibial translations and internal tibial rotations. It is believed that this duality of function is the reason for the ACL's double bundle structure. The anteromedial (AM) bundle of the ACL is thought to primarily function to restrict anterior tibial translation, while the posterolateral (PL) bundle prevents tibial rotation [7].

To achieve their different tasks, the AM and PL bundle differ in size, orientation, and structure (see Fig. 1.4). The AM bundle is longer, and it wraps around the PL bundle to attach at a more anterior location on the tibia and more posterior (back of the knee) location on the femur, giving it a better angle to prevent tibial translation. The PL twists about its own axis, which increases its effective torsional stiffness to prevent internal tibial rotation [7]. Both bundles are are composed of the same material constituents, or extracellular matrix (ECM) components.

1.2.2 The extracellular matrix

The ECM is what provides all tissues with mechanical integrity. In ligaments and tendons, collagen accounts for 60-85% of the dry tissue weight [82]. Most of that collagen is type-I collagen, which is organized into fibers that are highly aligned along the primary direction of loading. Collagen is a hierarchical material, built from collagen triple helix molecules organized into collagen fibrils with a staggered design that gives rise to a consistent pattern known as D-spacing [51]. Collagen fibrils are grouped together to form collagen fibers, which are the primary load-bearing ECM

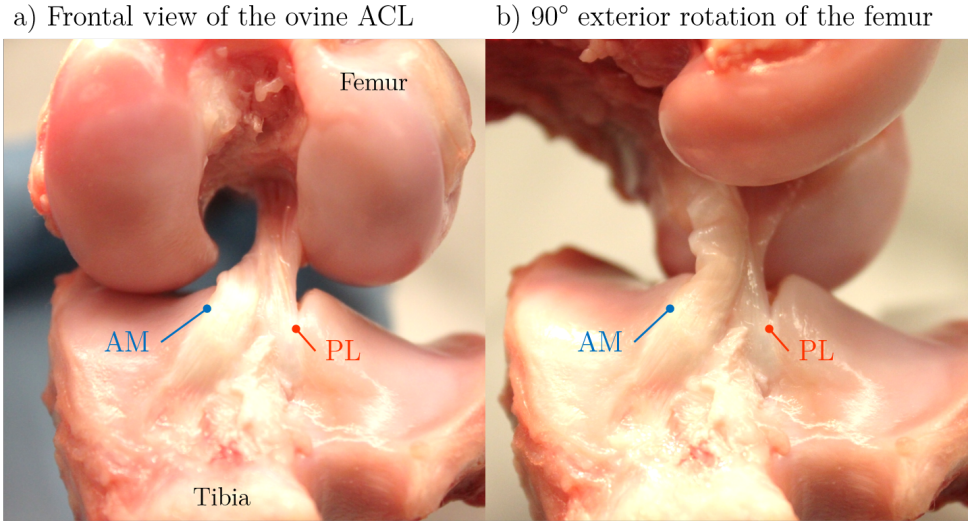

Figure 1.3: The double bundle anatomy of the ACL is shown with a anterior view of a left ovine knee (all soft tissues except the ACL have been removed). In a physiologic orientation (a), the AM bundle attaches to the tibia at a more anterior and medial position than the PL bundle, and it wraps around the PL bundle to attach to the femur at a more posterior location than the PL bundle. When the femur is turned 90°to the tibia (b), this double bundle structure becomes more apparent.

component in ligaments and tendons, as depicted in Fig. 1.5.

Collagen fibers insert directly into bone at an enthesis, a ∼1 mm region over which the ECM transitions from ligament to bone. Ligament and bone are two dissimilar materials: ligament is compliant and tough, bone is stiff and brittle. Connecting two dissimilar materials is a classically difficult engineering problem, as stress concentrations inevitably form at the junction. To mitigate this problem, the enthesis is a functionally graded material, meaning its material properties continuously change, becoming increasingly stiff as it attaches ligament to bone, as shown in Fig. 1.6. The increased stiffness is achieved with continuous changes in the non-collagenous ECM components.

Non-collagenous components include other protein structures like proteoglycans (PGs) and elastic fibers. Decorin and glycosaminoglycans are small leucine-rich PGs, thought to facilitate load transfer between neighboring type-I collagen fibers, while

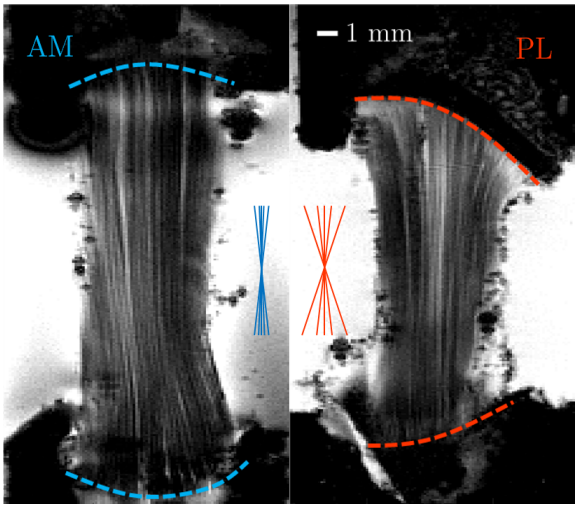

Figure 1.4: High-resolution MRI images of the two bundles (or regions) of the ACL demonstrate the similarities and differences. Both bundles are composed of highly aligned collagen fibers (seen here as dark vertical strands) which spread or splay near the attachment to bone (enthesis), emphasized with dotted lines. However, the AM bundle is considerably longer than the PL, and the bundles have differently shaped entheses. Studies on the microstructure of the bundles show that at a material point, collagen fibers in the PL bundle tend to have more variation about the mean fiber direction than those in the AM bundle. The accompanying symbols represent this difference in the degree of collagen fiber alignment.

large aggregating PGs like versican and aggrecan are hydrophilic molecules that increase water content, providing resistance to compression [129, 135, 150]. Elastic fibers, composed of the proteins elastin and fibrillin, constitute ∼2% of the dry weight [66, 82, 135]. It has been estimated that elastic fibers support as much as 70% of shear stress and tensile stress transverse to the collagen fibers [66].

It is also thought that a naturally occurring, small amount of pre-tension in elastic fibers creates collagen fiber crimp, shown in Fig. 1.7. Collagen fibers display tension-compression asymmetry, exhibiting almost no resistance to compression. Thus, slightly-tensioned elastic fibers hold collagen fibers in a buckled state when the tissue is unloaded [43]. The initial distribution of crimped states is believed to be the source of much of the non-linearity in the material's mechanical response in

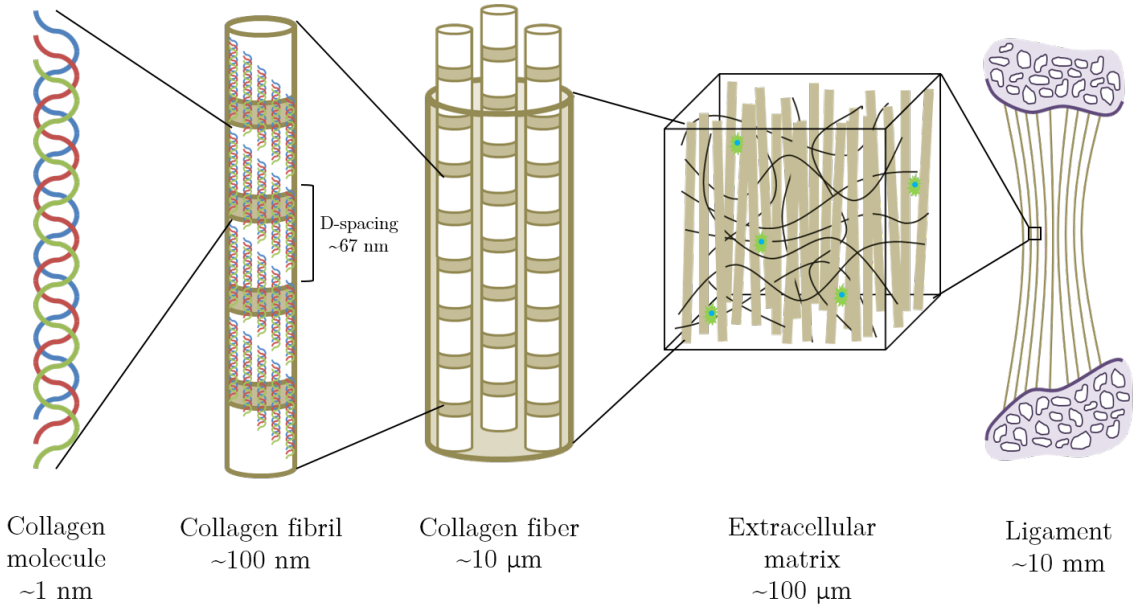

Figure 1.5: Ligament ECM is largely comprised of elastic fibers (depicted with wavy black lines), and highly-aligned type-I collagen, a hierarchical protein. Collagen molecules form collagen fibrils, which form collagen fibers, which form collagen fascicles or whole tendons/ligaments.

the collagen fiber direction [160], as explained in Fig. 1.8.

1.2.3 Computational modeling of the ACL

With such complicated anatomy, using analytical mechanical models to study the ACL would require vast simplifications. Using computational tools like the finite element method (FEM), however, the complex geometry and material behavior that emerges from the ECM can be considered. In the FEM, a 3D shape is approximated using a finite number of simple shapes, or elements, which are connected at corners called nodes (see Fig. 1.9). This process is referred to as discretisation. The differential equations governing the displacements across each element are approximated using combinations of simpler equations, or shape functions. The assembly of these shape functions over all elements create a system of equations that models the entire domain. The system is solved using variational methods to find the solution that

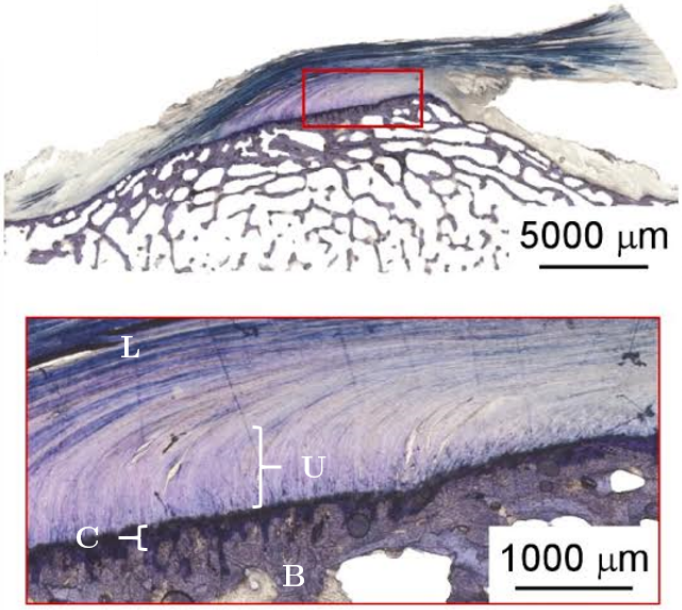

Figure 1.6: The enthesis is a ∼1 mm transition zone between ligament and bone. The non-collageneous ECM increasingly stiffens as the ligament proper (L) transitions into uncalcified fibrocartilage (U), then to calcified cartilage (C) before becoming bone (B). This image was created using standard histological techniques with a toluidine blue stain, which highlights proteoglycan content [18], courtesy of Mélanie Beaulieu.

minimizes an error function, i.e., best approximates equilibrium. The stress or deformation fields computed can be analyzed to determine concentrations where the material is likely to fail.

1.2.4 Material modeling of ligaments

In a FE model, each element must be assigned a constitutive model which describes the material's stress-deformation relationship. For ligaments, these equations can include non-linearity, anisotropy, and viscoelasticity. The ECM is largely comprised of protein fibers, which are polymeric and give rise to stress-deformation non-linearity. Moreover, type-I collagen fibers are very stiff in comparison to other ECM components and they are highly aligned in one direction. This creates mate-

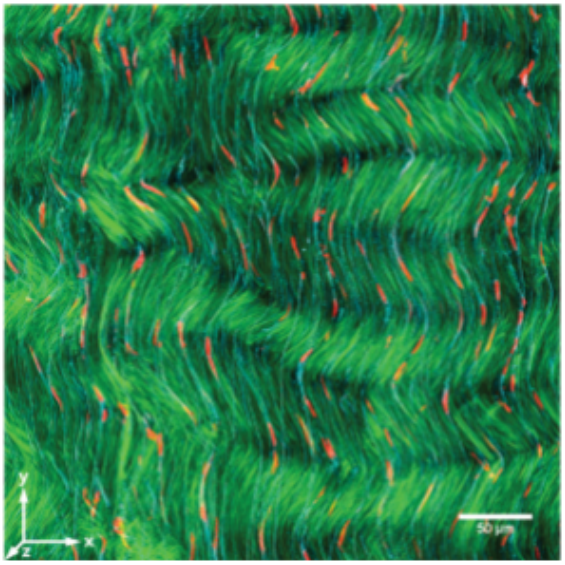

Figure 1.7: Collagen fibers exhibit a small amount of waviness, or crimp, in a ligament or tendon's unloaded state, which thought to be the result of slight pre-tensioning in the elastic fibers. This image of a rabbit Achilles tendon ECM was created using both confocal fluorescence and second harmonic generation imaging by Pang et al. [118], where collagen is shown in green, elastin in cyan, and cells in red. Reproduced with permission under license number 4795361355630.

rial anisotropy (specifically, transverse isotropy), meaning ligaments are stiffer when stretched in the direction of the collagen fibers than in other directions. Finally, the polymeric structure and large water content in ligaments and tendons result in viscoelastic, or time-dependent, material behavior. This work only considers the nonlinear and anisotropic aspects of the material behavior of the ACL. Viscoelasticity will be considered in future work.

1.3 Specific aims

The aims of this research changed with each successive chapter, as findings both invalidated past assumptions and inspired new understanding. My long-term goal has consistently been to aid the development of ACL injury prevention strategies by

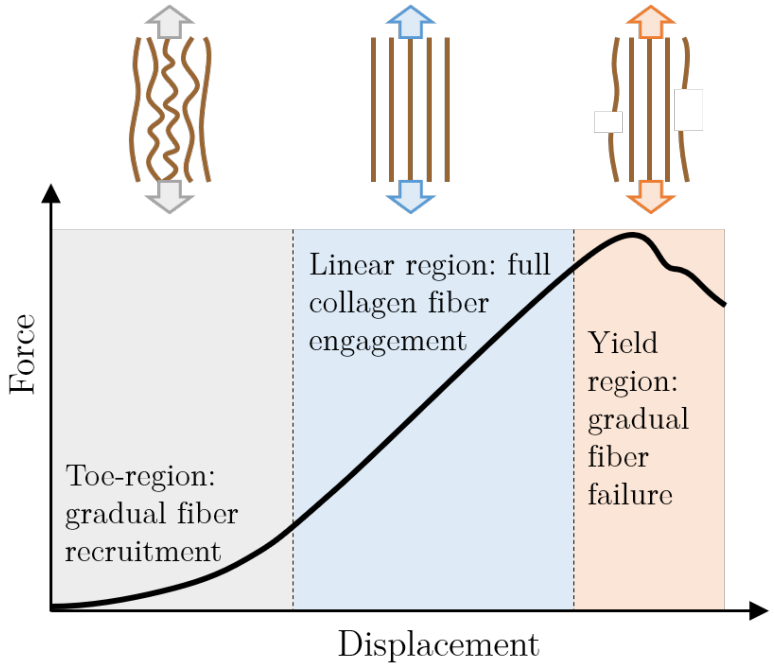

Figure 1.8: Collagen fibers in tendons and ligaments display a distribution of levels of fiber crimp in the unloaded tissue configuration, which gives rise to the material's non-linear force-displacement relationship when pulled in the collagen fiber direction. The initial shape of the curve is concave up, as more and more collagen fibers become uncrimped and begin to resist deformation; this part of the response is referred to as the toe-region. Once all collagen fibers are engaged, the response often appears nearly linear. Finally, if the tissue continues to stretch, the most stretched fibers will fail.

identifying features which increase susceptibility to injury. In the work presented in Chapter 2, I seek to use computational mechanics models to assess whether certain femoral enthesis shapes and/or attachment angles (within the variation seen in the human population) [21] could be ACL injury risk factors. In addition to finding answers to the intended research question, unintended findings were made. First, that the material models used are inadequately calibrated. Second, enthesis geometry is likely one cause of this inefficacy.

Previous modeling methods assumed that ACL bundles loaded uniaxially in

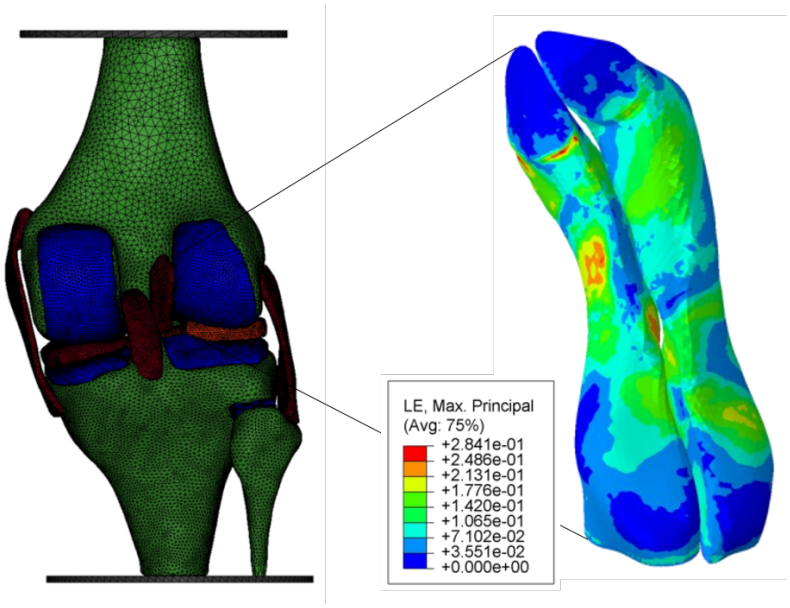

Figure 1.9: Whole-knee FE models like this one can be used to study how changes in knee loading, ACL geometry, or changes in other soft tissues affect stress and deformation concentrations in the ACL bundles. This is achieved with discretisation (breaking the complicated geometries up into a finite number of smaller, simpler shapes, or elements) and numerical approximations. This image is adapted, with permission, from Marchi [98].

a laboratory setting undergo homogeneous (or nearly homogeneous) deformation. However, results shown in Chapter 2 demonstrate that even small differences in attachment shape can have notable effects on the global mechanical response through significant strain heterogeneity. In Chapter 3, strain field heterogeneity is measured throughout the volume of uniaxially loaded ovine AM and PL bundles of the ACL using displacements under applied loading by magnetic resonance imaging (dualMRI). Results demonstrate that certain regions undergo large shear and transverse strains, in addition to inhomogeneous axial strains, indicating that the assumption of homogeneous uniaxial strain is invalid. Additionally, transverse strains in the thickest dimension were largely positive, rather than negative as one would expect in a uniaxial tension test, due to the Poisson effect. This lateral expansion is likely due to fiber splay, the tendency of collagen fibers to spread out as they insert into the bone

(see Fig. 1.4).

Thus, in Chapter 4, I investigated the effect of fiber splay on global force-displacement measurements with a combination of analytical, experimental, and computational methods. Results demonstrate that fiber splay significantly influences the global mechanical response, and thus, must be taken into account when calibrating material models for ligaments.

In order to obtain reliable results about ACL injury risk from computational models, it is clear that better material models of the ACL are needed. However, strain homogeneity is practically impossible to obtain in the ACL, and standard material modeling methods are unable to account for strain heterogeneity and the structural features that create it. Therefore, Chapter 5 discusses the finale of this work: I demonstrate how to build constitutive models for the ACL bundles and patellar tendon using full-field imaging and inverse methods to account for enthesis geometry and fiber splay.

CHAPTER 2

Femoral Entheseal Shape and Attachment Angle as Potential Risk Factors for Anterior Cruciate Ligament Injury

This chapter has been previously published and is used with permission from Elsevier. It may referenced as:

Luetkemeyer, Callan M., Benjamin C. Marchi, James A. Ashton-Miller, and Ellen M. Arruda. Femoral entheseal shape and attachment angle as potential risk factors for anterior cruciate ligament injury. *Journal of the Mechanical Behavior of Biomedical Materials* 88: 313-321, 2018.

2.1 Introduction

Anterior cruciate ligament (ACL) tears are the most common knee ligament injury, occurring more than 250,000 times per year in the United States [58, 143]. Complete tears of the ACL often require surgical reconstruction and increase the susceptibility to knee osteoarthritis within 10 years of the injury [80, 91]. These injuries are especially common in female athletes, who are two to five times more likely to sustain an ACL tear than their male counterparts [68, 148].

There has been considerable interest in determining anatomical features that increase an athlete's risk of ACL injury. Several morphological characteristics have

been correlated with ACL injury, such as steeper posterior tibial slope in the lateral tibial plateau [22, 62, 138, 146] and smaller intercondylar notch width [138, 146, 159]. It has also been proposed that smaller cross-sectional area of the ACL is to blame for the increased injury rate of females compared to males [8, 38]. However, to the authors' knowledge, no statistically significant correlation has been found between cross-sectional area and injury risk. Additionally, while these correlations might prove useful, they lack a mechanical analysis that supports their direct causation of ACL injury.

Clinically, the most common location for an ACL tear is at or near the femoral insertion [163]. The reasons for this region's susceptibility are not yet fully understood. Nevertheless, *in vitro* experimental studies have demonstrated that the ACL is particularly prone to failure at the femoral enthesis, especially in the posterolateral (PL) bundle [20, 90, 107].

Recently, Beaulieu et al. [21] identified six main categories of human femoral entheses by the shape of their tidemarks on standardized histological sections (see Fig. 2.1). Beaulieu et al. [19] also quantified the angle of attachment of the ACL as it arises from lateral femoral epicondyle. The data from that study indicated that, at 15°of knee flexion, male specimens, on average, have a larger attachment angle than their female counterparts; the average male attachment angle was roughly 13°while the average female attachment angle was just 7°. At the present time, the extent to which the femoral entheseal shape and attachment angle affect ACL stress and strain concentration are unknown.

Therefore, the goals of this study were: (1) to use data from the histological studies performed by Beaulieu and colleagues to inform the development of biomechanical models of the ACL femoral attachment, and (2) to examine the differences in strain distribution among the characteristic tidemark profiles in order to determine whether particular profiles may be more prone to injury than others. A simplified 2D analytical model was constructed, followed by a 3D finite model with similar geometry. Three constitutive models were fit to longitudinal and transverse tensile test data from the literature. Results from all models suggest that a concave enthesis and smaller (more acute) attachment angle increase the strain concentration near the

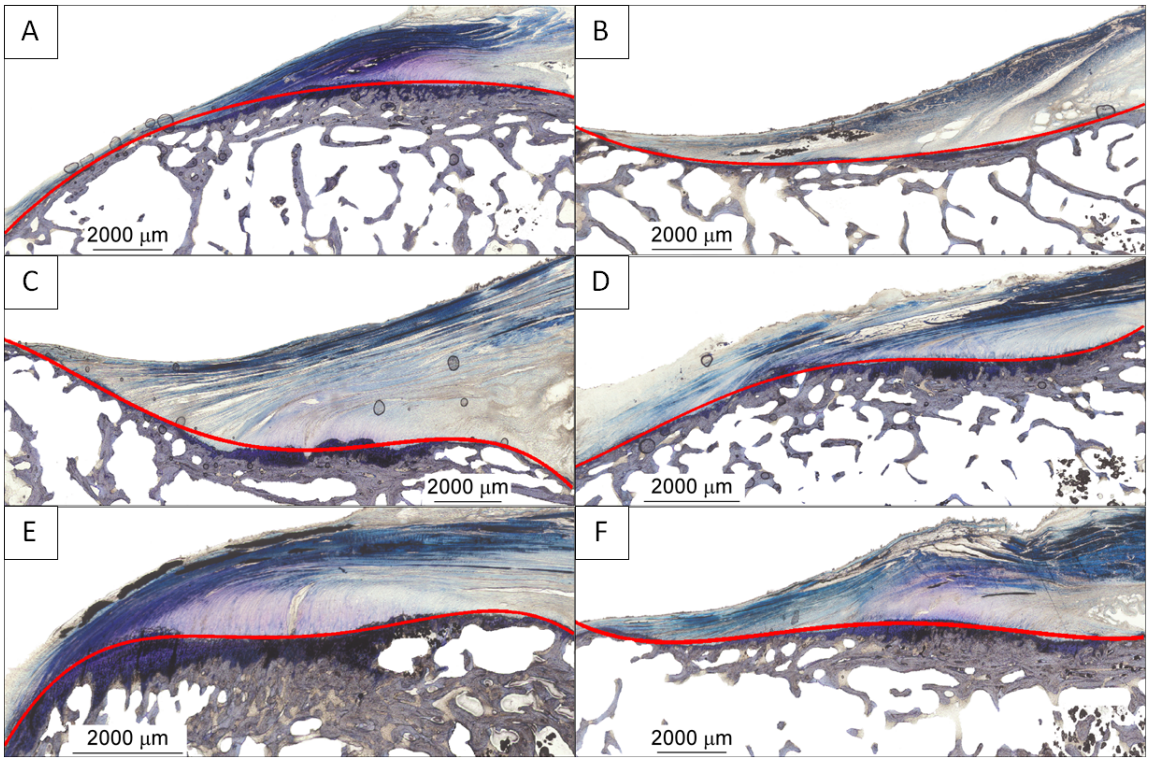

Figure 2.1: Human ACL femoral entheseal profile categories include second order convex (A), second order concave (B), third order convex (C), third order concave (D), fourth order convex (E) and fourth order concave (F) polynomial fits. Note that the shapes are classified as convex or concave with respect to the bone in the distal half. In each panel, the proximal end of the enthesis is shown at left, while the distal end is shown at right. Reproduced from Fig. 3 in Beaulieu et al. [21], used under `https://creativecommons.org/ licenses/by/4.0/legalcode`. Lower two rows of panels have been exchanged.

distal edge of the femoral ACL attachment, increasing injury risk. Additional analysis demonstrates that the macroscopic force-extension relationship of the structure is dependent both on the enthesis geometry as well as the constitutive form.

2.2 Methods

2.2.1 Analytical model formulation

The ACL femoral enthesis was first modeled as a 2D trapezoidal body of width w rigidly attached to a fixed curve, $y = A(x)$. This curve characterized the entheseal shape at the junction of the calcified and uncalcified fibrocartilage, and it had a mean slope of a/w, such that the insertion angle of the enthesis (ϕ) was 13°or 7°, the average attachment angle for males and females, respectively. Entheseal profiles were constructed from histological slices following the grouping scheme shown in Fig. 2.1. The opposite edge of the body ($y = L$) represented the ligament proper, which was assumed to undergo a uniform displacement δ. Fig. 2.2 depicts the variables used in creating the model.

Assuming homogeneity and no Poisson effect, the displacement field in the ligament can be approximated by

$$u_y(x, y) = \frac{\delta}{L - A(x)} (y - A(x)). \tag{2.1}$$

From the representative histological slices shown in Fig. 2.1, analytic expressions for entheseal profiles, $y = A(x)$, were constructed. Each of the entheseal profiles, described by $y = A(x)$, was assumed to have one of the following forms based on its corresponding category in Fig. 2.1:

$$A_{A,B}(x) = \frac{a}{w}x \pm \left(x^2 - wx\right), \tag{2.2}$$

$$A_{C,D}(x) = \frac{a}{w}x \pm \left(2x^3 - 3wx^2 + w^2x\right), \tag{2.3}$$

or

$$A_{E,F}(x) = \frac{a}{w}x \pm \left(4x^4 - 8wx^3 + 5w^2x^2 - w^3x\right). \tag{2.4}$$

The nonlinear terms in parentheses were added to give concave enthesis shapes and subtracted to yield convex shapes (with respect to the bone). Additionally, a linear

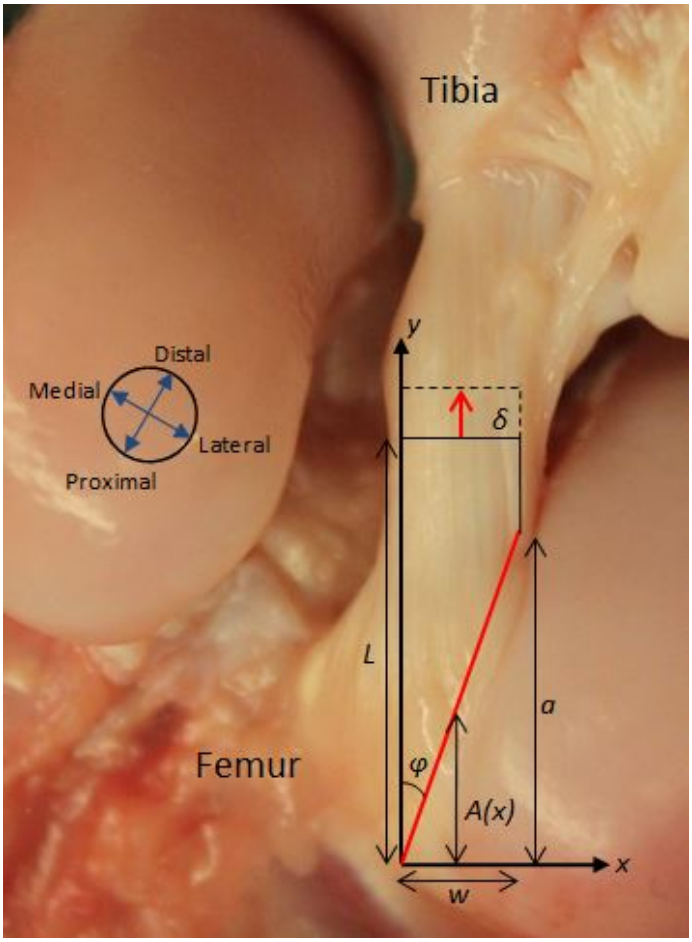

Figure 2.2: Diagram depicting the relationships among variables used in the 2D model over an image of an ovine ACL. The red arrow indicates the direction of the displacement (δ) of the boundary $y = L$, which was 10% of L. The red line represents $A(x)$, the femoral enthesis boundary, described by polynomials.

entheseal profile,

$$A_{linear}(x) = \frac{a}{w}x, \tag{2.5}$$

was considered. Analytic forms for the Lagrange strain tensor and equivalent (von Mises) strain were found using the deformation gradient tensor for each profile's

unique displacement field:

$$\mathbf{F} = \begin{bmatrix} 1 & 0 \\ \frac{\partial u_y}{\partial x} & (\frac{\partial u_y}{\partial y} + 1) \end{bmatrix} \tag{2.6}$$

$$\mathbf{E} = \frac{1}{2}(\mathbf{F}^\intercal \mathbf{F} - \mathbf{1}) \tag{2.7}$$

$$\mathbf{E}' = \mathbf{E} - \frac{1}{3}\,\mathrm{tr}\,(\mathbf{E})\mathbf{1} \tag{2.8}$$

$$E_{eq} = \sqrt{\frac{2}{3}\mathbf{E}' : \mathbf{E}'} \tag{2.9}$$

where $\mathbf{F}$ is the deformation gradient, $\mathbf{E}$ is the Lagrange strain, $\mathbf{E}'$ is the deviatoric part of $\mathbf{E}$, and E_{eq} is the equivalent strain.

Because this study seeks to gain understanding about which entheseal shapes may be more prone to injury, a failure criterion must be considered. Equivalent strain is not an accurate failure criterion for anisotropic materials such as ligaments; however, no such failure criterion currently exists. Furthermore, Luetkemeyer et al. [93] showed that while the two ACL bundles have different longitudinal stress-strain relationships when stretched in the mean fiber direction, their equivalent strains are remarkably consistent. This suggests that the ligaments may deform in ways that minimize their total deviatoric strain energy, and that there may exist some suitable failure criterion similar to the von Mises criterion. Regardless of what that failure criterion is, it seems likely that shear strain is part of it, and thus, that injury is likely the result of both high longitudinal and shear strains. Therefore, equivalent strain is used in this study to approximate the injurious potential that the combined longitudinal and shear loading present in unidirectional loading of a ligament attached to bone at an acute angle have on the ligament.

2.2.2 Finite element model formulation

A 3D finite element (FE) model representing a single ACL bundle was also considered to supplement the findings of the 2D analytical model. The FE model was generated and analyzed in ABAQUS v6.14 (SIMULA, Providence, Rhode Island,

United States), a commercial finite element solver. The ACL models, shown in Fig. 2.3, each have a diameter of 10 mm and net attachment angle of 13°. In agreement with the 2D formulations, convex, linear, and concave ACL enthesis geometries were constructed (shown in Figs. 2.3a-c, respectively).

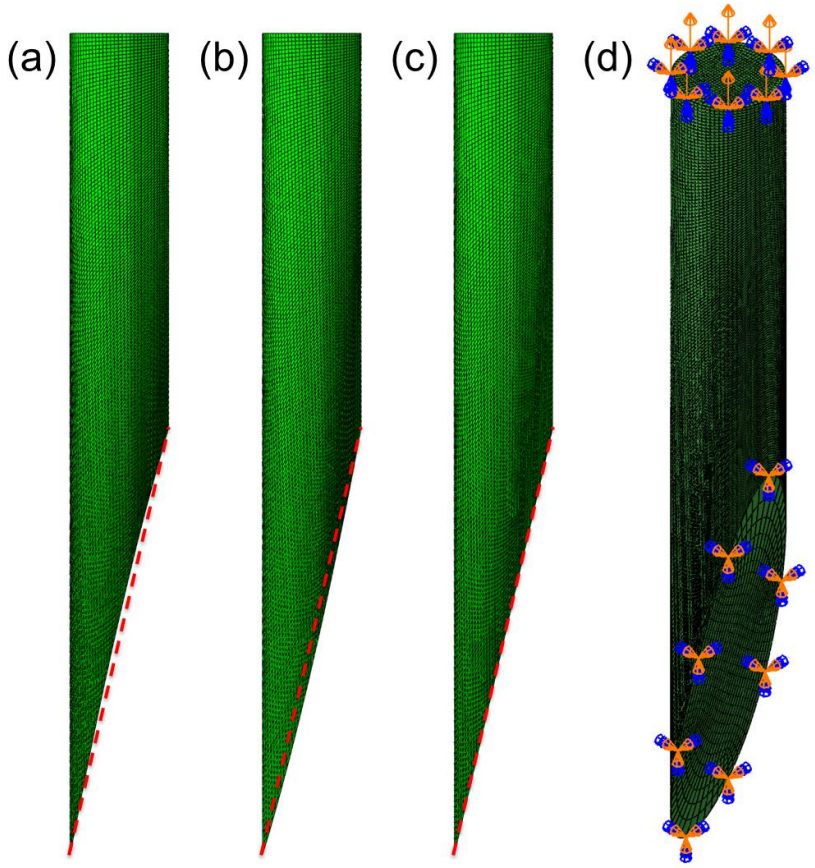

Figure 2.3: 3D FE models corresponding to convex (a), concave (b), and linear (c,d) entheseal shape profiles. Straight, dotted red lines are drawn between the most proximal (left) and distal (right) points of the entheses to highlight the concavity/convexity. The boundary conditions are shown in (d). Elements on the femoral enthesis boundary were encastered and elements on the opposite edge were assigned a uniform axial displacement.

Three constitutive models were implemented for each ACL geometry. First, in

an effort to directly extend the 2D analyses to this idealized geometry, an isotropic (nonlinear) neo-Hookean material description was used. Then, to more accurately describe the material mechanics of ligaments, two transversely isotropic constitutive models were considered: the single fiber family Holzapfel-Gasser-Odgen (HGO) model [71] and a transversely isotropic form of a freely-jointed eight-chain model (FJC) [23]. In models with material directionality, the preferred material direction—or fiber direction—was oriented in a Cartesian sense along the direction of prescribed displacement.

Material parameters were determined based on the optimization framework presented in Marchi et al. [100]. The mechanical behavior of the ACL along its preferred material direction was assumed to be an average of uniaxial responses from each of its constituent bundles [105]. Due to the absence of data describing the mechanical behavior of the ACL normal to its preferred material direction, the transverse behavior of the ACL was assumed to be identical to that of the medial collateral ligament (MCL). Problematically, there is large variability in the observed macroscopic response of the MCL; therefore, the transverse response of the ACL was modeled with data from both Quapp and Weiss [127] and Henninger et al. [66]. Neo-Hookean ACL models were assumed to have the same material parameters as the matrix (isotropic) phase of the HGO model. Experimental data, both along and normal to the preferred material direction, and constitutive model best fits are shown in Fig. 2.4. The large variation in transverse data can be seen by comparing the magnitudes of data in Fig. 2.4b and Fig. 2.4c. All material properties were implemented using user-defined subroutines [100].

Each FE geometry was subjected to an applied macroscopic axial stretch of 1.1. This value was chosen because it is far from small strain but within the physiologic range, in addition to being less than half the failure strain, as measured grip-to-grip [38]. The entheses were completely constrained, while displacements were applied to the surface located on the top of each model in Fig. 2.3. During the displacement step, nodes on the displacement surface were kinematically coupled with respect to a local cylindrical coordinate system attached to a point located in the center of the surface; displacement boundary conditions were applied directly

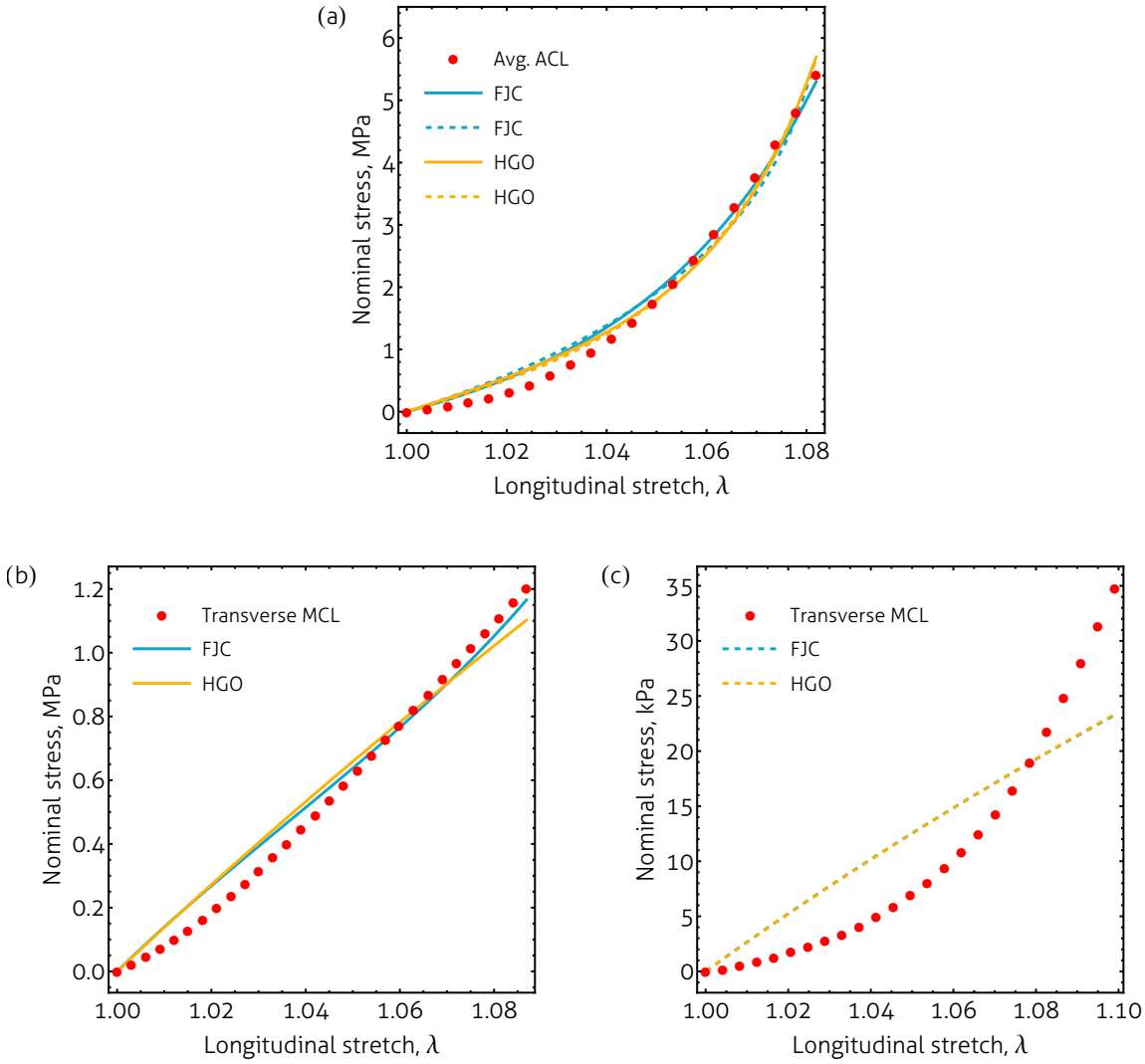

Figure 2.4: Experimental stress-stretch data and constitutive model fits (a) along and (b,c) normal to the preferred material direction. Experimental datasets are from (a) McLean et al. [105], (b) Quapp and Weiss [127] and (c) Henninger et al. [66]. Solid and dashed lines denote constitutive model best fits assuming transverse experimental stress-stretch data from [127] and [66], respectively.

to this central point. This allowed for axial displacements to be prescribed, while simultaneously leaving radial displacements free. Each ACL model shown in Fig. 2.3a-c contained 70,350 fully-integrated hexahedral elements and was solved implic-

Table 2.1: Best fit constitutive parameters of various ACL material models

neo-Hookean	μ (MPa)	B (MPa)		
Quapp and Weiss [127]	4.05	100		
Henninger et al. [64, 66]	0.0736	100		
HGO	μ (MPa)	B (MPa)	k_1 (MPa)	k_2
Quapp and Weiss [127]	4.05	100	3.58	44.2
Henninger et al. [64, 66]	0.0736	100	5.84	33.1
oFJC	C_r (MPa)	B (MPa)	a	$b = c$
Quapp and Weiss [127]	0.0806	100	1.25	1.15
Henninger et al. [64, 66]	0.333	100	2.21	0.325

itly using ABAQUS/Standard. The maximum longitudinal and equivalent strains were evaluated for each geometry.

2.2.3 Macroscopic stress-stretch simulation

The material models implemented in the FE models were built assuming the datasets used were the result of uniaxial tension experiments. However, recent experiments have made full-field deformation measurements of the ACL bundles under tension, and both full-volume [93] and full-surface [97] strain fields show that homogeneous uniaxial tension was not achieved, as both shear and transverse strains were large. The extent to which this assumption affects the construction of the material model is currently unknown. Thus, as a secondary aim, the macroscopic stress-stretch relationship of each FE model was compared to the experimental data to which the constitutive models were fit. Little difference between the FE model predictions and the experimental data would suggest that standard uniaxial tension assumption is a reasonable approximation.

2.3 Results

2.3.1 2D analytic approach

Compared to the linear and concave shapes, the parabolic convex (Fig. 2.1A) enthesis profile increased longitudinal strain throughout most of the ligament, but simultaneously reduced shear strain (Fig. 2.5h-n), thus reducing the equivalent strain (Fig. 2.5o-u). Both the maximum longitudinal strain and maximum shear strain were found on or near the most distal margin of the profiles; however, the magnitude of the maximum shear strain varies greatly with entheseal shape and attachment angle (see Figs. 2.5 and 2.6). Thus, both of these geometrical features were found to have significant effects on the maximum equivalent strain.

The most critical feature of entheseal shape with respect to maximum equivalent strain was the convexity near the most distal attachment point of the ACL. If this part of the profile is convex (as in Figs. 2.1A, 2.1C, and 2.1E), equivalent strain is reduced. In contrast, concavity in this region (as in Figs. 2.1B, 2.1D, and 2.1F) increased the maximum equivalent strain. Maximum equivalent strain moved toward that of the linear entheseal shape with increasing polynomial order (Fig. 2.6).

2.3.2 3D FE approach

Similar differences between ACL attachment geometries were observed with the 3D FE models. Maximum tensile and equivalent strains (calculated using Eq. 2.9) for each ACL enthesis geometry and material model combination are shown in Fig. 2.7. In all cases, for a given material model, the maximum equivalent strains were highest and lowest in ACLs with concave and convex entheses, respectively (Figs. 2.7b and 2.7d). Deformation in neo-Hookean ACL models manifested similarly for equivalent entheseal shapes independent of the experimental data used in their construction. A similar trend was not observed when directional material models were used. While maximum equivalent strains all followed the same pattern (concave > linear > convex), the differences between maximum equivalent strain values notably varied with material model and experimental data. In particular, large differences

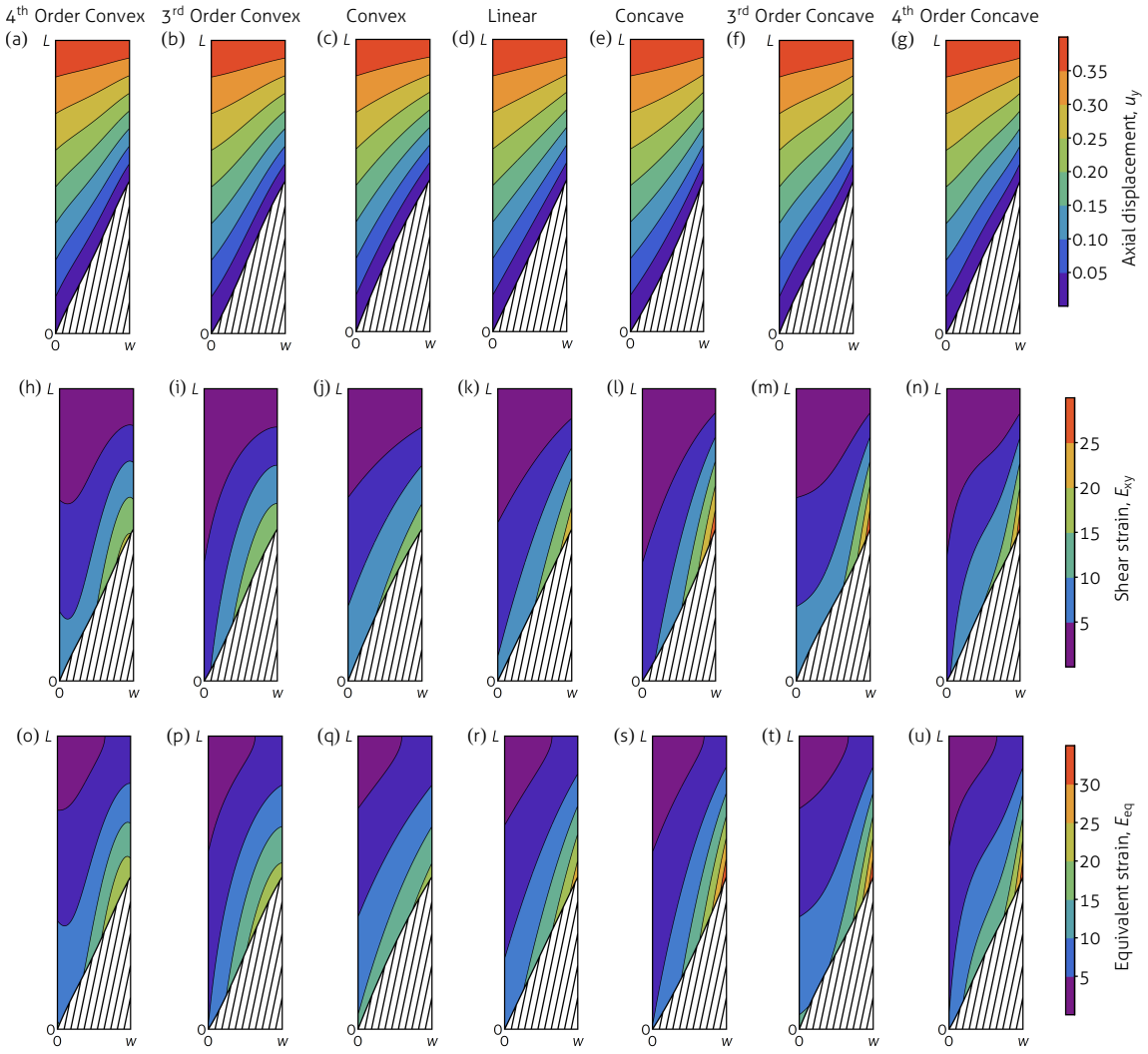

Figure 2.5: 2D (a-g) Longitudinal displacement, (h-n) in-plane shear strain, and (o-u) equivalent strain fields for each entheseal profile. All contours computed with the average male (13°) attachment angle. Hatched regions indicate bone. These results demonstrate that the equivalent strain is largest near the distal (right) end of the enthesis.

in the maximum equivalent strains of convex vs. linear vs. concave entheseal shapes were observed with the FJC model assuming transverse data of the form presented by Henninger et al. [66] (Fig. 2.7d); however, only small differences between maxi-

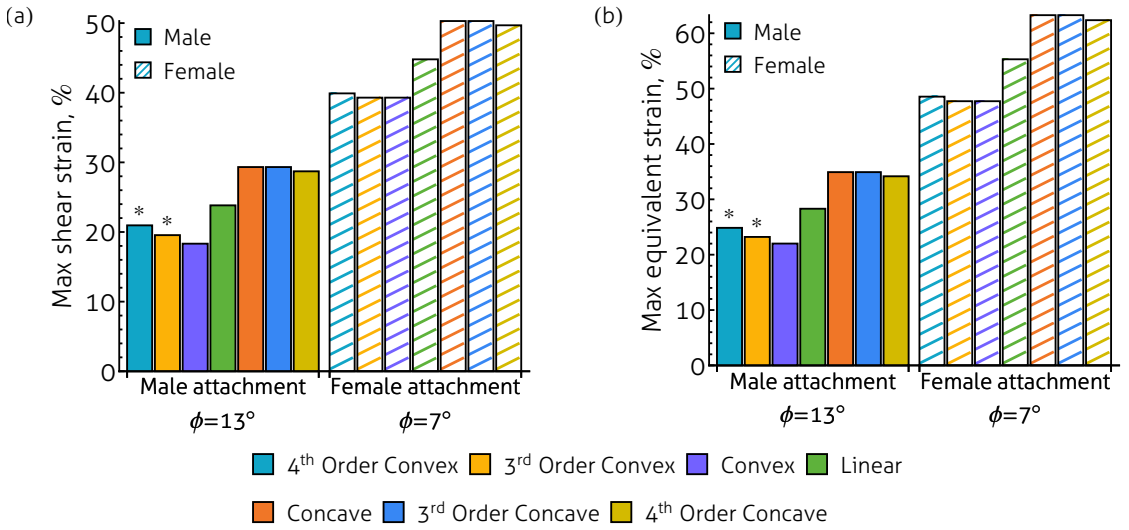

Figure 2.6: 2D maximum (a) shear and (b) equivalent strains of various entheseal profiles and attachment angles. * denotes an entheseal profile for which the maximum strain value occurs at a location other than the point $\{w, a\}$ (see Fig. 2.2).

mum equivalent strains were observed with transverse data from Quapp and Weiss [127] (Fig. 2.7b). There was no consistent trend in the effect of entheseal geometry on maximum tensile strains across material model forms or the experimental data used.

2.3.3 Macroscopic stress-stretch analysis

As a secondary aim, the validity of the assumption of homogeneous uniaxial tension for constitutive modeling purposes was assessed. If uniaxial tension is a valid assumption, the macroscopic stress-stretch relationship of the FE model (an idealized version of the experimental geometry) should match the experimental data used in the construction of the implemented material model. Conversely, the constitutive form, transverse experimental data, and entheseal geometry all affected the macroscopic stress-stretch behavior of the idealized ACL. The stress-stretch responses for each transversely isotropic ACL model along the preferred material direction are shown in Fig. 2.8. There was large variation in predicted macroscopic behavior for

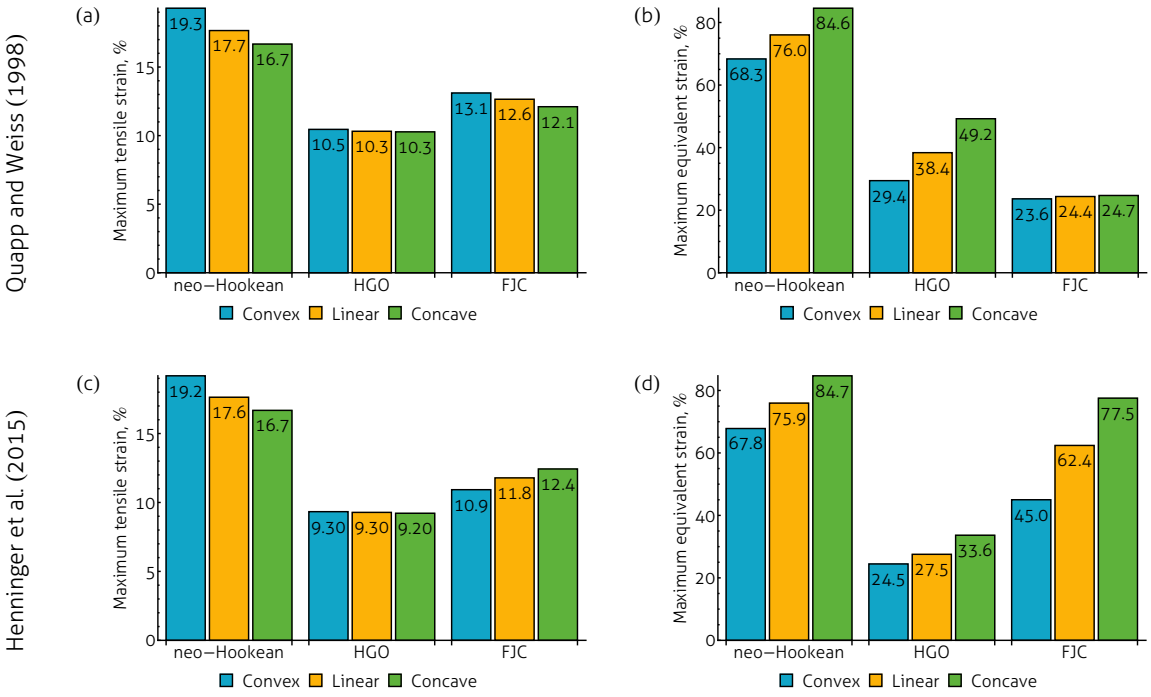

Figure 2.7: Maximum (a,c) tensile and (b,d) equivalent strains in the 3D FE models with various geometric and constitutive models. Mechanical characterization data was obtained from Quapp and Weiss [127] (a,b) and Henninger et al. [66] (c,d).

a given set of transverse experimental data, as well as with the assumed constitutive form. For each transverse dataset (data from either Quapp and Weiss [127] or Henninger et al. [66]), the response of FJC models was stiffer compared to HGO models—comparing (a) to (b) and (c) to (d) in Fig. 2.8. Models built assuming transverse data of the form presented in Quapp and Weiss [127] were stiffer compared to their equivalent Henninger et al. [66] based model; this feature can be seen by comparing (a) to (c) (HGO model) and (b) to (d) (FJC model) in Fig. 2.8. Only FJC based models with transverse data from Quapp and Weiss [127] approached the expected macoscopic preferred material direction response (Fig. 2.8). Small variation between entheseal geometries was also detected. For every material model and transverse data combination except the FJC model with Quapp and Weiss [127] transverse data, convex entheseal attachments produced the stiffest macroscopic stress-stretch

relationship. In the case of the FJC model with Quapp and Weiss [127] transverse data, the concave enthesis yielded the stiffest response (Fig. 2.8).

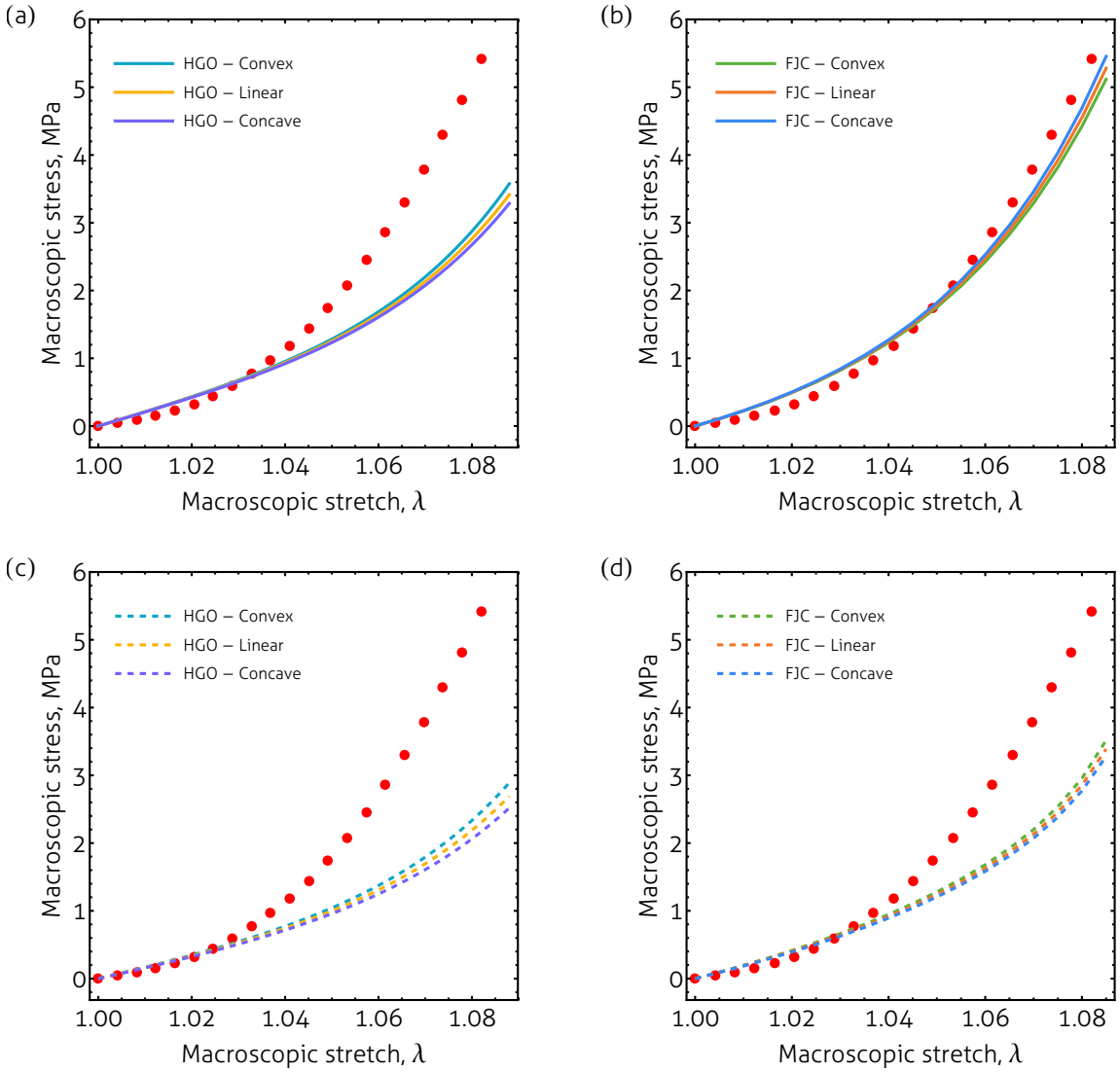

Figure 2.8: Predicted macroscopic stress-stretch curves of various geometric and constitutive models. Simulation results using constitutive model best fits assuming transverse experimental stress-stretch data from Quapp and Weiss [127] and Henninger et al. [66] are shown in (a,b) and (c,d), respectively.

2.4 Discussion

The present results lend insight into why ACL failures often occur at the femoral enthesis. The acute attachment angle of the ACL at the femoral enthesis prompts a concentration in shear strain near the most distal point of attachment. This strain concentration is exacerbated by a concavity in the tidemark in that region, but mitigated by convexity, because concavity locally minimizes while convexity locally maximizes the attachment angle in the distal margin of the femoral enthesis.

While the shear strain in the ACL is sensitive to the convexity of the profile, attachment angle is more influential in the concentration of shear and equivalent strain. The increase in strain with decreasing insertion angle may explain the ACL injury risk associated with small notch width [138, 146, 159], as smaller notch width should require a more acute attachment angle. If so, this provides a mechanistic understanding of the correlation found between notch width and injury risk.

Entheseal shape and insertion angle may help explain the gender disparity seen in ACL injuries. In Beaulieu et al. [21], the mean femoral enthesis attachment angle of female specimens was found to be nearly half that of their male counterparts. A second look at the study's raw data showed that more than 81% of the male tidemark sections were convex near the distal corner of the femoral enthesis, while only about 57% of female enthesis sections exhibited one of these more advantageous shapes [21].

These results may also explain why the PL bundle of the ACL is more susceptible to fatigue failure than the anteromedial (AM) bundle [20, 90]. In the histological study by Beaulieu et al. [21], all parabolic concave profiles were seen in the posterior sections while all but one of the convex profiles were found in anterior sections. Because the PL bundle femoral attachment site is more posterior and distal than the AM bundle attachment, this suggests that the PL bundle may possess a less advantageous concave profile as well as be located in the region of highest shear and equivalent strain concentration.

While other anatomical risk factors are largely non-modifiable, it is possible that the shape of the enthesis may be able to change in response to particular types of

loading. Milella et al. [108] found that entheseal robusticity scores were significantly greater in right versus left upper limb entheses, indicating significant right hand dominance. Although debated, entheseal morphology has long been used as a marker of activity level to study ancient populations in bioarcheology [134]. The fact that almost 70% of all profiles categorized by Beaulieu et al. [21] had a convex shape in the inferior margin suggests that entheseal convexity is favored over concavity with respect to the bone in that region.

Worthy of further investigation is the notable dependence of the maximum equivalent strain values predicted on the constitutive model form and transverse dataset used, as shown in Fig. 2.7. Most computational biomechanics studies on ligaments have ignored the material response orthogonal to the fiber direction. This study used both of the two sets of transverse ligament mechanical data published to date. Even when the same constitutive form and axial response dataset was used, the two model fits provided disparate results. This shows that the transverse and/or shear response of ligaments is a necessary consideration for accurate constitutive modeling of ligament tissue.

When the same datasets were used in the construction of the two transversely isotropic constitutive models considered, they produced dissimilar results as well. This is not necessarily unexpected, as differences in aspects of the model physics, like shear coupling, would lead to differences in the predicted equivalent strain fields. Future ligament computational studies may want to consider more than one constitutive form in their model, since the sparsity of experimental data in multiple deformation states makes it difficult to know which material models can accurately describe the real material physics. Moreover, the lack of data in several deformation states means it is impossible to ensure that all model parameters are identifiable.

Also pertinent to this discussion is the wide array of macroscopic stress values predicted for a given macroscopic stretch illustrated in Fig. 2.8. This applies both to different constitutive models fit to the same datasets as well as to the same constitutive model fit with different transverse data. This has implications not only in modeling, but also in experimental characterization. The fact that these global stress-stretch curves do not align with the curve to which the constitutive models

were fit implies that boundary effects prevent the computational models from achieving a state of uniaxial tension, which was assumed for material model fitting. This indicates that current ligament constitutive models are actually a description of both the structural stiffness and material stiffness. FE models require constitutive models that describe the true material response; thus, material and structural properties need to be decoupled. This is principally a result of the large characteristic decay length (the length over which boundary effects are significant) associated with highly transversely isotropic materials [13, 74]. Still, traditionally, as well as in the current study, ligament constitutive modeling has not yet accounted for the effects that specimen geometry and boundary conditions have on the measured macroscopic mechanical behavior. For this reason, we recently measured full-volume displacement fields for the AM and PL bundles of the ovine ACL [93]. Full-field inverse methods will be used to fit constitutive models to this data, accounting for the irregular geometry and resulting strain field inhomogeneity.

Similarly, it is commonly assumed that the mechanical response of ligaments transverse to the fibers makes little difference in the predicted response of constitutive models of ligaments. As Fig. 2.8 reinforces, both constitutive form and transverse mechanical behavior play invaluable roles in the construction of computational models of the ACL.

Limitations of this study include the use of the von Mises criterion for an anisotropic material, simplified constitutive modeling assumptions, and the possibility that a double bundle model would have been a more accurate representation of the ACL than the single bundle models used. Additionally, the femoral attachment angles used to create the 2D and 3D models were based on data collected at 15°knee flexion. However, it should be noted that this is a common knee flexion angle at which ACL injuries occur [83]. Finally, the cross-sectional shape of the ACL was idealized as a circle and the applied deformation did not include bending, torsion, or displacement in any direction other than axial. More complex loading may yield different results.

Despite the large differences in maximum strains predicted by the various models used, the trend seen in maximum equivalent strain was consistent. A concave

entheseal shape increased the maximum equivalent strain seen by the ACL in every model used, and thus, would appear to be more prone to injury than other enthesis shapes. Future research on ACL injury risk factors should consider entheseal shape and insertion angle.

2.5 Conclusions

The primary aim of this work was to model the femoral attachment of the ACL and determine whether some entheseal shapes, as identified by Beaulieu et al. [21], may cause the ACL to be more prone to injury than others, as predicted by the maximum equivalent strain. Based on all of the models tested, a more acute attachment angle and bone concavity in the distal margin of the enthesis are likely more prone to cause ligament failure than larger attachment angles and convex entheseal shapes. This analysis illustrates the effects of two of the variables involved in predicting the mechanical failure of the ACL.

Additionally, this work used the formulated FE models to examine the validity of traditional constitutive modeling assumptions. It was determined that homogeneous uniaxial tension is not a valid assumption for accurate constitutive modeling, and that the transverse response or matrix phase of the constitutive model has a significant impact on both the strain fields and the macroscopic response.

CHAPTER 3

Full-volume Displacement Mapping of Anterior Cruciate Ligament Bundles with DualMRI

This chapter has been previously published and is used with permission from Elsevier. It may referenced as:

Luetkemeyer, Callan M., Luyao Cai, Corey P. Neu, and Ellen M. Arruda. Full-volume displacement mapping of anterior cruciate ligament bundles with dualMRI. *Extreme Mechanics Letters*, 19: 7-14, 2018.

3.1 Introduction

The number of anterior cruciate ligament (ACL) reconstruction surgeries in the United States continues to rise, particularly for females and young people [84, 96]. ACL ruptures are associated with a three-fold increase in the risk of developing osteoarthritis [17, 78], which decreases quality of life and inflicts notable financial [29] and psychological burdens [12]. Consequently, there is considerable interest in identifying the most significant risk factors for ACL injury as well as ideal reconstruction techniques. Smaller intercondylar notch width [33, 38, 47, 92] and steeper tibial slope [24, 28, 62, 81, 145, 152], for example, have been investigated as potential risk factors by correlating morphological measurements with injury prevalence, but the results of these studies are conflicting. Potential risk factors associated with lower limb mechanics like stiff landings [87], increased peak knee abduction moment [69],

and rearfoot striking [46] have also been detected. Screening methods concerned with movement strategies [42, 50] and neuromuscular movement pattern training programs [147] have been proposed, but have had limited success. With a large and unknown number of variables to consider, these clinical studies have serious limitations. Without the ability to test the effect of a single factor or group of factors and control for all other variables, it is difficult to discern whether a correlative relationship between a particular variable and ACL injury prevalence is also causal. A more fundamental approach, starting with an accurate description of ACL mechanical properties, can add to the current peripheral understanding of ACL injury risk factors.

The ACL consists of the anteromedial (AM) and posterolateral (PL) bundles, which play predominant roles in preventing anterior tibial translation and internal tibial rotation, respectively. Just as their functions differ, their underlying microstructures and mechanics do as well; the AM bundle has less variance in the mean collagen fiber direction than the PL bundle, making it stiffer in tension along the principle fiber direction and presumably less stiff in shear [32, 140]. Both of these deformation states are at play in the tissues physiologically, so the average longitudinal stress-strain relationship in the principal fiber direction is not enough information for adequate mechanical characterization.

Of additional concern is how constitutive models are traditionally fit to mechanical testing data of these tissues. Typically, a homogeneous deformation state (namely, uniaxial tension) is assumed. However, the positive transverse strains and large shear strains experienced by the ACL bundles when they are pulled in the mean fiber direction [97] suggest that a state of homogeneous uniaxial tension is not achieved, even in the midsubstance of these tissues. The assumption of uniaxial tension is considered valid by most in the mechanics community for specimens of isotropic materials with at least a 4:1 length-to-width ratio because the boundary effects (e.g. prohibition of lateral contraction) decay with distance, due to Saint Venant's Principle. But as Horgan and others established long ago, boundary effects decay much more slowly as a function of distance from the boundary in anisotropic materials, particularly along the fiber direction [73, 74, 116]. In 1976, Arridge and Folkes showed that the

measured modulus in the stiffest direction of an anisotropic polymer changed with the aspect ratio of the specimens used, and concluded that the aspect ratio of samples may need to exceed 100:1 to achieve near uniaxial tension in highly anisotropic materials [13]. At that time, the only alternative to increasing the aspect ratio was to determine the stress distribution at the boundary for geometry-independent mechanical characterization of anisotropic materials. Neither of these options is readily feasible for mechanical testing of ligaments. However, there now exists a third option; full-field strain measurements can be used to fit constitutive models using full-field inverse techniques, such as iterative finite element model updating or the virtual fields method [57]. Unlike conventional constitutive modeling, these techniques do not assume homogeneous deformation; in fact, they require a heterogeneous strain field. Additionally, they can account for the influences that geometrical features like the aspect ratio and irregular boundary conditions have on the strain field. These methods do, however, require full-field displacement data.

Full-field deformation measurement techniques like digital image correlation (DIC) and related methods have recently been used to produce surface deformation contours of ligaments and tendons [97, 149]. DIC has provided groundbreaking information about surface deformation, but DIC measurements are limited by their inability to probe the through-thickness deformation. Full-volume deformation fields would provide a more complete picture of bulk constitutive behavior. Additionally, while incompressibility is commonly assumed for constitutive modeling of these tissues, the validity of this assumption has yet to be verified, and this can only be done with full-volume deformation information. Through-thickness displacement fields have been generated for articular cartilage [34, 37] and intervertebral discs [35] using displacements under applied loading by magnetic resonance imaging (dualMRI) methods, but this technique has yet to be used to characterize deformation patterns of ligaments.

A constitutive model capable of predicting the complex mechanical response of the ACL bundles would empower computational models to predict how potential risk factors affect strain, thereby yielding a mechanistic understanding of ACL injury pathology. This in turn would help guide injury prevention efforts and re-

construction techniques in addition to providing a template for the development of tissue-engineered constructs for ACL replacements. However, such a model requires a more comprehensive experimental characterization of ACL bundles than has currently been achieved. Thus, this study provides proof-of-concept that full-volume displacement maps of the ACL bundles can be generated using dualMRI. The average stress-strain responses of the two bundle types are compared and compressibility of the ACL bundles is also explored.

3.2 Methods

3.2.1 Experimental methods

Six ovine (of average market weight 80 lbs.) tibiofemoral joints were purchased from a local abattoir. All connective tissues were removed from the joints, with the exception of the ACL. The AM and PL bundles were carefully separated and an electric oscillating hand saw (Dremel) was used to cut the bones and remove the bundles with small blocks of bone still attached to the ends of each bundle. The bone blocks were fixed in custom grips made of Ultem (MRI compatible plastic) using a non-toxic, moldable thermoplastic (McMaster-Carr, Aurora, OH) such that when the grips were pulled in opposite directions, the fasicles were as equally engaged as possible. The grips were secured to a custom-built loading chamber made of Ultem, which included a bath filled with 1X phosphate buffered saline (Thermo Fisher Scientific, Inc.) to maintain sample hydration. The samples were loaded along the mean fiber axis (designated the y axis), using a pneumatic cylinder actuator (Airpel, Airpot Corp.), and care was taken to ensure that the samples were untwisted to prevent torsion. All specimens were secured in the loading chamber with the tibial end held stationary and the femoral attachment fixed to the actuator. For AM bundles, the anterior side of the tibial attachment was facing up (first slice in z), while the posterior side of the tibial end was up for PL bundles. Fig. 3.1a depicts the coordinate system used and Fig. 3.1b shows the loading chamber.

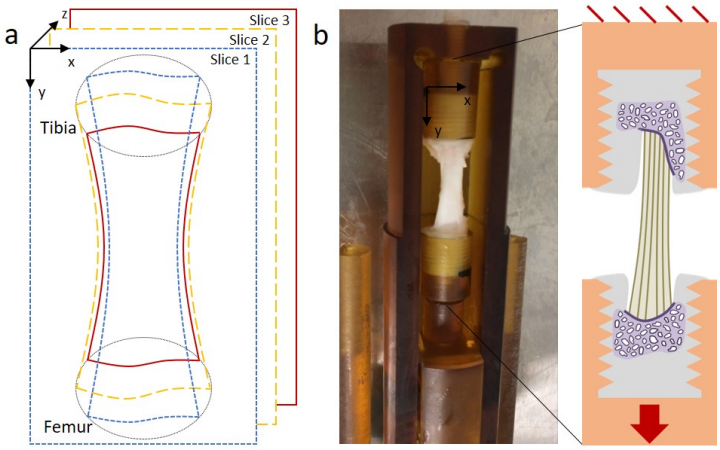

Figure 3.1: The coordinate system used on an idealized AM bundle schematic is shown in (a) and an AM bundle within the loading chamber is pictured in (b) with an illustration of the imposed boundary conditions. Bone blocks (in purple) were held in the threaded Ultem grips (in orange) with heat-moldable polystyrene (in gray). One grip was held fixed against the end of the loading chamber and the other was displaced in the y direction with the actuation rod.

Prior to loading, anatomical images of each specimen were taken using a FLASH (Fast Low Angle SHot) pulse sequence with a field of view of 32x32x5 mm^3 and spatial resolution of 0.125x0.125x1.0 mm^3/voxel. Five slices were imaged through the thickness of each sample (x-y plane), and the position of the five slices were adjusted until the specimen volume was contained in the middle three slices. These three slices were used for imaging with displacement encoding with dualMRI. Additionally, five cross-sectional slices (x-z plane) were imaged along the length of each specimen. ImageJ was used to estimate the number of pixels in the cross-sectional area in each image and the average for each specimen was computed. The average cross-sectional area in pixels was converted to mm^2 and used to calculate nominal stress for each force level.

For dualMRI, specimens were encoded with magnetic field gradients in a reference (low load) state and then un-encoded in a high load state, leaving a phase-difference signal that was directly proportional to the overall change in position, or displacement. This was achieved using a displacement encoding with stimulated echoes

(DENSE) pulse sequence preparation and fast imaging with steady-state precession (FISP) acquisition [34] inside a 7T Biospec MRI scanner (Bruker Medical GmbH, Ettlington, Germany). The ligaments were cyclically loaded (600 cycles, 0.33 Hz) while synchronized with MRI to measure 3D displacements. The DENSE-FISP encoding gradient area was 1.13 π/mm. FISP parameters were: TE/TR = 2.5/5.0 ms, field of view = 32x32x3 mm^3, spatial resolution = 0.5x0.5x1.0 mm^3/voxel, number of averages = 8, flip angle = 15°.

Displacement fields were sought for both bundles at four force levels, to capture the nonlinear stress-strain behavior. A pre-load of 3 N ($\approx$ 0.15 MPa) was used to ensure the displacement encoding began with the samples in a taught configuration but not highly stressed. Pilot data revealed that significant phase wrapping (aliasing) rendered the displacement fields unable to be reliably discerned when the specimens were loaded from the unloaded configuration to higher force levels. In order to keep the measured displacements relatively small and minimize phase wrapping, displacement fields were acquired in steps: 3-12.5, 12.5-25, 25-50 and 50-100 N for the PL bundles, and 3-12.5, 12.5-37.5, 37.5-100 and 100-200 N for the AM bundles. These steps are shown schematically in Fig. 3.2a.

3.2.2 Data processing

Phase was unwrapped using a custom Goldstein branch cut phase unwrapping algorithm [54] and the change in phase was directly calculated by the difference of reference and loaded phases. Phase change for each voxel was then converted to displacement using Matlab (The Mathworks, Natick, MA), as previously described [109].

Masks were drawn to define the region of interest (ROI), or image volume occupied by the sample for each displacement field using morphology defining the ligament from magnitude reconstructions of DENSE-FISP data in the high load (deformed) state of each step, and the displacements outside of the ROI were defined as zero. The raw displacement fields were smoothed using 100 iterations of a 3D Gaussian filter with a kernel size of 3 [36]. A nearest neighbor transform was used to fill

the image outside the ROI with the spatially closest non-zero displacement value to minimize bias at the ROI edges during smoothing.

For computing strains, the desired displacement fields were those describing the total displacements incurred from 3 N to each force level, written in the 3 N reference configuration. The measured displacement fields, on the other hand, were relative displacements in the deformed configurations. For example, the displacement fields measured for the PL bundles described the displacements from 3-12.5 N in the 12.5 N configuration, 12.5-25 N in the 25 N configuration, 25-50 N in the 50 N configuration, and 50-100 N in the 100 N configuration. In contrast, the desired displacement fields for the PL bundles were 3-12.5 N, 3-25 N, 3-50 N, and 3-100 N, all in the 3 N configuration. The basic image processing scheme used to convert the measured displacement fields into the desired ones is described in Fig. 3.2b. Each measured displacement field (originally in its step-specific deformed configuration) was first warped by the negative of itself to yield the same displacement field in the step-specific initial configuration. For force levels past the first, displacement fields were further warped until they were in the original (3 N) reference configuration. Finally, stepped displacement fields in the original reference configuration were superposed to yield the desired total displacement fields. Image warping was performed using the Matlab function `imwarp`.

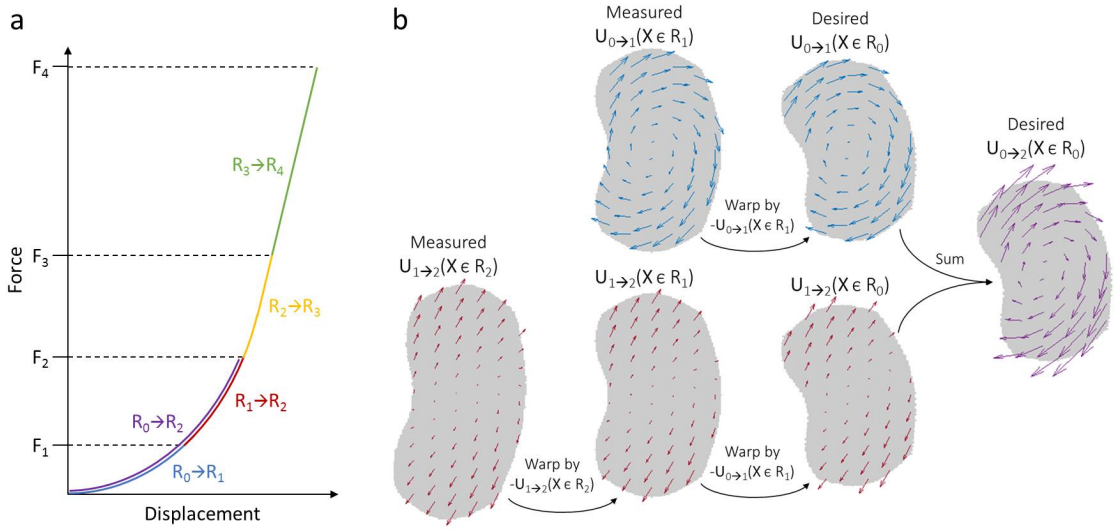

Figure 3.2: An idealized force-displacement curve is depicted in (a) with color-coded regions showing the stepped collection of displacement data. R_0 represents the reference configuration and subsequent configurations are numbered. Part of the image processing scheme used to convert the measured displacement fields (step-wise displacements in high load configuration) to the desired ones (total displacements in original reference configuration) is shown in (b) using an arbitrary 2D shape which has undergone a clockwise rotation and vertical stretching. In the notation used, $\mathbf{U}_{a\rightarrow b}(\mathbf{X} \in R_c)$ refers to the displacement vector field $\mathbf{U}$ required to get from configuration R_a to R_b as a function of 3D position vector $\mathbf{X}$ belonging to the configuration R_c. Blue, red, and purple arrows represent the displacements from the reference configuration to the first step, the first step to the second step, and the reference to the second step, respectively.

Using the full-volume displacement matrices, the deformation gradient tensor was computed for each voxel with

$$\mathbf{F} = \frac{\partial \mathbf{U}}{\partial \mathbf{X}} + \mathbf{1} \tag{3.1}$$

where $\mathbf{F}$ is the deformation gradient tensor, $\mathbf{U}$ is the displacement vector, $\mathbf{X}$ is the undeformed position vector, and $\mathbf{1}$ is the identity matrix. 3-point numerical differentiation was used to approximate the partial derivatives, except at the ROI boundaries where forward or backward difference methods were used. The Lagrange

strain tensor was then found for every voxel at each force level using

$$\mathbf{E} = \frac{1}{2}(\mathbf{F}^{\intercal}\mathbf{F} - \mathbf{1}) \tag{3.2}$$

where $\mathbf{E}$ is the Lagrange strain tensor. Additionally, the volumetric strain, defined as

$$E_{vol} = \det(\mathbf{F}) - 1 \tag{3.3}$$

was computed for each voxel. To contrast the volumetric strain, the equivalent strain was computed from the deviatoric strain tensor with

$$\mathbf{E}' = \mathbf{E} - \frac{\mathrm{tr}(\mathbf{E})}{3}\mathbf{1} \tag{3.4}$$

$$E_{eq} = \sqrt{\frac{2}{3}\mathbf{E}' : \mathbf{E}'} \tag{3.5}$$

where $\mathbf{E}'$ is the deviatoric strain tensor.

Longitudinal strains were averaged over the entire volume to give homogenized strain measures in order to compare the current results to previously published stress-strain measurements. A tangent modulus was estimated for each specimen using the last two data points of each nominal longitudinal stress-strain curve. Mean volumetric and equivalent strains were calculated for each volume and plotted against the longitudinal stress.

3.2.3 Statistics

Clustered linear mixed models were employed to compare the nominal stress-strain relationships of the two bundle types. The volume-averaged longitudinal strain was modeled as a linear function of a logarithmic transform of the nominal stress, and the volumetric and equivalent strains were modeled as linear functions of the nominal stress. The models included a fixed effect term for the interaction between bundle type and stress as well as a random effect term for the specific sample. The statistical models were fit using the Matlab function `fitlme`, which produced a p-value for each

term in each model. The p-value for the interaction term represents the probability that there is no difference in the volume-averaged stress-strain relationships of the two bundle types.

The mean tangent modulus was calculated for the AM and PL bundle groups, as was a standard deviation of the mean for each group. A two-sample t-test was used to compare the tangent moduli of the AM and PL bundles. All of the data collected was used for the linear mixed-effects models. Two AM bundles slipped from the grips at the last force level, and data from these samples were excluded from contributing to the mean tangent moduli and subsequent analysis.

3.3 Results

Example anatomical images for a right AM bundle and corresponding PL bundle are shown Fig. 3.3. The differences in geometry between the AM and PL bundles are readily apparent; the AM bundle is longer and has a larger aspect ratio than the PL bundle. The orientation of the collagen fascicles can be seen in the high resolution images of both bundles, confirming that the specimens were untwisted and well-aligned in the loading chamber. Both bundles have a splayed geometry (widen near the attachments to bone) in the x-y plane and non-flat bone insertions. These geometrical features have non-trivial effects on the displacement and strain fields. Note that the tibial end was held fixed and the femoral end was displaced downwards, in the positive y direction.

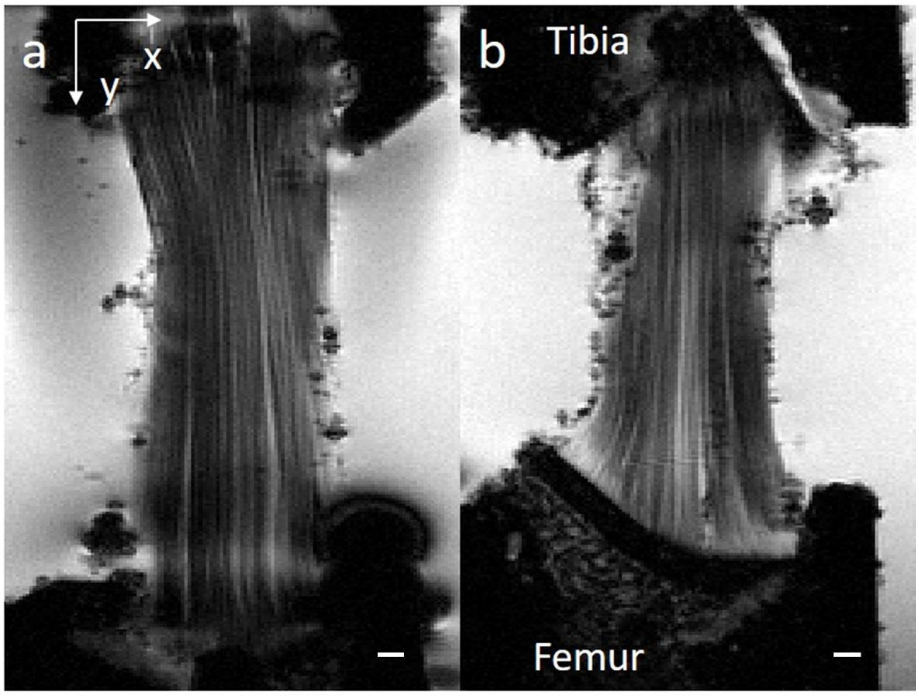

Figure 3.3: Middle slice anatomical images of an (a) AM bundle and (b) PL bundle from a right knee. Scale bars indicate 1 mm. This view is from the bottom of the bath, looking in the negative z direction.

Fig. 3.4 shows the axial (y) displacement contours for each slice of the AM and PL bundles of the same knee. Displacements were nearly zero close to the tibial enthesis and reasonably constant near the femoral enthesis, as would be expected. The y displacements are similar between slices, but differences due to varying slice geometries and their femoral and tibial boundaries are evident. The corresponding strain contours are found in Fig. 3.5. Longitudinal strains (E_{yy}) were large and positive throughout the volume of the specimens tested. Transverse strains were typically large in both directions. Large positive E_{xx} strains were seen in the mid-substance of all samples, and large negative E_{zz} were experienced by most specimens, especially near the femoral enthesis of many AM bundles. Additionally, there were often large and slice-specific shear strains; E_{yz} was particularly large in several AM bundle specimens. Interestingly, volumetric strains were typically negative near the

femoral enthesis for AM bundles, as a result of negative E_{zz} in that region. However, the volumetric strains over the majority of the volume were positive for all the samples tested.

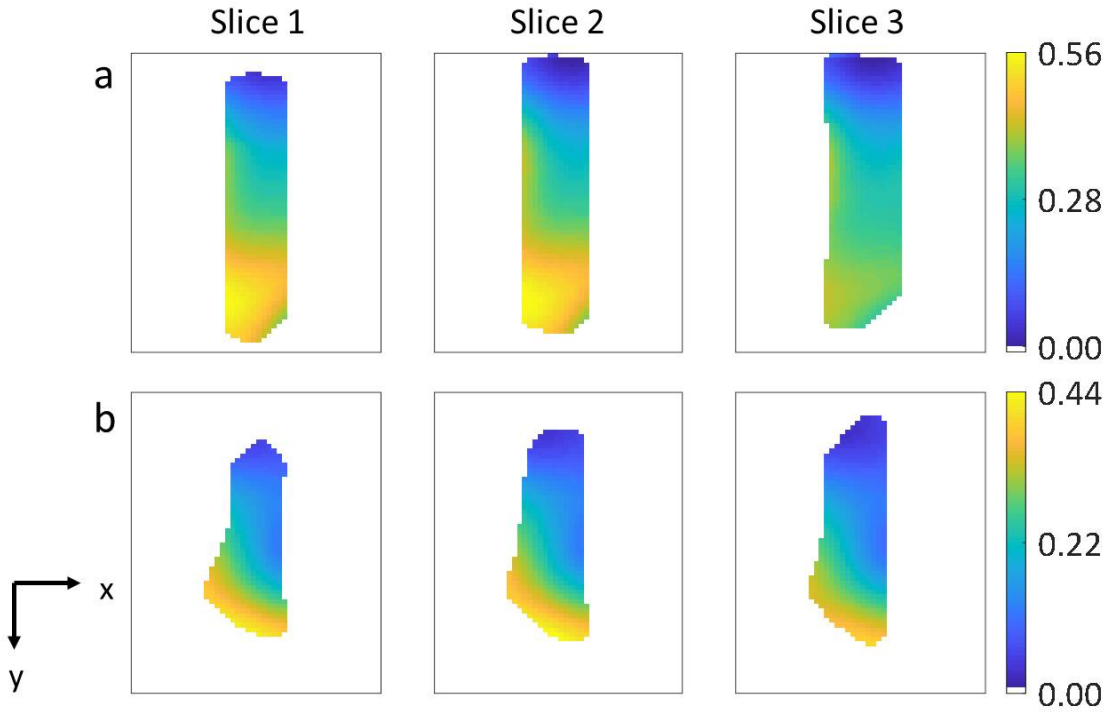

Figure 3.4: Axial (y) displacement contours for the (a) AM and (b) PL bundles of a right knee at the maximum force levels (200 and 100 N, respectively).

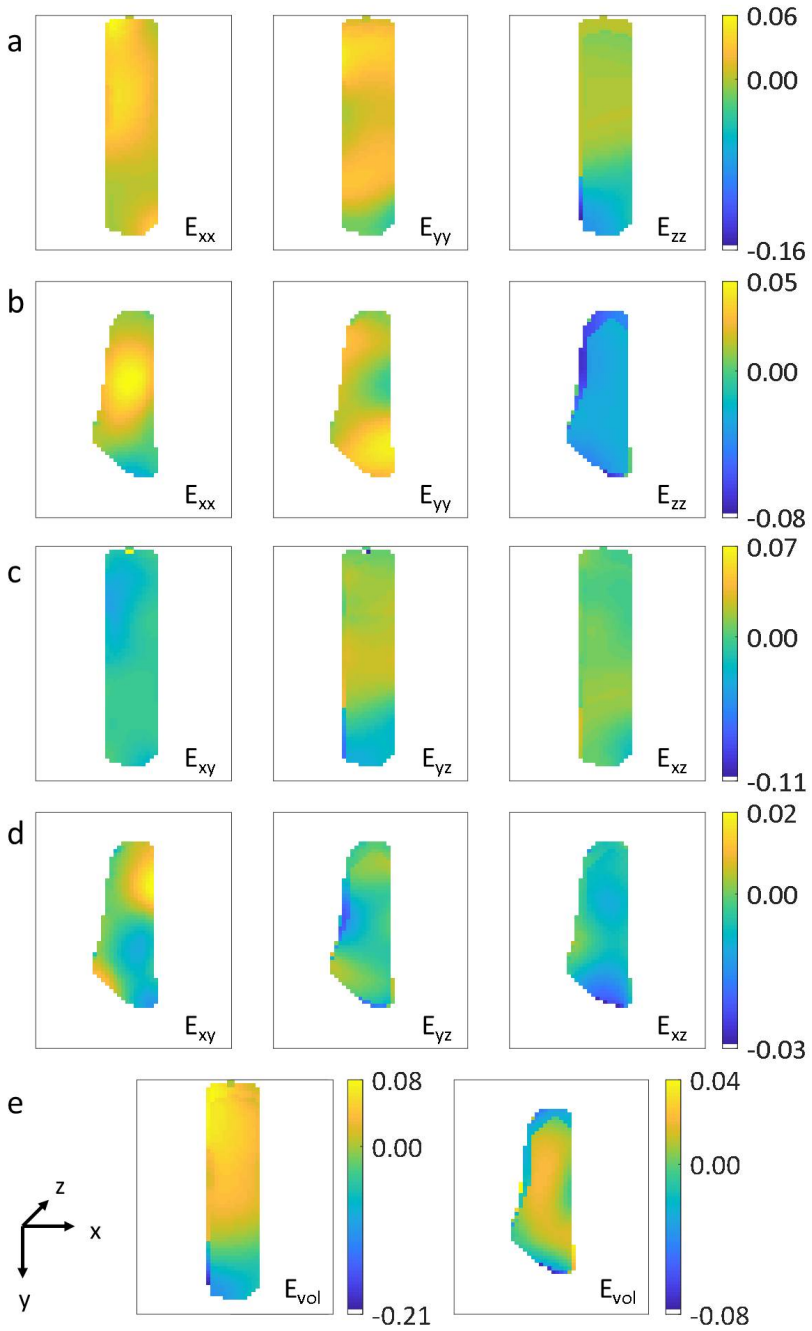

Figure 3.5: Corresponding middle slice (slice 2) Lagrangian strain contours for the example AM bundle (a, c and e left) and PL bundle (b, d and e right) at the maximum force levels.

Homogenized stress-strain curves are shown for each sample in Fig. 3.6a. These curves exhibit the characteristic exponential shape seen elsewhere in the literature, but with a shortened toe-region and much smaller strains than are typically reported [105]. The model constant for the term describing the interaction between the logarithm of the stress and bundle type was statistically significant at the 0.01 significance level ($p = 0.00177$). As depicted in Fig. 3.6b, the mean tangent moduli and their corresponding standard deviations are 737 ± 171 MPa and 445 ± 178 MPa for the AM and PL bundle groups, respectively. The two-sample t-test revealed a statistically significant difference between the mean tangent moduli of the two bundle types at the 0.05 significance level ($p = 0.0271$).

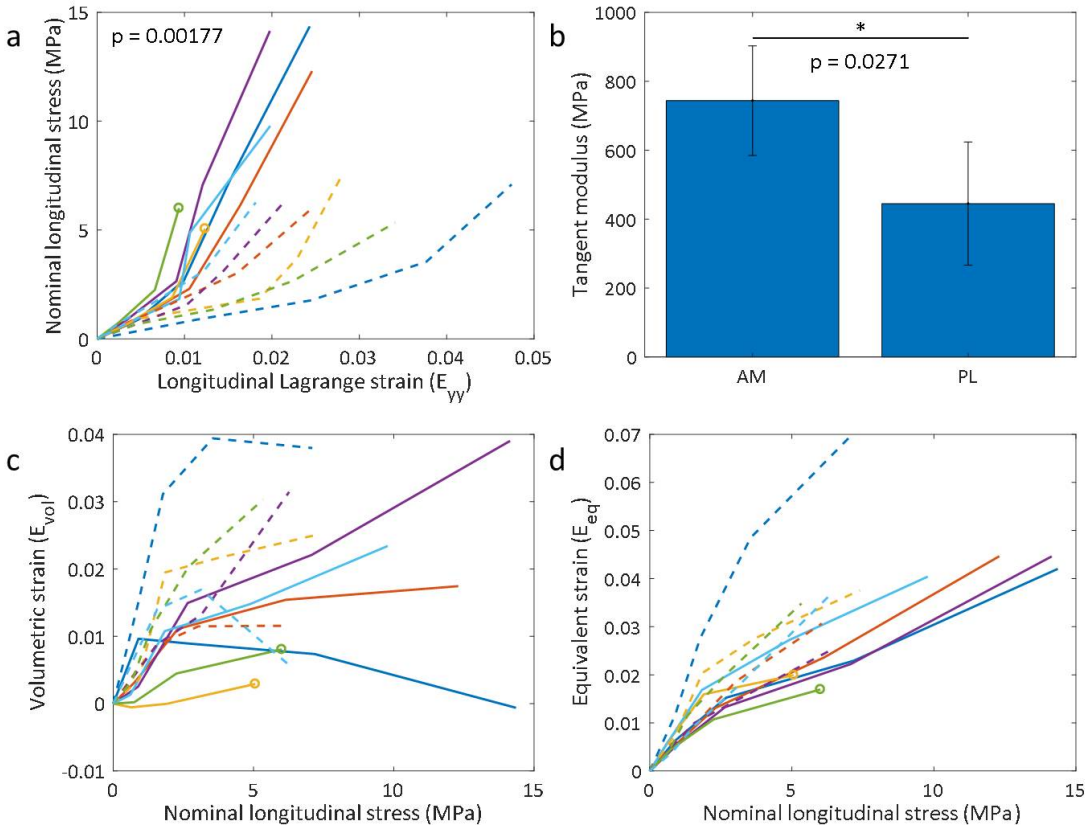

Figure 3.6: Nominal stress vs homogenized longitudinal strain are shown for each specimen in (a). AM bundles are plotted with solid lines and PL bundles are plotted with dashed lines. Note that two AM bundles slipped out of the grips at the final force level and these are indicated with a circle at the final data point. Mean tangent moduli found for each bundle type are depicted in (b). Error bars represent the standard deviation of the mean. The homogenized volumetric and equivalent strains are plotted against the nominal stress for each specimen in (c) and (d), respectively.

Mean volumetric and equivalent strains are plotted in Fig. 3.6c and Fig. 3.6d. The homogenized volumetric strains are entirely positive for most samples and on the order of the mean longitudinal strains. The p-values for the first fixed effects term for the AM and PL bundles were 1.26e-6 and 1.42e-11, respectively, meaning the slopes of the volumetric strain curves are significantly different than zero at the strongest significance level. The homogenized equivalent strains have a nearly linear

relationship with the longitudinal stress and are large compared to the longitudinal strains. The equivalent strain curves were statistically different between the two bundle types ($p = 0.00282$).

3.4 Discussion

The current study is the first to present full-volume deformation contours of ligaments under tensile loading. DualMRI produced realistic and repeatable displacement fields, from which strain fields were computed. These full-volume strains are likely more accurate representations of true bulk mechanical behavior of the ACL bundles than surface-based or grip-to-grip strain measures. It is also worth noting that this method did not require any pattern application as is typical with texture correlation techniques. The recent study by Mallett and Arruda [97], in which DIC was used to measure surface strains, estimated that the mean apparent tangent modulus for the AM bundle was about 1 GPa along the fiber direction. Despite the differences in methods, the mean AM bundle tangent modulus estimate from this work (737 GPa) was smaller but reasonably close to the previously published value obtained from DIC data on similar specimens. The difference between them is largely due to the fact that the current estimate was computed at a nominal stress level of roughly 10 MPa, versus the 20 MPa of the previous study. Both of these estimates are much larger than grip-to-grip measures and other published values for the tangent modulus of the AM bundle.

The statistics performed on the current data suggest that AM and PL bundles have significantly different homogenized structural stress-strain relationships and tangent moduli, which corroborates previous findings [97, 140]. While the AM bundle has more highly aligned collagen than the PL bundle, it is important to recognize that the differences in tangent moduli computed here and elsewhere are likely a result of both differences in material properties and differences in geometry. As stated previously, the AM bundle has a larger aspect ratio than the PL bundle. This geometrical difference would result in a larger measured modulus for the AM bundle along the fiber direction even if no material differences exist. Care should be taken

when comparing the mechanical responses of two anisotropic materials tested with different geometries.

True constitutive properties are independent of geometry and the high degree of anisotropy and irregular geometrical features of the ACL bundles have significant effects on the strain field. For example, the splay that exists to minimize the stress concentration at the ligament-bone junction is the main source of the positive E_{xx} measured in the midsubstance of most of the samples. As the ligaments are pulled in y (the mean fiber direction), they expand in x until the outermost fibers are aligned between the widest points of the splay on both ends. The sample-specific curved boundary conditions also have significant effects on the displacements and strains.

Full-field inverse methods such as the inverse finite element method or the virtual fields method can incorporate irregular geometry as well as tissue heterogeneity into the constitutive model fitting process [56, 136]. Inverse finite element analysis has been employed to determine anisotropic constitutive parameters of cornea [110], skin [59], cervical tissue [162], white matter [49], and meniscus [137], among other soft tissues. The virtual fields method has been used to fit anisotropic hyperelastic models to human arterial tissue [16].

The volumetric strains presented in Fig. 3.6c exhibit large sample variability, but are overwhelmingly positive and large. The statistical analysis shows that the slopes of the volumetric strain curves are significantly different than zero for both bundle types. Given this evidence, there can be little doubt that the ACL bundles can, and do, undergo non-negligible changes in volume under mechanical stress. Equivalent strains were remarkably consistent among samples, which may mean that it is possible to establish a yield criterion for predicting ligament injury.

This study presented several challenges and limitations that should be addressed in future work. There was significant bending in the load train that caused large z displacements for some samples. As a result, it is possible that some data were lost from the field of view. Additionally, while stepped force levels allowed confident measurement of displacements at large loads, the superposition of stepped displacement fields to yield total displacement fields propagated errors. Last, a pre-load of 3 N may have been too large. This is may have contributed to the shortened toe-region

in the homogenized stress-strain curves.

The analysis presented here is a first step to utilizing the data that dualMRI has to offer. The datasets collected in this study show that homogeneous uniaxial tension is not achieved in any sizable volume in the ACL bundles, and that they are compressible materials. Therefore, these traditional assumptions may not be valid for purposes of geometry-independent constitutive characterization. Future work will use full-field inverse methods to fit constitutive models to the full-volume displacement data.

CHAPTER 4

Fiber Splay Precludes the Direct Identification of Ligament Material Properties: Implications for ACL Graft Selection

This chapter will be submitted for publication as a journal article and may then referenced as:

> Luetkemeyer, Callan M., Ryan A. Rosario, Jonathan B. Estrada, and Ellen M. Arruda. Fiber splay precludes the direct identification of ligament material properties: implications for ACL graft selection.

4.1 Introduction

Ligament and tendon injuries are the most common musculoskeletal problems for which medical attention is sought [142]. These injuries are generally painful and debilitating, and they present a significant financial burden. An appreciable amount of literature is dedicated to the identification of injury risk factors (features which increase an individual's susceptibility to injury) for various tendons and ligaments, and these studies typically fall into one of two categories: correlative [24, 87, 88, 153] and mechanistic [41, 94, 144]. While the detection of correlations between the presence of particular features and injury prevalence may indicate a role in injury risk, there is often no mechanistic underpinning to substantiate the claim that these cor-

relative factors are also causal. Conversely, because ligaments and tendons perform a mechanical function, mechanistic studies use computational tools such as finite element analysis to systematically evaluate the effect of possible risk factors on ligament strain concentrations, and thus, their injurious potential. However, computational models require accurate material descriptions, and the literature on this topic is conflicting and inconclusive.

Ligaments and tendons are nonlinear and anisotropic materials, which makes the material modeling process challenging. They derive their anisotropy from highly-aligned, stiff, type-I collagen fibers, which are embedded in a compliant matrix composed of elastin and other extracellular matrix proteins [150]. Nonlinearity requires multiple material parameters to be identified, and anisotropy demands mechanical deformations be provided in multiple directions. For studies interested in general material stiffness comparisons between groups rather than material modeling, a tangent modulus (slope of the uniaxial stress-strain curve) in the fiber direction of these materials is a useful measure. However, even for this most basic material property, reported values in the literature can span several orders of magnitude for a given ligament or tendon [39, 97, 112, 140].

The material properties of ligaments and tendons are also important criteria for graft selection and tissue-engineered graft design for tendons/ligaments that require surgical reconstruction if torn. For example, a frequently used graft option for reconstruction of the anterior cruciate ligament (ACL) – the most commonly injured knee ligament – is the middle third of the patient's own patellar tendon (PT) [151]. However, it is debated whether PT material properties are sufficiently similar to those of a native ACL. Prevailing opinion considers the PT to be a stiffer material than the ACL, as several studies comparing the two have reported a larger tangent modulus for the PT graft [30, 39, 40, 45]. Still, others have reported conflicting evidence [31, 130].

However, there is much we do not fully understand about the mechanical behavior of ligaments and tendons. For example, recent studies using full-field displacement mapping techniques like digital image correlation (DIC) and displacement-encoded magnetic resonance imaging (MR-u) have revealed that the ACL bundles actually

expand laterally when pulled in the mean fiber direction [93, 97]. A study with similar findings for the Achilles tendon and deep flexor tendon led authors to report negative Poisson's ratios [53]. However, it is likely that this unexpected behavior is due to a combination of a high degree of anisotropy and the spatial inhomogeneity in the collagen fiber direction that characterizes "fiber splay." Collagen fibers tend to spread out, or splay, near the attachment to bone or muscle, and this splay likely causes the unexpected expansion. As these structures are loaded in the axial direction, the longer fibers on the outside of the splay tend to straighten, and this deformation is minimally opposed by a very compliant matrix. We hypothesized that this fiber splay may have consequences on the grip-to-grip (macroscopic) stress-strain response of ligaments, resulting in a measured, or apparent, tangent modulus that is not indicative of true material stiffness.

This study investigated the influence of fiber splay on the apparent tangent modulus of ligaments – specifically the ovine PT and anteromedial (AM) and posterolateral (PL) regions of the ACL. We defined a geometric quantity called the splay ratio, in accordance with the results of an analytical analysis that described the relationship between splay geometry and apparent material stiffness. The effect of fiber splay was more rigorously investigated with a finite element model and experimental analysis. The results of all three approaches demonstrate that apparent material stiffness is significantly affected by fiber splay geometry. Experiments further indicate that the PT is likely not a stiffer material than the ACL, but rather appears stiffer due to differences in fiber splay.

4.2 Methods

This study used experimental, theoretical, and computational methods to investigate the effect of fiber splay on the global stress-stretch response of ovine knee ligaments. Typical dimensions (in mm) of the ovine specimens used in the experimental part of the study are shown in Table 4.1. These dimensions were used in the analytical model and finite element model to investigate how the PT and ACL regions might appear more or less stiff (based on grip-to-grip mechanical measurements) due

to differences in fiber splay, even if they were made of the same material.

	AM region	PL region	Whole PT	PT graft
L_0	25	18	50	50
w_{max}	7.0	6.0	13.0	4.3
w_{min}	4.5	4.0	10.5	3.5
Splay ratio	15.6	13.5	24.8	74.3

Table 4.1: Representative dimensions (in mm) for the ovine AM region of the ACL, PL region of the ACL, whole PT, and PT graft (middle third of the PT) demonstrate the typical differences in geometry and fiber splay. L_0 refers to the length in the unloaded configuration, while w_{max} and w_{min} are measurements of the enthesis and mid-substance widths, respectively. See Eq. 4.1 for the definition of splay ratio, which quantifies the dependence of apparent material stiffness on specimen geometry.

4.2.1 Analytical model development

A simplified, 2D analytical model of a ligament with linear elastic fibers (and no shear/transverse stiffness) was developed to examine the effect of fiber splay geometry on macroscopic mechanical behavior. Three splay-related dimensions were considered – enthesis width (w_{max}), mid-substance width (w_{min}), and unloaded ligament length (L_0) – and they are illustrated in Fig. 4.1 and quantified for ovine ligaments in Table 4.1. Using the analytical model, a relationship between ligament geometry and the apparent tangent modulus ($\bar{E}$) was derived,

$$\bar{E} \propto \frac{L_0}{w_{max} - w_{min}} \frac{w_{max}}{w_{min}} \tag{4.1}$$

and this quantity was named the splay ratio. A detailed derivation can be found in Appendix A.

4.2.2 Finite element modeling

Finite element models with various splay ratios were created to determine the effect of splay on apparent tangent modulus, as shown in Fig. 4.2. Unlike the analytical

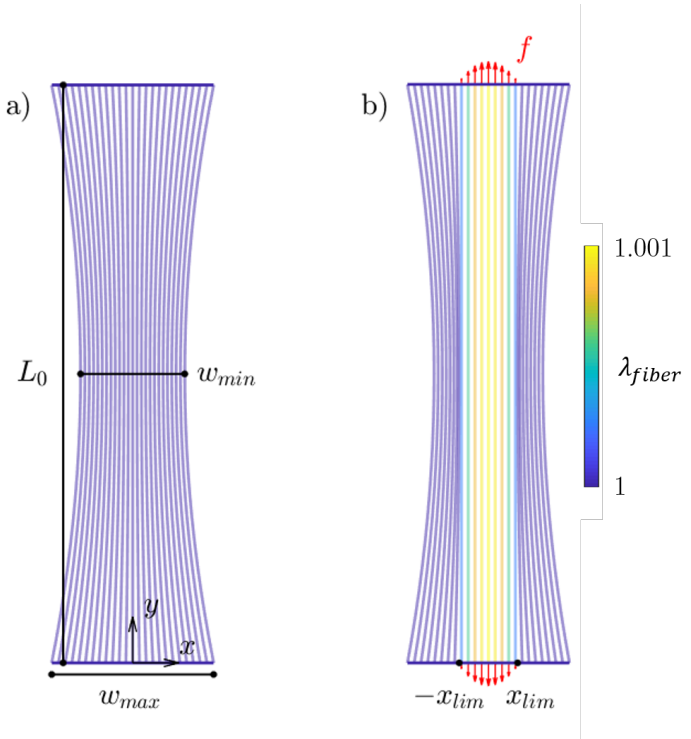

Figure 4.1: The analytical model was built as a function of three geometric variables, shown here (a) for typical dimensions of an ovine AM region of the ACL. The global (total) force is the integral of the boundary force distribution f, which is nonzero over the width of engaged fibers, $[-x_{lim},x_{lim}]$.

model, these models accounted for the continuum, nonlinear behavior of ligaments, as well as the curved shape of the entheses (attachment to bone). The widths at the entheses and at the mid-substance were fixed at 2.0 m and 1.6 m, respectively, and the splay ratio was varied by varying the length (L_0). The thickness was fixed at 0.1 m. Model lengths varied from 2-19 m in unit increments. Symmetry planes were included on two of the surfaces to reduce computation time. The geometry was meshed with linear hexahedral elements with four elements through the thickness, 40 elements through the width, and the number of elements through the length varied to keep a roughly constant element size, ranging from 35 to 375. To ensure that model outputs were independent of mesh density, the mesh density was doubled.

Doubling the mesh density changed the stress at max stretch by $< 2\%$, so the mesh was considered sufficiently fine. Material directions were assigned to each element based on the tangent vector of the parabola connecting the centroids of elements running lengthwise along the geometry. To determine the nominal stress-strain behavior of these varying geometries, samples were pulled to 6% nominal strain over 5 s, and reaction forces from the top surface were extracted. All simulations were run using an explicit solver in ABAQUS v6.14 (SIMULIA, Providence, Rhode Island, United States).

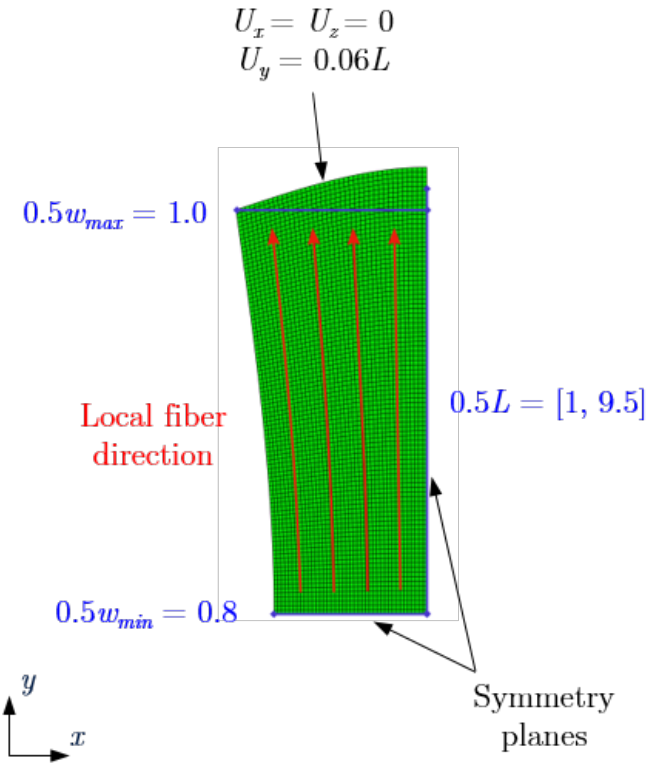

Figure 4.2: The finite element model had a fixed thickness and fixed widths at the ends and mid-substance. The length of the model was varied to create various splay ratios. Symmetry planes were included on two of the surfaces to reduce computation time.

To incorporate the degree of anisotropy commonly seen in ligaments, the Holzapfel-

Gasser-Ogden model with fully aligned fibers (HGO) was used [70]:

$$\begin{aligned}\boldsymbol{\sigma} = C_{10}J^{-\frac{5}{3}}(\mathbf{B} - \frac{1}{3}I_1\mathbf{1}) + B(J-1)\mathbf{1} \\ +2k_1J^{-1}(I_4-1)\exp\left[k_2(I_4-1)^2\right]\mathbf{a}\otimes\mathbf{a}\end{aligned} \tag{4.2}$$

where $\boldsymbol{\sigma}$ is the Cauchy stress, C_{10} is the shear modulus of the isotropic matrix phase, $I_1 = tr[\mathbf{B}]$ is the first invariant of the left Cauchy-Green tensor, k_1 and k_2 are material parameters describing nonlinear fibers, $I_4 = \mathbf{a_0^T C a_0}$ is the stretch along the fiber direction ($\mathbf{a}_0$ is the fiber direction in the reference configuration and $\mathbf{C}$ is the right Cauchy-Green tensor), $\mathbf{a}$ is the fiber direction in the deformed configuration, B is the bulk modulus, J is the Jacobian of the deformation gradient tensor, and $\mathbf{1}$ is the identity tensor. For our simulations, $C_{10} = 34$ kPa; $k_1 = 42$ MPa, $k_2 = 27$, and $B = 10$ MPa. The isotropic parameters (C_{10} and B) were previously determined by Marchi and colleagues [101] using transverse tension data from Henninger et al. [65] for the medial collateral ligament. The anisotropic, or fiber-specific, parameters (k_1 and k_2) were determined by fitting the model to the stress-stretch data collected from the highest splay ratio patellar tendon sample in this study, as it would be expected to have the least strain inhomogeneity. The constitutive model was implemented as a custom VUMAT.

4.2.3 Experimental methods

Ovine tibiofemoral joints were acquired from a local abattoir. For each joint, the whole PT was removed, using a reciprocating hand saw (Dremel, Racine, WI) to cut small bone blocks out of the patella and tibia which contained the ligament's attachments. All other connective tissues were then removed, leaving only the ACL between the femur and tibia. The natural separation of the AM and PL regions on the tibial attachment was followed up to the femoral attachment with forceps to break any weak connective tissue between them. Both ACL regions were then removed with small bone blocks attached. Specimens were refrigerated and stored in 1X phosphate buffered saline (Thermo Fisher Scientific, Inc., Waltham, MA) until

used within 24 hours.

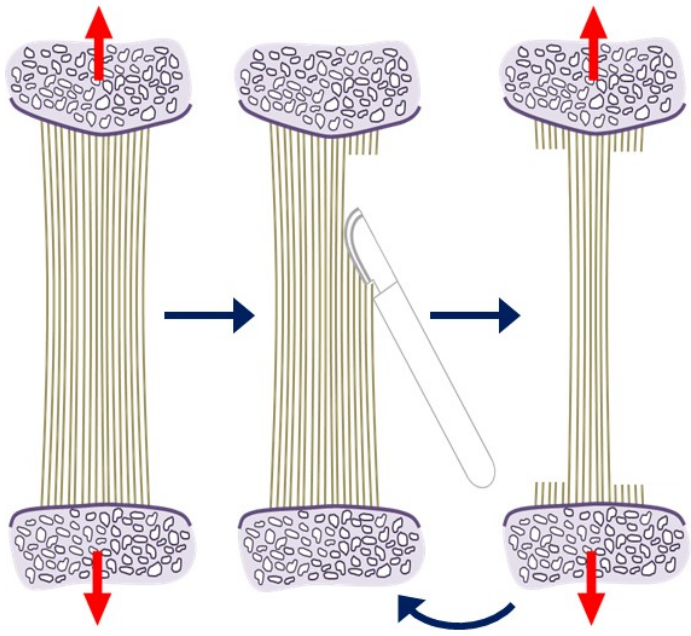

Figure 4.3: Bone-ligament-bone specimens were mechanically tested at 0.1 mm/s in uniaxial tension and returned to their reference position. Fascicles were removed from both edges of the specimen (overemphasized here), after which, the uniaxial test was repeated. This process was repeated to yield data for three to four splay ratio geometries per specimen.

Prior to testing, each specimen was trimmed in its thinnest dimension, using a #11 scalpel to yield samples of ∼1 mm thickness. This was done to minimize heterogeneity in the out-of-plane deformations (i.e. to approximate plane stress) and make comparisons to the 2D analytical model as relevant as possible. The average length, enthesis widths, and thickness of each specimen were measured using multiple dial caliper measurements. The bone blocks on both ends of each specimen were surrounded in moldable heat-set thermoplastic (Polly Plastics, Midland, MI) within a custom-made mold to yield a regular, rectangular prism shape that would be easily integrated into the testing rig clamps. Care was taken to ensure that the plastic would not restrict the movement or deformation of the ligament. Additionally,

it was imperative that the bone plugs were positioned such that fibers were as equally engaged as possible when the ligament was pulled uniaxially.

The bone plugs (encased in plastic) were fixed in a horizontal uniaxial mechanical testing machine (ADMET Inc., Norwood, MA) with pneumatic clamps. Specimens were first pre-tensioned to 0.1 N, and then stretched at 0.1 mm/s to a grip-to-grip longitudinal strain of ∼7%. One to two fascicles were then cut away from the lateral and medial edges of the specimen to increase the specimen's splay ratio, as shown in Fig. 4.3. The specimen was again loaded at 0.1 mm/s to ∼7% grip-to-grip strain. This process was repeated one to two more times, depending on the initial size of the specimen.

The mid-substance (minimum) width was measured for each test of each specimen using ImageJ analysis of a digital image taken just prior to testing. The enthesis (maximum) width for cut specimens could not be measured directly, as the entheses were covered by the thermoplastic. Thus, it was estimated using the uncut mid-substance and enthesis width (referred to as w^0_{min} and w^0_{max}, respectively) and the cut mid-substance width (w_{min}), using the relation $w_{max} = \frac{w^0_{max}}{w^0_{min}} w_{min}$. The macroscopic, or average, longitudinal stress was then computed for each test of each specimen using the measured mid-substance (minimum) width and assuming a rectangular cross-section. The apparent tangent modulus was evaluated for each test as the slope of the best-fit line for the data points between 4.5% and 5.5% grip-to-grip strain on the macroscopic stress-strain curve. Linear and nonlinear regression analyses were used to examine whether the splay ratio significantly affects apparent tangent modulus; the nonlinear model used a logarithmic function, based on the shape of the tangent modulus vs. splay ratio curve found with the finite element model.

4.3 Results

The analytical relationship between fraction of engaged fibers and macroscopic ligament stretch is shown in Fig. 4.4a for typical dimensions of the ovine PT and ACL regions (see Table 4.1). All fibers in the PT graft are engaged before $\lambda =$ 1.00025, whereas less than half of both ACL regions' fibers are engaged at $\lambda =$

1.001, due only to their differences in geometric splay ratio (splay ratios were 16 and 14 for the AM and PL regions, respectively, and 74 for the PT graft). More importantly, the model predicts that these differences in geometry lead to differences in the macroscopic stress-stretch relationships, as shown in Fig. 4.4b. The differences in fiber recruitment led to a seemingly stiffer, linear PT graft and more compliant, nonlinear ACL regions, even though all the ligaments were assumed to be built of fibers with identical material properties.

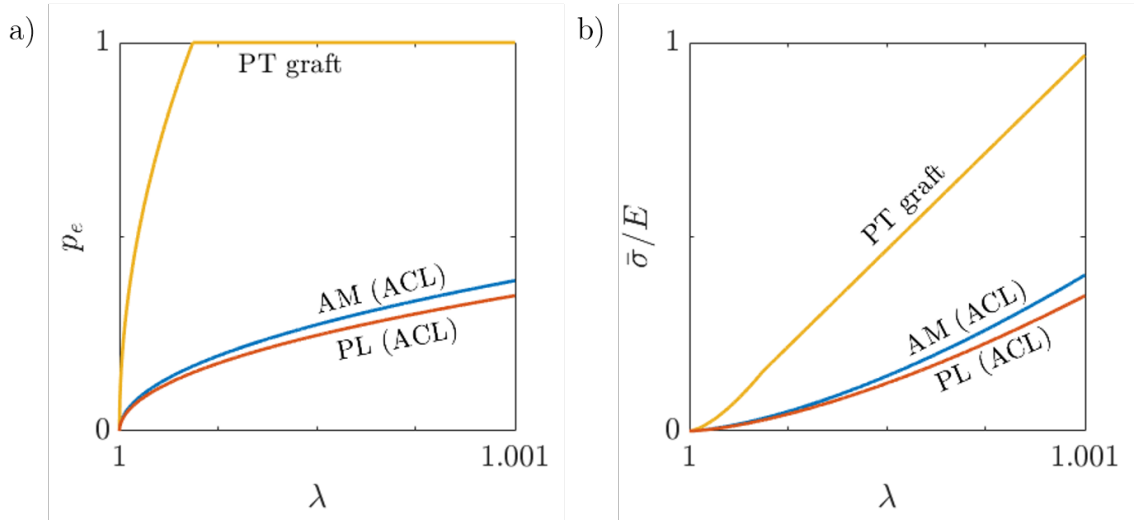

Figure 4.4: The analytical model-derived (a) fraction of engaged fibers (p_e) and (b) normalized, non-dimensional average stress ($\bar{\sigma}/E$), as defined by Eqs. A.12 and A.14, respectively, are plotted against macroscopic (grip-to-grip) ligament stretch (λ) for typical dimensions of an ovine PT graft and AM and PL regions of the ACL. Due to their smaller splay ratios, the ACL appears more compliant and nonlinear compared to the larger splay ratio PT graft.

Experimental results show that the apparent tangent modulus increased with increasing splay ratio ($\frac{L_0}{w_{max}-w_{min}}\frac{w_{max}}{w_{min}}$) for the ovine PT and both ACL regions. The effect of splay geometry on the macroscopic stress-strain relationship is demonstrated for a single PT sample in Fig. 4.5a. As collagen fascicles were removed from the medial and lateral edges of the ligament, the average stress in the ligament was larger for the same grip-to-grip displacement, as a result of the larger splay ratio. The PT

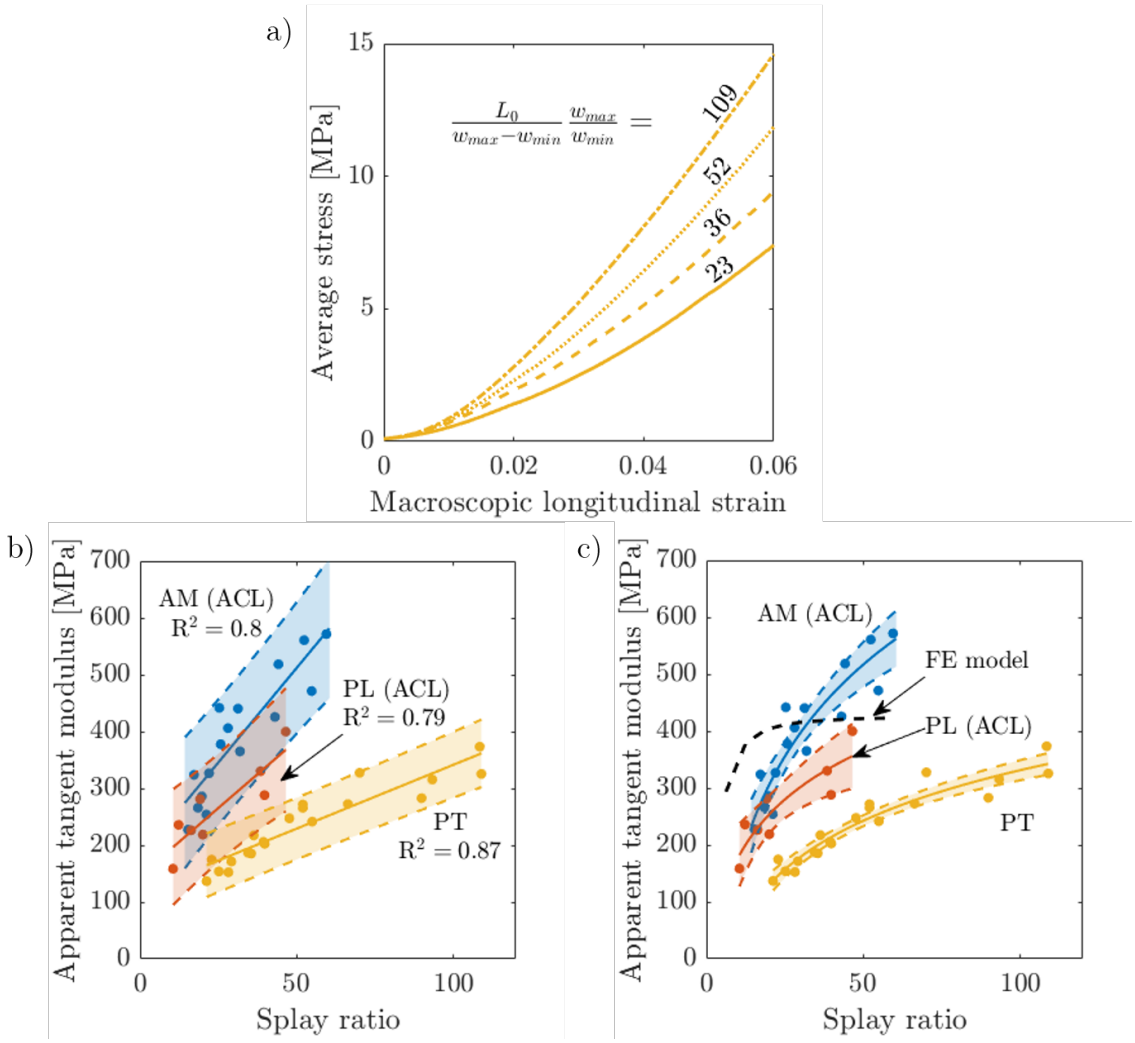

Figure 4.5: (a) Macroscopic stress-strain curves for a single PT sample at multiple splay ratios (noted above each curve) illustrate the effect of splay geometry on its macroscopic mechanical behavior. (b-c) The apparent tangent modulus at 5% grip-to-grip strain increased with increasing splay ratio for the PT and both ACL regions. The apparent tangent modulus of the PT is similar to or less than that of both ACL regions at similar splay ratios. Linear (b) and nonlinear (c) regression lines are represented by solid lines and 95% confidence intervals are bounded by dashed lines. The results of the finite element (FE) model are shown in (c) with a black dotted line.

appeared to be more compliant than both ACL regions for similar splay ratios; experimentally measured values for apparent tangent modulus at 5% grip-to-grip strain are plotted against splay ratio for the PT and both ACL regions in Fig. 4.5b. However, similar to previous findings [30, 39, 40, 45], the PT graft had an apparent tangent modulus similar to the AM and PL at their respective physiological splay ratios (74 vs. 16 and 14). Linear regression analysis indicated that the relationship between apparent tangent modulus and splay ratio was highly significant, with p-values well below 0.001 for the PT and AM and PL regions, as shown in Table 4.2. Nonlinear regression yielded similar results.

	AM bundle	PL bundle	PT
Linear regression	3.13e-06	3.03e-3	2.46e-09
Nonlinear regression	8e-07	3.51e-3	4.78e-11

Table 4.2: Linear and nonlinear regression p-values indicate that the relationship between experimentally measured apparent tangent modulus and splay ratio is highly significant for each of the ligaments tested.

Finite element results incorporating fiber splay qualitatively match experimentally observed macroscopic stress-strain behavior. In addition to tensile strain in the axial (pull) direction, there were also large tensile strains in the in-plane transverse direction due to straightening of the outermost splayed fibers (see Fig. 4.6). At splay ratios similar to those for the ACL regions (14-16), the magnitude of the transverse tensile strain was similar to those seen experimentally [93, 97]. The magnitude of the transverse tensile strain was greatest in the mid-substance of the material, and it decreased as splay ratio increased. The apparent tangent modulus at 5% nominal strain increased with increasing splay ratio, approaching ∼425 MPa at large splay ratios.

4.4 Discussion

Material properties, by definition, are independent of specimen geometry. This study used analytical, computational, and experimental methods to demonstrate

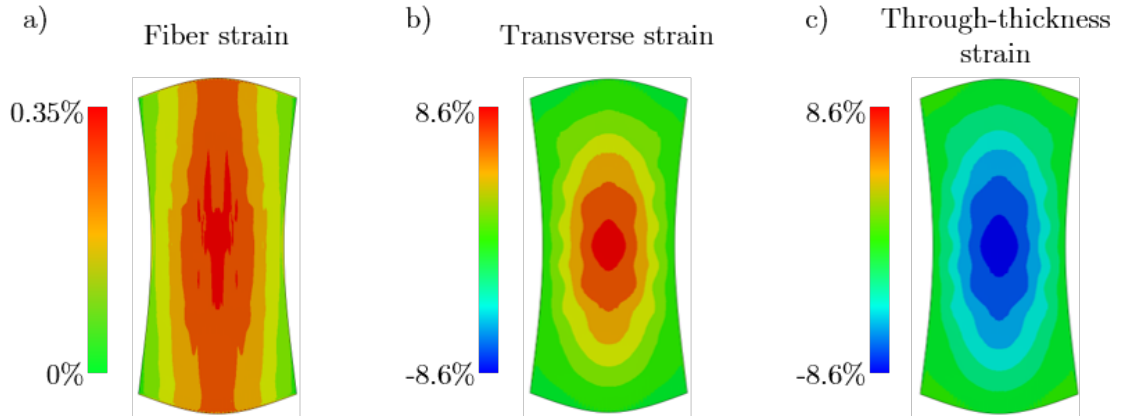

Figure 4.6: Small-strain contours for the (a) fiber, (b) transverse, and (c) through-thickness directions. Fiber strain is largest in the central third of the model, and it is smallest near the edges where fibers are most splayed. The model expands in the transverse direction and contracts in the through-thickness direction, which matches experimental observations for ACL and PT tension experiments [93, 97].

that specimen geometry – specifically fiber splay – significantly affects the global stress-strain relationships of the ovine PT and ACL regions by creating strain inhomogeneity, as shown in Fig. 4.6. Therefore, we suggest that macroscopic stress-strain measurements of ligaments and tendons are indicative of both material and structural properties and not well-suited to the identification of true material properties.

4.4.1 Impact on ACL graft selection

The effect of splay ratio on macroscopic mechanical behavior may explain the inconsistent reports on the relative material stiffness of the ACL and PT found in the literature. Studies by Danto and Woo [45] on rabbit ligaments and Chandrashekar et al. [39, 40] on human specimens reported larger apparent tangent moduli for PT grafts (middle third of the PT) than whole ACLs, using bone-ligament-bone samples. However, Ristaniemi et al. used a dumbbell-shaped punch to procure bovine samples of consistent geometry, and reported a slightly smaller (but not statistically different) tangent modulus for the PT than the ACL [130]. Butler et al. first reported a nearly two-fold larger tangent modulus for human bone-fascicle-bone PT samples

than ACLs [30], but later reported a much smaller tangent modulus for the medial half of the PT (smaller splay ratio) vs. whole ACL of cynomolgus monkey specimens [31].

The current results suggest that the PT is in fact not a stiffer material than the ACL. However, the PT graft (middle third of the PT) is probably a stiffer structure than the ACL. This point raises an important question for ACL reconstruction surgeons, tissue engineers, and biomechanists: does an ACL graft need to mimic a) the native ACL material properties, b) the force-extension relationship, or c) both? A similar force-extension relation is likely required to enable normal knee kinematics, but similar material properties may be necessary to mimic the native mechanical environment of cells and stimulate appropriate graft incorporation and remodeling. Answering this question is beyond the scope of the current work, but we suggest the use of more sophisticated characterization methods if material properties are of interest.

4.4.2 Broader relevancy

This work is applicable beyond its direct implications on the use of PT grafts for ACL reconstruction. For example, sex differences in macroscopic mechanical behavior of ligaments and tendons have been reported in the literature, and these may also be explained by the effect of splay geometry. Pardes et al. and Bonilla et al. reported smaller tangent moduli for the Achilles tendon and supraspinatus tendon, respectively, of male vs. female rats [25, 120]. However, in both studies, a consistent gauge length was used for specimens of both sexes, but male specimens had significantly larger cross-sectional area. This may have caused the male specimens to have a smaller splay ratio, and thus, to appear more compliant than female specimens. Similarly, Chandrashekar and colleagues reported a significantly larger tangent modulus for male vs. female ACLs, but their data also revealed a highly significant relationship between apparent tangent modulus and donor height [39], suggesting that geometrical effects may have obscured their measurements. In subsequent work, they noted that taller individuals tended to have PTs with larger

apparent tangent moduli [40]. Further adding to this discussion is a study by O'Brien and colleagues, which found no significant difference in the apparent tangent modulus of the PTs of men and women, nor that of boys and girls, but a nearly two-fold increase between adults and children [115]. Their results could be explained by a increase in splay ratio with age-related growth.

To be clear, measurable material property differences may exist between the ACL and PT [161], the sexes [61], or with age as a result of differences/changes in the collagen microstructure. However, true material characterization – that which accounts for the inherent strain inhomogeneity present in deformed ligaments/tendons – has yet to be performed. Current data is a reflection of both material and geometrical properties.

4.4.3 Additional notes on mechanical testing and study limitations

In addition to material properties, there are several factors that influence the macroscopic mechanical response of ligaments/tendons tested in a laboratory setting, but the present study considered only fiber splay geometry in the analysis of experimental data. For example, a previous computational study found that if the ligament is left attached to bones, small differences in enthesis shape and attachment angle can influence the macroscopic stress-stretch relationship [94]. To avoid the influence of enthesis geometry, one might be tempted to cut the ligament from the bones and clamp it directly. Unfortunately, this will result in significant underestimation of the tangent modulus [9]. Clamping creates end effects by transferring mechanical force from the testing rig to the specimen via shear tractions. Saint Venant's principle states that these end effects decay with a distance from the clamp known as the characteristic decay length. For isotropic materials, the decay length is about one specimen width. However, mathematical analysis performed by Horgan in 1972 found that the characteristic decay length is longest in the stiffest direction of anisotropic materials [72]. This was experimentally confirmed in 1976 by Arridge and Folkes, who found that the apparent tensile modulus of a transversely isotropic polyethylene film continued to increase with increasing length-to-width ratio up to

100:1 [13]. More recent studies from the biomechanics literature have directly supported this idea in the case of tendons and ligaments. Atkinson et al. reported that the apparent tangent modulus of the human patellar tendon increased with decreasing cross-sectional area [15] and Legerlotz et al. noted that the tangent moduli of rat tail tendon fascicles and bovine foot extensor tendon fascicles appeared to increase with decreasing cross-sectional area or increasing length [85]. Thus, whether ligaments and tendons are clamped or left attached to bones, a multitude of evidence suggests that both fiber splay and either clamping or enthesis curvature affect their macroscopic stress-strain behavior. The current study attempted to address the intersection of enthesis shape and fiber splay with the computational model, but curved enthesis shapes likely influenced the experimental results as well.

Grip-to-grip mechanical measurements are also affected by the compliance of the testing system. Movement of the bony ends within the testing grips and stretching of the loading train both contribute to the measured macroscopic strain. This may explain some of the quantitative discrepancy between the PT experimental data and the FE model (which was constructed using the stress-stretch data from the largest splay ratio PT sample). Experimentally measured apparent tangent moduli were likely underestimated, as they were probably measured at tissue strains below 5% due to compliance in our grip-to-grip measurements.

As previously mentioned, the splay ratio derived with the analytical model is directly proportional to the apparent tangent modulus only for the case of unconnected, linear elastic fibers at small stretch. In reality, collagen fibers exhibit nonlinear mechanical behavior and are bound by a compliant matrix composed of other extracellular matrix proteins [150]. For simplicity, these complexities were not considered in the analytical model. However, in contrast to the linear behavior assumed, the nonlinear behavior of collagen fibers would allow the splay ratio to continue to affect macroscopic mechanical behavior past the small stretch at which all fibers are engaged. The computational and experimental results of this study confirm this assertion. Still, because of this nonlinearity, the apparent tangent moduli of ligaments and tendons are likely not directly proportional to the splay ratio at finite strains. The linear and nonlinear regression analyses presented here (Fig. 4.5b-c)

are merely approximations to test whether splay ratio (i.e. geometry) significantly affects apparent tangent modulus measurements.

This study did not consider viscoelastic effects, although it is well-documented that ligaments exhibit time-dependent mechanical behavior [105]. Strain rate effects may explain why the PT appears to be more compliant than the ACL bundles at similar splay ratios; a consistent displacement rate (0.1 mm/s) was used in the experiments, yielding strain rates of $\sim 0.2\%$/s for the PT and $\sim 0.5\%$/s for the ACL bundles. The larger strain rate could make the ACL bundles appear to be stiffer than the PT. However, both strain rates are typically considered to be within the quasistatic regime.

It should also be noted that other models of fiber recruitment exist, which are primarily concerned with the gradual straightening of collagen fibers from their sinusoidal crimped state in the reference configuration as the tissue is stretched [79]. The current work was concerned with fiber recruitment from macroscopic fiber straightening due to fiber splay, rather than microscopic straightening due to fiber crimp.

Finally, this study used ovine ligaments as a model for human ligaments, both in the experimental work and analytical modeling. Ovine tibiofemoral anatomy and structure is considered to be sufficiently similar to that of humans [128]. Additionally, the finite element model examined a range of splay ratios, within which we would expect to find those of the human PT and ACL [125]. However, it would be valuable to validate the results of the experimental work presented here with data from human ligaments.

4.4.4 Future work

Our long-term goal is to study injury risk mitigation and surgical reconstruction using a whole-knee finite element model to perform *in silico* mechanistic studies [99]. This model requires fidelic material models for each of the tissues involved. However, standard curve-fitting methods for material characterization require an assumption of strain homogeneity, and this work and previous studies by our group and others have demonstrated the impracticality of obtaining homogeneous states

of strain in ligaments and tendons [75, 93–95, 97]. As a result, we have turned our attention to full-field methods, for which strain inhomogeneity is an asset, rather than a limitation. Full-field displacement measurement techniques like digital image correlation and displacement-encoded magnetic resonance imaging have been used by our group to measure full-surface and full-volume displacement fields [93, 97, 133]. Future work will aim to use full-field data and inverse methods – like finite element model updating (FEMU) [76] or the Virtual Fields Method (VFM) [16, 126] – to account for the strain inhomogeneity and relevant geometric features in the material characterization process.

CHAPTER 5

Constitutive Modeling of the Anterior Cruciate Ligament Bundles and Patellar Tendon with Full-Field Methods Detects Microstructural Differences

This chapter will be submitted for publication as a journal article and may then be referenced as:

Luetkemeyer, Callan M., Ulrich M. Scheven, Jonathan B. Estrada, and Ellen M. Arruda. Constitutive modeling of the anterior cruciate ligament bundles and patellar tendon with full-field methods detects microstructural differences.

5.1 Introduction

The anterior cruciate ligament (ACL) plays a vital role in healthy knee mechanics, providing both stability and flexibility required for walking, running, and athletic maneuvers. The ACL is also commonly torn, and surgical reconstruction is often required to restore an acceptable level of knee stability [10]. An ACL tear not only affects immediate quality of life, it also appears to be linked to the development of knee osteoarthritis within 10 years of injury [91, 113]. With the average age of those sustaining ACL injuries dropping [157, 158, 164], this inevitably means that many

afflicted young people are destined to endure chronic knee pain for the majority of their lives.

Thus, we are interested in developing injury prevention strategies by first identifying the factors which predispose certain individuals to ACL injury. A large number of potential injury risk factors have been identified by studies which correlate anatomical features with ACL injury incidence. For example, several studies report a positive correlation between ACL injury prevalence and smaller intercondylar notch width [26, 114, 146, 159]. However, similar studies have found conflicting results [5, 92, 154, 156]. In clinical studies, it is difficult to consider the large number of anatomical variables which may contribute to injury risk, and even more difficult to parse out the effect of a single variable.

A computational approach, such as finite element (FE) analysis, can be used to evaluate the injury risk associated with various factors in a systematic and deterministic way; factors which cause greater deformation concentrations will put an individual at greater risk of ACL failure. This approach is not without its challenges, however, as realistic model predictions require accurate model inputs. In addition to ACL geometry (which can be obtained with magnetic resonance imaging) and knee kinematics (which can measured with motion capture [77] or inertial measurement units [155]), these models also need to be given material properties, in the form of a constitutive equation which describes the stress-deformation relationship of the ACL at the material level. However, despite decades of research, even basic material properties elude scientific consensus [122].

Ligaments derive their material properties from extracellular matrix (ECM) components. Type-I collagen fibers are relatively stiff protein structures that give rise to an anisotropic phase, as they are mostly aligned in the predominant direction of loading, while elastin, proteoglycans, and other more compliant proteins constitute the "ground substance," which is believed to behave as an isotropic polymer [101]. Furthermore, the ACL is actually composed of two ligaments: the anteromedial (AM) bundle, which primarily restricts anterior tibial translation, and the posterolateral (PL) bundle, which predominantly restrains tibial rotation [7]. Both the AM and PL regions are composed of essentially the same ECM components. However,

the collagen fibers in the PL region tend to be slightly less perfectly aligned with their neighbors, or have more variation about the mean fiber direction for a given material point [140, 141], which likely gives it greater torsional stiffness. This distribution about a mean fiber direction is also seen in arteries, and its relevance led to an addendum on the popular Holzapfel-Gasser-Ogden (HGO) constitutive model [71]: the addition of κ, a material parameter which describes the degree of collagen fiber alignment [52].

The standard method used to calibrate material models relies on achieving nearly homogeneous states of deformation and nearly uniform stress distributions at the loaded boundaries. The material parameters can then be found by fitting a chosen material model to the homogeneous stress-strain curve. For ligaments, this method has been used to calibrate material models with homogenized measurements (typically grip-to-grip) of stress and deformation from uniaxial mechanical tests, assuming that the strain is entirely homogeneous and uniaxial. However, full-field displacement measurements have shown that deformation is not homogeneous nor uniaxial; shear and transverse strains are consistently large and spatially inhomogeneous [93, 97]. Recently, we have shown that fiber splay (the tendency of ligament collagen fibers to spread as they insert into bone) creates deformation heterogeneity, which affects the global stress-stretch response of ligaments. Similarly, small variations in the shape of the enthesis (ligament attachment to bone) can affect the macroscopic response [94]. For applications where true material properties are desired – such as FE modeling – strain inhomogeneity and the structural features that create it (e.g. fiber splay and enthesis shape) must be taken into account.

Therefore, we turn our attention to full-field characterization methods, for which deformation heterogeneity is an asset, rather than a detriment. Instead of measuring the global displacement during a mechanical test, the full displacement field is measured and used to calibrate a chosen constitutive model. For anisotropic materials/tissues in particular, full-field methods have the potential to make all material parameters identifiable with a single test. Standard modeling methods would require multiple mechanical tests (each with homogeneous strain) in different directions to make all material parameters identifiable. Conversely, with full-field methods, a sin-

gle heterogeneous strain field can provide the material model calibration scheme with information from various modes of deformation.

The first step is to experimentally measure the deformation field. Digital image correlation (DIC) is the most commonly used displacement mapping technique [117]. However, it is limited to surface measurements and an assumption about through-thickness deformations, usually plane stress, while the heterogeneity in ligament deformation is fully three dimensional. Digital volume correlation (DVC) is a full volume extension of DIC, but it requires a trackable internal pattern, usually inherent microstructural features [131]. A third option for experimentally measuring displacement fields is displacement-encoded magnetic resonance imaging (MRI). MRI images contain complex valued image data. In anatomical imaging, the *magnitude* of this complex data is used to differentiate between tissues based on their relative density. In displacement imaging, the *phase* of the data in each voxel is directly proportional to the displacement between stretched (encode) and reference (decode) configurations. In this study, the alternating pulsed field gradient stimulated echo imaging (APGSTEi) sequence proposed by Scheven and colleagues is used [133].

Full-field displacement measurements can be used to calibrate material models using full-field inverse methods. Several full-field inverse methods exist, such as finite element model updating, the equilibrium gap method, and the constitutive equation gap method, but the Virtual Fields Method (VFM) has shown both robustness and computational efficiency in comparison to other methods [104]. The VFM is based on the principle of virtual work. A cost function is constructed using the weak form of the equilibrium equation, and the best set of material parameters is found by minimizing the difference between the internal virtual work and external virtual work. For a complete review of the VFM and examples of its use, the reader is directed to the work of Pierron and Grédiac [123].

In previous work, material models of silicone elastomers were calibrated using displacement-encoded MRI with APGSTEi and inverse characterization with full-volume VFM to validate our material characterization pipeline [48]. In this study, we use this set of full-field methods to build constitutive models of the ovine ACL bundles, as well as the patellar tendon (PT), a commonly used graft for surgical

reconstruction of the ACL. The implementation of these methods presented in this work account for heterogeneous deformation, heterogeneous material direction (fiber splay), and curved, 3D displacement boundary conditions (enthesis shapes).

5.2 Methods

5.2.1 Overview of material model calibration with the Virtual Fields Method

The stress-deformation relationship of a nonlinear elastic material can be modeled with a hyperelastic constitutive equation, typically given in the form of a strain energy density function (U), a scalar-valued function which relates the internal energy in the material to the mechanical deformation. For finite strains, deformation is described by the deformation gradient tensor,

$$\mathbf{F}(\mathbf{X}) = \frac{d\mathbf{x}}{d\mathbf{X}} = \frac{d\mathbf{u}}{d\mathbf{X}} + \mathbf{1}, \tag{5.1}$$

where $\mathbf{X}$ and $\mathbf{x}$ are the position vectors of the material point in the reference and deformed configurations, respectively, $\mathbf{u}$ is the displacement vector, and $\mathbf{1}$ is the identity tensor. The first Piola-Kirchhoff stress ($\mathbf{\Pi}$) is defined as the tensor derivative of the strain energy density function with respect to the deformation gradient tensor,

$$\mathbf{\Pi}(\mathbf{F}, \mathbf{a}_0, \boldsymbol{\xi}) = \frac{\partial U(\mathbf{F}, \mathbf{a}_0, \boldsymbol{\xi})}{\partial \mathbf{F}} \tag{5.2}$$

where $\mathbf{a}_0$ is a unit vector describing the material direction (i.e., collagen fiber direction) in the reference configuration, and $\boldsymbol{\xi}$ is a vector of constitutive parameters (i.e., material properties) which we seek to find. The first Piola-Kirchhoff stress is a useful stress quantity in experimental mechanics, as it relates the force in the deformed configuration to the undeformed (reference) cross-sectional area, which is how these quantities are generally measured.

In this study, hyperelastic material models were calibrated using finite deformation measurements at static equilibrium (no acceleration) in each specimen's ref-

erence configuration (Ω_0). It was assumed that body forces (e.g. gravity) were negligible. Thus, as described by Promma et al. [126], the following weak form of the equilibrium equation was used,

$$\int_{\Omega_0} \mathbf{\Pi} : \frac{d\mathbf{u}^*}{d\mathbf{X}} dV - \int_{\partial\Omega_0} (\mathbf{\Pi}\,\mathbf{n}) \cdot \mathbf{u}^* dS = 0, \tag{5.3}$$

where $\mathbf{u}^*$ is a virtual displacement vector (also known as a trial function, test function, or weighting function in the finite element method) and $\mathbf{n}$ is the vector normal to the surface $\partial\Omega_0$. This virtual displacement field can be *any* vector field that 1) is constant along boundaries with constant displacement (i.e., obeys Dirichlet boundary conditions) and 2) is kinematically admissible (i.e., continuous). However, each possible virtual field will weight the measured fields differently. The fields chosen should probe orthogonal modes of deformation to improve identifiability of parameters that contribute to particular modes of deformation (more on this in section 2.6).

If external tractions ($\mathbf{\Pi}\,\mathbf{n}$) are applied only along surfaces ($\partial\Omega_0$) with constant displacement ($\mathbf{u}$) (i.e. boundary conditions are Cauchy boundary conditions), the virtual displacement fields ($\mathbf{u}^*$) must also be constant along these boundaries. Thus, Eq. 5.3 becomes

$$\int_{\Omega_0} \mathbf{\Pi} : \frac{d\mathbf{u}^*}{d\mathbf{X}} dV - F u^*_{\partial\Omega_0} = 0 \tag{5.4}$$

where $F = \int_{\partial\Omega_0} (\mathbf{\Pi}\,\mathbf{n}) dS$ is the resultant applied force (which is measured experimentally) and $u^*_{\partial\Omega_0}$ is the constant virtual displacement (in the direction of the applied force F) of all points along the surface $\partial\Omega_0$.

To find constitutive parameters, a nonlinear sum of squares cost function is constructed based on Eq. 5.4 using multiple stretch states (required to fit nonlinearity) and multiple virtual fields (to extract different kinds of stress-deformation information):

$$\phi \equiv \sum_{i=1}^{n_\lambda} \sum_{j=1}^{n_{VF}} \frac{\left(\int_{\Omega_0} \mathbf{\Pi}^{(i)} : \frac{d\mathbf{u}^{*(j)}}{d\mathbf{X}} dV - F^{(i)} u^{*(j)}_{\partial\Omega_0} \right)^2}{F^{(i)} u^{(i)}_{\partial\Omega_0}} \tag{5.5}$$

where n_λ is the number of stretch states or measured deformation fields and n_{VF} is the number of virtual fields used, which can be different for each stretch state. The difference between the internal and external virtual work was normalized by the measured external work ($F^{(i)}u^{(i)}_{\partial\Omega_0}$) at each stretch state to balance the influence of each measured deformation field on the cost function. In this work, the least squares cost function (ϕ) was minimized with respect to the unknown vector of constitutive parameters ($\boldsymbol{\xi}$) using the built-in Matlab (The MathWorks, Inc., Natick, MA) function `lsqnonlin` to find a best estimate for ligament material properties. A range of initial conditions were used to ensure robust convergence.

Thus, the VFM relies on two full-field inputs: the first Piola-Kirchhoff stress fields ($\mathbf{\Pi}$), which depend on the sought constitutive parameters ($\boldsymbol{\xi}$), and virtual displacement fields ($\mathbf{u}^*$). The construction of virtual fields for this study is described in section 5.2.6. The stress field is dependent on the measured deformation field (discussed in section 5.2.3), the material model formulation (discussed in section 5.2.4), and in this particular study, a description of material direction heterogeneity (discussed in section 5.2.5).

5.2.2 Specimen preparation

Five ovine tibiofemoral joints were acquired from a local abattoir, where meat was removed before wrapping the knee in cellophane and storing it at 6°C. The knee was further dissected in the laboratory within 24 hours. All soft tissues other than the ACL bundles were removed, and the natural separation of the bundles near the tibial insertion was identified. A pair of forceps was inserted into this separation, and used to break any weak connective tissue between the bundles up to the femoral attachment. Small bone blocks were cut out of the tibia and femur using a reciprocating hand saw (Dremel, Racine, WI), each containing an enthesis of one of the ACL bundles. Custom grips (made of Ultem) contained a cylindrical hole tapped with 5/8"-11 threads, into which moldable heat-set thermoplastic (Polly Plastics, Midland, MI) was deposited. While the thermoplastic was still warm, the bone blocks were submerged into the thermoplastic-filled grips. It was ensured that the

thermoplastic covered the bone block edges but did not restrict ligament movement. Specimens were stored in 1X phosphate buffered saline (Thermo Fisher Scientific, Inc., Waltham, MA) at 6°C for 12 to 96 hours.

5.2.3 Full-volume deformation measurements with displacement-encoded MRI

Full-volume displacement maps were acquired for each specimen (five of each ligament) at five stretch states, using alternating pulsed field gradient stimulated echo imaging (APGSTEi), described in detail in previous publications [133]. For mechanical testing, sample grips were attached to a fixed loading chamber at one end and a long actuation rod on the other. To prevent specimen desiccation, a nitrile sleeve was stretched over both grips to form a small, airtight barrier around the hydrated tissue. The loading chamber (with a mounted specimen inside) was then placed in the bore of a 7T MRI magnet. The materials used in or near the magnet were all MRI-compatible; the loading chamber and actuation rod were made of Ultem, while the tube which housed the actuation rod was a G10 fiberglass composite with Delrin bearings. Actuation was achieved with a linear stepper motor (L5918S2008-T10X2-A50, Nanotec Electronic GmbH & Co. KG, Germany), kept several feet away from the magnet bore. Force measurements were made with a load cell (LCM300, Futek Advanced Sensor Technology Inc., Irvine, CA) in line with the actuation rod.

Specimens were pre-loaded to either 5 N (AM and PL regions) or 10 N (PT) before being subjected to cyclic loading to 3 mm (AM and PL regions) or 6 mm (PT) at 1 Hz for 15 mins. This was done to improve repeatability by minimizing viscoelastic effects and allowing settling of the bone within the grip mold, as has been done in the majority of biomechanics research [63, 132]. After cycling, the reference configuration was established as the position at 5 and 10 N pre-load for AM/PL regions and PTs, respectively. Anatomical images were acquired using a spin-echo multislice acquisition at the reference state.

Using our previously published pulse sequence, APGSTEi, synchronized with stepper motor-driven actuation, the change in phase of proton magnetic moments

throughout the sample was measured between reference and deformed configurations [133]. This change in phase (θ_i) is directly related to the displacement $(x_e - x_d)_i$ of protons during the time interval between encoding and decoding gradient pulses by $\theta_i = 2\pi\gamma\delta g_i(x_e - x_d)_i$, where γ is the gyromagnetic ratio, g_i is the gradient pulse amplitude for the ith Cartesian direction, and δ is the effective duration of the gradient pulse in the APGSTEi sequence.

It was imperative that the encoding wavelength ($\lambda_i = 1/\gamma\delta g_i$) for each direction was large enough to avoid large phase differences ($\sim \pi/32$) between adjacent voxels in regions with strain concentrations (i.e. to avoid aliasing), but smaller encoding wavelengths should yield better signal to noise. Through experimentation during pilot testing, appropriate encoding wavelengths were determined for each specimen type as a function of applied displacement. For AM and PL bundles, these were $0.5(x_e - x_d)_i$ in the readout ($\mathbf{e}_2$) direction and $0.75(x_e - x_d)_i$ in the phase encode ($\mathbf{e}_1$) and slice select ($\mathbf{e}_3$) directions. The encoding wavelengths used for PT specimens were half those used for AM and PL bundles.

Phase measurements were smoothed using a custom complex blurring filter with kernel size 5 and then unwrapped to yield full-volume displacement fields using a custom reliability-weighted implementation of the robust, 3D unwrapping algorithm proposed by Abdul-Rahman and colleagues [1]. Displacement fields were then masked (see section 5.2.5) with NaNs outside the region of interest (ROI), before being smoothed with a 3D Gaussian filter with kernel size 5 using the Matlab function `ndnanfilter` [3]. This prevented noise outside the ROI from influencing the filtering process. The displacement fields were numerically differentiated (via central difference) to compute deformation gradient tensor fields (see Eq. 5.1), from which Green-Lagrange strain fields were computed as

$$\mathbf{E} = \frac{1}{2}(\mathbf{C} - \mathbf{1}) \tag{5.6}$$

where $\mathbf{C}$ is the right Cauchy-Green tensor, defined as

$$\mathbf{C} = \mathbf{F}^\intercal\mathbf{F}. \tag{5.7}$$

The transition of phases to displacements to strains is depicted for an AM region in Fig. 5.1. Deformation fields were acquired at motor displacements of 0.75, 1.5, 2.25, 3.0, and 3.75 mm for AM and PL bundles and 1.5, 3.0, 4.5, 6, and 7.5 mm for PT samples. For the ACL bundles, the maximum displacement (3.75 mm) produced maximum forces around 200 N, or 30-50% of the ultimate tensile load [106].

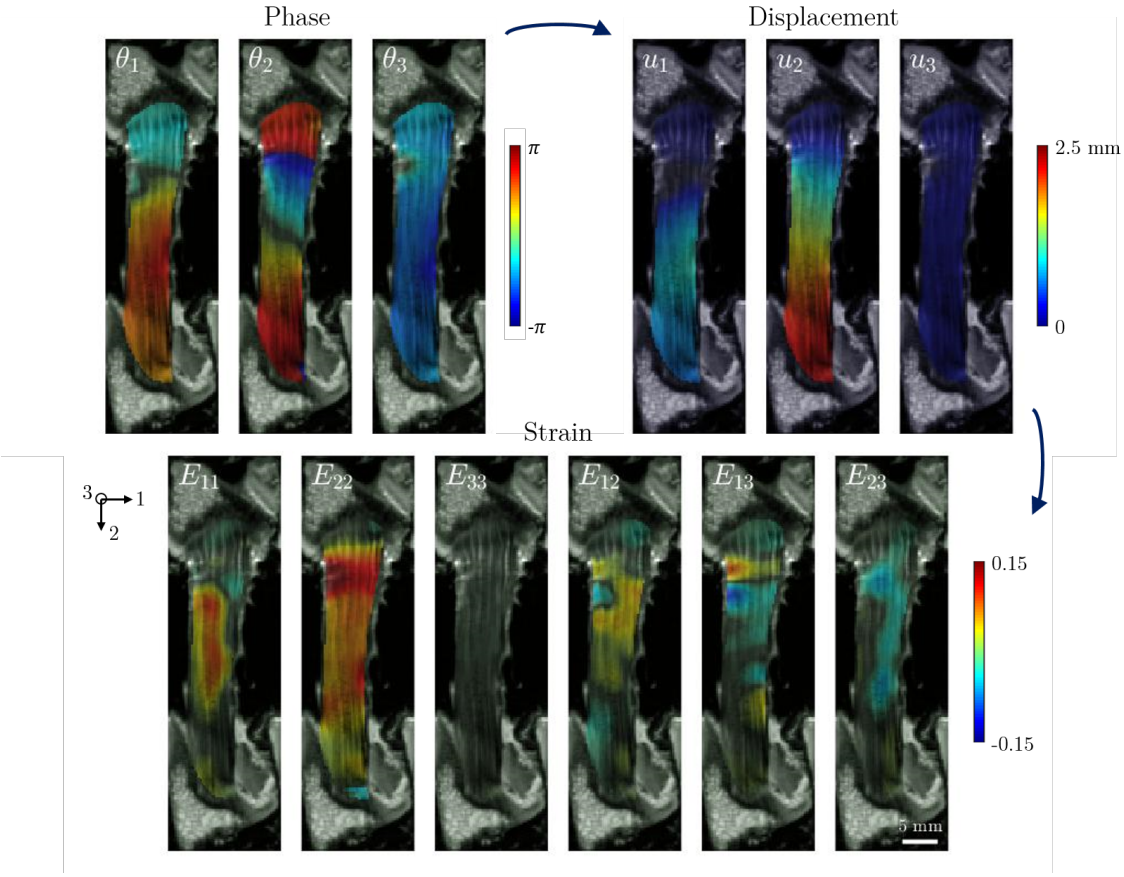

Figure 5.1: Phase measurements in each direction are shown for a slice through an example AM bundle, stretched to 3.75 mm (motor displacement). The encoding wavelengths used here were $\lambda = [2.8, 1.9, 2.8]$ for the phase encode ($\mathbf{e}_1$), readout ($\mathbf{e}_2$), and slice select ($\mathbf{e}_3$) directions, respectively. The derivatives of the displacement fields were used to compute the full Lagrange strain tensor ($\mathbf{E}$) throughout the volume of each specimen. For all plots, the colormap opacity scales directly from zero.

5.2.4 Material model formulations

Because the material characterization of ligaments is still in its infancy, it remains unclear which constitutive model best represents the real material physics. Thus, in this study, three strain energy density functions were employed, two of which are invariant-based models. For these anisotropic, invariant-based models with a single fiber family, the first Piola-Kirchhoff stress ($\mathbf{\Pi}$) can be derived from the strain energy density function (U) using

$$\mathbf{\Pi}(\mathbf{F}, \mathbf{a}_0, \xi) = 2\left[\left(\frac{\partial U}{\partial I_1} + \frac{\partial U}{\partial I_2} I_1\right)\mathbf{F} - \frac{\partial U}{\partial I_2}\mathbf{B}\mathbf{F} + I_3\frac{\partial U}{\partial I_3}\mathbf{F}^{-\intercal} + \frac{\partial U}{\partial I_4}\mathbf{F}\left(\mathbf{a}_0 \otimes \mathbf{a}_0\right)\right] \tag{5.8}$$

where $\mathbf{a}_0$ is the local material direction in the reference configuration (see Fig. 5.2), $\mathbf{B}$ is the left Cauchy-Green tensor,

$$\mathbf{B} = \mathbf{F}\mathbf{F}^{\intercal}, \tag{5.9}$$

and I_1, I_2, I_3, and I_4 are the invariants of the right Cauchy-Green tensor (Eq. 5.7),

$$\begin{aligned} I_1 &= \operatorname{tr}\mathbf{C} \\ I_2 &= \tfrac{1}{2}\left[(\operatorname{tr}\mathbf{C})^2 - \operatorname{tr}\mathbf{C}^2\right] \\ I_3 &= \det\mathbf{C} \\ I_4 &= \mathbf{a}_0\mathbf{C}\mathbf{a}_0. \end{aligned} \tag{5.10}$$

The first material model used was the classic Holzapfel-Gasser-Ogden (HGO) model [70] with the addition of a fiber dispersion term [52]. The HGO model has a neo-Hookean isotropic phase and an exponential-based anisotropic phase,

$$\begin{aligned} U_{\mathrm{HGO}}(\mathbf{F}, \mathbf{a}_0) = {} & C_{10}\left(J^{-2/3}I_1 - 3\right) \\ & + \frac{k_1}{2k_2}\left(\exp\left[k_2\left(\kappa I_1 + (1-3\kappa)I_4 - 1\right)^2\right] - 1\right) + \frac{B}{2}(J-1)^2 \end{aligned} \tag{5.11}$$

where C_{10} is the isotropic shear modulus, B is the bulk modulus (a measure of the volumetric stress-strain behavior), k_1 represents the stiffness of the fiber phase, k_2 describes collagen fiber nonlinearity, and κ is a measure of the degree of collagen

fiber alignment, ranging from 0 (perfectly aligned) to 1/3 (isotropically distributed). J is the determinant of the deformation gradient tensor ($J = \det \mathbf{F}$). It then follows from Eqs. 5.8 and 5.10 that the HGO model for the first Piola-Kirchhoff stress is

$$\begin{aligned}\mathbf{\Pi}_{\text{HGO}}(\mathbf{F}, \mathbf{a}_0) = 2C_{10}J^{-2/3}\left(\mathbf{F} - \frac{1}{3}I_1\mathbf{F}^{-\intercal}\right) + BJ(J-1)\mathbf{F}^{-\intercal} \\ + 2k_1 E \exp\left[k_2 E^2\right](\kappa\mathbf{B} + (1-3\kappa)(\mathbf{F}\mathbf{a}_0 \otimes \mathbf{F}\mathbf{a}_0))\,\mathbf{F}^{-\intercal}\end{aligned} \tag{5.12}$$

where $E = \kappa I_1 + (1-3\kappa)I_4 - 1$. For the HGO model, the material constants are $\boldsymbol{\xi}_{\text{HGO}} = [C_{10}, B, k_1, k_2, \kappa]$.

In previous work, we proposed a modification to the HGO model with a Macintosh 8-chain isotropic phase (HGO-MAC) CITE, as the Neo-Hookean constitutive form in the HGO model cannot capture the characteristic concave up relationship between stress and stretch for the isotropic phase [101]. The HGO-MAC model provides such a material model form at the expense of extra parameters,

$$\begin{aligned}&U_{\text{HGO-MAC}}(\mathbf{F}, \mathbf{a}_0) \\ &= C_r\left(\frac{3L^2}{12AL - 4Ar_0\sqrt{3I_1}}\right. \\ &\qquad \left. + \ln\left[\frac{L - r_0\sqrt{I_1/3}}{L^2 - 2AL + 2Ar_0\sqrt{I_1/3}}\right] - \frac{L^2 r_0\left(L^2 + 6A(r_0 - L)\right)}{12A(L-r_0)^2\left(L^2 + 2A(r_0 - L)\right)}\ln(J)\right) \\ &\quad + \frac{k_1}{2k_2}\left(\exp\left(k_2\left(\kappa I_1 + (1-3\kappa)I_4 - 1\right)^2\right) - 1\right) + \frac{B}{2}(J-1)^2\end{aligned} \tag{5.13}$$

where the isotropic material parameters are: C_r (the rubbery modulus), L (the chain contour length), A (the persistence length), and r_0 (the end-to-end length of the Macintosh chains in the reference configuration). The anisotropic and bulk terms are identical to those in the HGO model. In terms of stress, this equation becomes

$$\begin{aligned}\mathbf{\Pi}_{\text{HGO-MAC}}(\mathbf{F}, \mathbf{a}_0) = &\frac{9C_r\rho_0\Lambda^2\left(\sqrt{3}\Lambda(\Lambda-6) + 6\rho_0\sqrt{I_1}\right)}{4\sqrt{I_1}\left(\rho_0\sqrt{3I_1} - 3\Lambda\right)^2\left(3\Lambda(\Lambda-2) + 2\rho_0\sqrt{3I_1}\right)}\mathbf{F} \\ &- \frac{C_r\rho_0\Lambda^2\left(\Lambda^2 + 6(\rho_0 - \Lambda)\right)}{12\left(\Lambda - \rho_0\right)^2\left(\Lambda^2 + 2(\rho_0 - \Lambda)\right)}\mathbf{F}^{-\intercal} + BJ(J-1)\mathbf{F}^{-\intercal} \\ &+ 2k_1 E\exp\left[k_2 E^2\right](\kappa\mathbf{B} + (1-3\kappa)(\mathbf{F}\mathbf{a}_0 \otimes \mathbf{F}\mathbf{a}_0))\,\mathbf{F}^{-\intercal}\end{aligned} \tag{5.14}$$

where $\Lambda = L/A$ and $\rho_0 = r_0/A$. Thus, the constitutive parameters present in the HGO-MAC model are $\boldsymbol{\xi}_{\text{HGO-MAC}} = [C_r, \Lambda, \rho_0, B, k_1, k_2, \kappa]$. Note that to calibrate the HGO-MAC model using $\mathbf{\Pi}$ and $\mathbf{F}$, the contour, end-to-end, and persistence lengths reduce to just two parameters (Λ and ρ_0) based on their ratios.

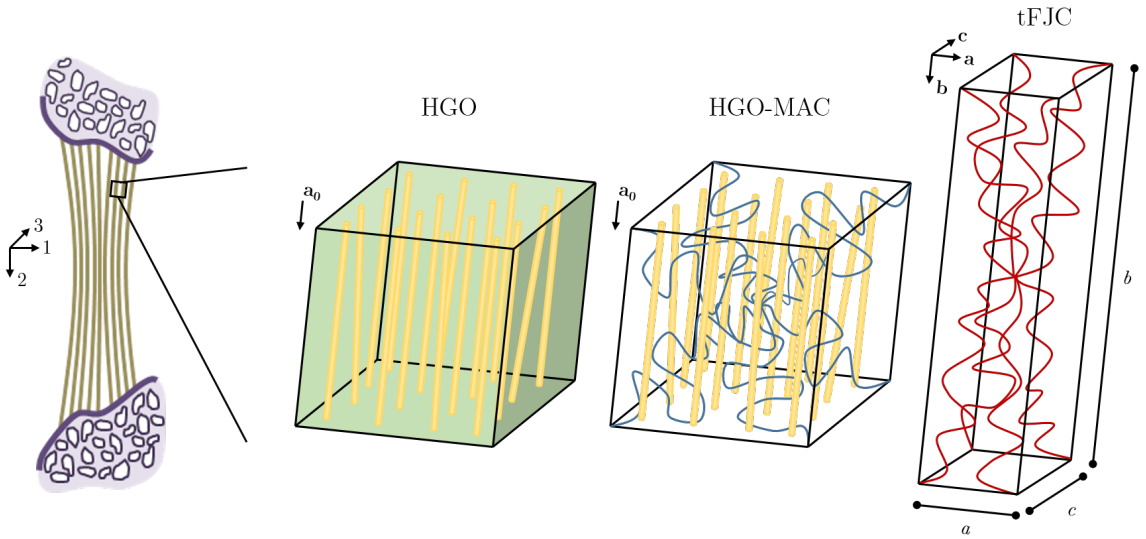

Figure 5.2: Three constitutive models were used in this study to model the material behavior of ligaments; representative volume elements (RVEs) for each are shown here for a material point in the local material orientation relative to the global coordinate system. The HGO model (neo-Hookean isotropic phase) and the HGO-MAC model (Macintosh 8-chain isotropic phase) derive their anistropy from an exponential fiber phase with variation about the mean fiber direction ($\mathbf{a}_0$). In contrast, the tFJC model derives anisotropy from the relative dimensions of the RVE itself, which are sought material parameters.

Lastly, we used a transversely isotropic version of the freely jointed 8-chain model, a statistical mechanics model originally proposed by Arruda and Boyce [14]. The original model was expanded to an orthotropic formulation by Bischoff et al. [23],

which we employed as a transversely isotropic freely jointed 8-chain model (tFJC),

$$U_{\text{tFJC}}(\mathbf{F},\mathbf{a},\mathbf{b},\mathbf{c}) = U_0 + \frac{C_r}{4}\left(N\sum_{i=1}^{4}\left[\frac{\rho^{(i)}}{N}\beta_\rho^{(i)} + \ln\left(\frac{\beta_\rho^{(i)}}{\sinh\beta_\rho^{(i)}}\right)\right] - \frac{\beta_P}{\sqrt{N}}\ln\left(\lambda_{\mathbf{a}}^{a^2}\lambda_{\mathbf{b}}^{b^2}\lambda_{\mathbf{c}}^{c^2}\right)\right) + \frac{B}{2}(J-1)^2 \tag{5.15}$$

where U_0 is a constant (representing an internal energy contribution from sources other than deformation), $\sqrt{N} = \frac{1}{2}\sqrt{a^2+b^2+c^2}$ is the root mean square chain length in the undeformed configuration, $\rho^{(i)}$ is the deformed chain length of the ith chain. The stretches along the principal material axes $(\mathbf{a},\mathbf{b},\mathbf{c})$ are denoted by $\lambda_{\mathbf{a},\mathbf{b},\mathbf{c}}$, computed using

$$\begin{aligned}\lambda_{\mathbf{a}} &= \sqrt{\mathbf{a}^\intercal\cdot\mathbf{C}\cdot\mathbf{a}}\\ \lambda_{\mathbf{b}} &= \sqrt{\mathbf{b}^\intercal\cdot\mathbf{C}\cdot\mathbf{b}}\\ \lambda_{\mathbf{c}} &= \sqrt{\mathbf{c}^\intercal\cdot\mathbf{C}\cdot\mathbf{c}}.\end{aligned} \tag{5.16}$$

The degree of anisotropy is controlled by the dimensions of the representative volume element (RVE), given by a, b, and c (see Fig.5.2). In this work, the material was assumed to be transversely isotropic, with the collagen fibers aligned in the direction of $\mathbf{b}$, so that $a = c$, and b represented the longest edge of the RVE. The functions $\beta_\rho^{(i)}$ and β_P are based on the probability density functions of freely jointed chains,

$$\beta_\rho^{(i)} = \mathcal{L}^{-1}\left(\frac{\rho^{(i)}}{N}\right) \tag{5.17}$$

$$\beta_P = \mathcal{L}^{-1}\left(\frac{P}{N}\right) \tag{5.18}$$

where P is the reference chain length ($P = \sqrt{N}$) and $\mathcal{L}^{-1}(x) = \cosh x - \frac{1}{x}$ is the inverse Langevin function, for which the Padé approximation was used [44]. Finally, the tFJC model for the first Piola-Kirchhoff stress is

$$\mathbf{\Pi}_{\text{tFJC}}(\mathbf{F},\mathbf{a},\mathbf{b},\mathbf{c}) = \mathbf{F}\bar{\mathbf{S}}_{\text{tFJC}} + BJ(J-1)\mathbf{F}^{-\intercal} \tag{5.19}$$

where $\bar{\mathbf{S}}_{\text{tFJC}}$ is the isochoric portion of the second Piola-Kirchhoff stress, given in

indicial notation as

$$\bar{S}_{\mathrm{tFJC}_{ik}} = \left[\frac{C_r}{4}\left(\sum_{i=1}^{4}\left[\frac{P_j^{(i)}P_k^{(i)}}{\rho^{(i)}}\beta_\rho^{(i)}\right] - \frac{\beta_P}{\sqrt{N}}\left(\frac{a^2}{\lambda_{\mathbf{a}}^2}a_j a_k + \frac{b^2}{\lambda_{\mathbf{b}}^2}b_j b_k + \frac{c^2}{\lambda_{\mathbf{c}}^2}c_j c_k\right)\right)\right] \quad (5.20)$$

where $P_j^{(i)}$ is the jth component of the end-to-end position vector for the ith chain in the reference configuration, given by

$$\begin{aligned}
\mathbf{P}^{(1)} &= \tfrac{a}{2}\mathbf{a} + \tfrac{b}{2}\mathbf{b} + \tfrac{c}{2}\mathbf{c} \\
\mathbf{P}^{(2)} &= \tfrac{a}{2}\mathbf{a} + \tfrac{b}{2}\mathbf{b} - \tfrac{c}{2}\mathbf{c} \\
\mathbf{P}^{(3)} &= \tfrac{a}{2}\mathbf{a} - \tfrac{b}{2}\mathbf{b} + \tfrac{c}{2}\mathbf{c} \\
\mathbf{P}^{(4)} &= \tfrac{a}{2}\mathbf{a} - \tfrac{b}{2}\mathbf{b} - \tfrac{c}{2}\mathbf{c}.
\end{aligned} \quad (5.21)$$

The constitutive constants required to implement the tFJC model, then, are $\boldsymbol{\xi}_{\mathrm{tFJC}} = [C_r, B, a, b]$, as $c = a$. The reader is directed to the work of Marchi and colleagues [101] for a more thorough overview and derivation of these constitutive equations. Note that this study used a slight variation of the tFJC model: namely, a linear bulk deformation term.

5.2.5 Construction of data masks and fiber direction fields

Full-volume data masks were constructed to identify the region of interest for each specimen, as well as the shape of both entheses. A custom application was developed in Matlab in which the user could parse through anatomical image slices and select points defining the edges of the specimen. The user identified each point as an enthesis point (tibial or femoral/patellar) or a free edge point. Together, all points were used to construct a point cloud from which a 3D mask was created using the `alphaShape` and `inShape` built-in Matlab functions.

A fiber field was constructed for each specimen based on the shape of the edges of the data mask. For each slice through the thinnest dimension of the specimen, a 2D second-order polynomial was fit to both sets of points along the free edges (non-enthesis boundaries). The analytic derivatives of these equations were used to specify the in-plane components of the material direction vector at the boundary points.

The in-plane fiber direction vector for interior points was then found using linear interpolation. Similarly, for each slice through the widest dimension of the specimen, a first-order polynomial (no splay was assumed in this direction) was fit to both sets of points along both ligament edges. The slopes of both lines were used to determine the in-plane components of the fiber direction vector at the boundary points, and linear interpolation was used to find the interior material direction vectors. Since both in-plane material direction fields have an axial component, both vector components for the two sets of 2D vector fields were normalized relative to the axial component. The two sets of material direction fields were then combined to obtain a single fiber field containing material direction vectors with components in all three Cartesian directions. Each vector within the field was then normalized by its magnitude to make unit vectors to describe the fiber direction in the reference configuration ($\mathbf{a}_0$).

For the tFJC model, three material direction vectors are required (see Fig. 5.2), and research by Marchi and colleagues showed the importance of the definitions of the transverse material directions in a transversely isotropic FJC model [101]. Thus, for each voxel, a transformation matrix $\mathbf{T}$ was constructed using the components of $\mathbf{a}_0 = [u, v, w]^\intercal = \mathbf{T}\mathbf{e}_2 = \mathbf{b}$ to determine the material vectors $\mathbf{a} = \mathbf{T}\mathbf{e}_1$ and $\mathbf{c} = \mathbf{T}\mathbf{e}_3$:

$$\mathbf{T} = \begin{bmatrix} \cos\psi_1 & \sin\psi_1 & 0 \\ -\cos\psi_2 \sin\psi_1 & \cos\psi_2 \cos\psi_1 & \sin\psi_2 \\ \sin\psi_2 \sin\psi_1 & -\sin\psi_2 \cos\psi_1 & \cos\psi_2 \end{bmatrix} \tag{5.22}$$

where $\psi_1 = \arcsin(u)$ and $\psi_2 = \arccos\left(\frac{v}{\cos\psi_1}\right)$.

5.2.6 Definition of virtual fields based on shapes of bone-ligament boundaries

The VFM cost function uses one or more virtual displacement fields, akin to test functions used in the finite element method; *any* vector field can be used as a virtual displacement field if it 1) adheres to the boundary conditions of the problem (i.e., is constant along boundaries with constant displacement) and 2) is kinematically ad-

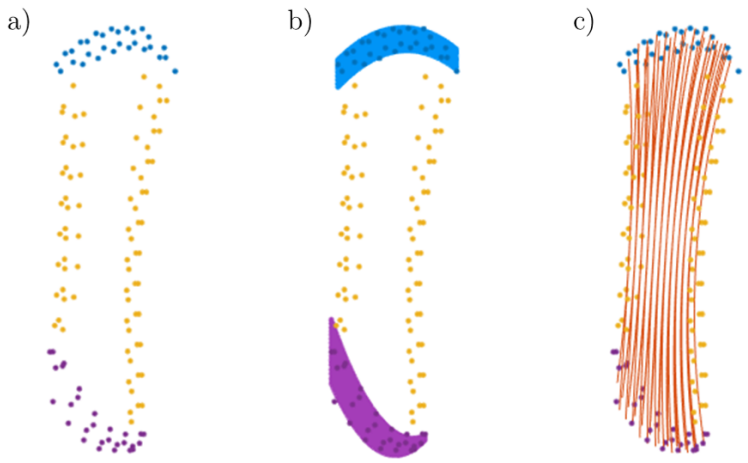

Figure 5.3: Using high resolution spin-echo multi-slice images, a point cloud was manually created for each specimen, as shown in (a) for the same example AM bundle in Fig. 5.1. The points defining both entheses (femoral in blue and tibial in purple) were used to construct 3D polynomial models (b) of the surfaces with displacement boundary conditions (as discussed in Section 5.2.6). The point clouds were also used to construct volumetric data masks that served as templates for defining the fiber direction field (c), depicted here with red streamlines.

missible. It need not be related to the true displacement field, nor does it need to be realistic or physically plausible. However, different virtual fields will extract different kinds of information. For example, a virtual displacement field that looks something like uniaxial extension in the fiber direction will largely extract information about the normal stress-deformation relationship of the anisotropic phase, yielding better estimates of the material properties governing the fiber direction response. Conversely, a virtual displacement field that has more variation in displacement along a transverse direction (orthogonal to the fibers) will give better estimates of constitutive parameters that describe the response of the isotropic phase. Of course, there exists an infinite number of possible virtual fields that can be used, which would, in theory, ensure that all material parameters are as identifiable as possible. However, each virtual field comes with additional computational cost, so we aim to use a small number of virtual fields which probe orthogonal modes of deformation.

In this study, specimen-specific virtual displacement fields were created by assuming the entheses were surfaces with constant displacement, i.e., the bones were essentially rigid in comparison to the ligament. Mathematical descriptions of the enthesis shapes (y_i) were made by fitting 3D second-order polynomials to both sets of enthesis points,

$$y_i = \alpha_1^{(i)} X_1^2 + \alpha_2^{(i)} X_1 + \alpha_3^{(i)} X_3^2 + \alpha_4^{(i)} X_3 + \alpha_5^{(i)} X_1 X_3 + \alpha_6^{(i)} \tag{5.23}$$

where y_i is a function which models the second coordinate (X_2) of the ith set of enthesis points as a function of the other two coordinates (X_1,X_3), and the position vector $\mathbf{X} = [X_1, X_2, X_3]$ describes the coordinates in the $\mathbf{e}_1$, $\mathbf{e}_2$, and $\mathbf{e}_3$ Cartesian directions, respectively. The fit enthesis shape parameters are given by $[\alpha_1^{(i)}, \alpha_2^{(i)}, \alpha_3^{(i)}, \alpha_4^{(i)}, \alpha_5^{(i)}, \alpha_6^{(i)}]$, where $i = [1, 2]$ denotes the two entheses.

These models of the ligament-bone boundaries were used to construct the virtual fields required for the VFM. To probe different modes of deformation, four sets of virtual fields were used. They are described component-wise, where $\mathbf{u}^{*(j)} = [u_1^{*(j)}, u_2^{*(j)}, u_3^{*(j)}]$ denotes the jth virtual displacement vector field.

The first virtual field was referred to as virtual tension in the direction of the applied load ($\mathbf{e}_2$),

$$\begin{aligned} u_1^{*(1)} &= u_3^{*(1)} = 0 \\ u_2^{*(1)} &= \tfrac{X_2 - y_1}{y_2 - y_1} \Delta L \end{aligned} \tag{5.24}$$

where ΔL was defined as $0.10L$, and L was defined as the average length of the specimen ($L \equiv \overline{y_2 - y_1}$). Note that $u_2^{*(1)}$ is equal to 0 along the first enthesis boundary (y_1) and varies linearly until it is equal to ΔL along the second (y_2), both of which are functions of 3D voxel position $\mathbf{X}$. Thus, to compute the value of the cost function ϕ (Eq. 5.5) for the VFM, $u_{\partial\Omega_0}^{*(1)} = \Delta L$.

Next, a virtual Poisson contraction field in the thinnest dimension ($\mathbf{e}_3$) was constructed,

$$\begin{aligned} u_1^{*(2)} &= u_2^{*(2)} = 0 \\ u_3^{*(2)} &= \tfrac{(X_2 - y_1)(X_2 - y_2)}{L^2} X_3 \end{aligned} \tag{5.25}$$

which yields $\mathbf{u}^* = \mathbf{0}$ along y_1 and y_2, but allows for non-zero displacements in $\mathbf{e}_3$ else-

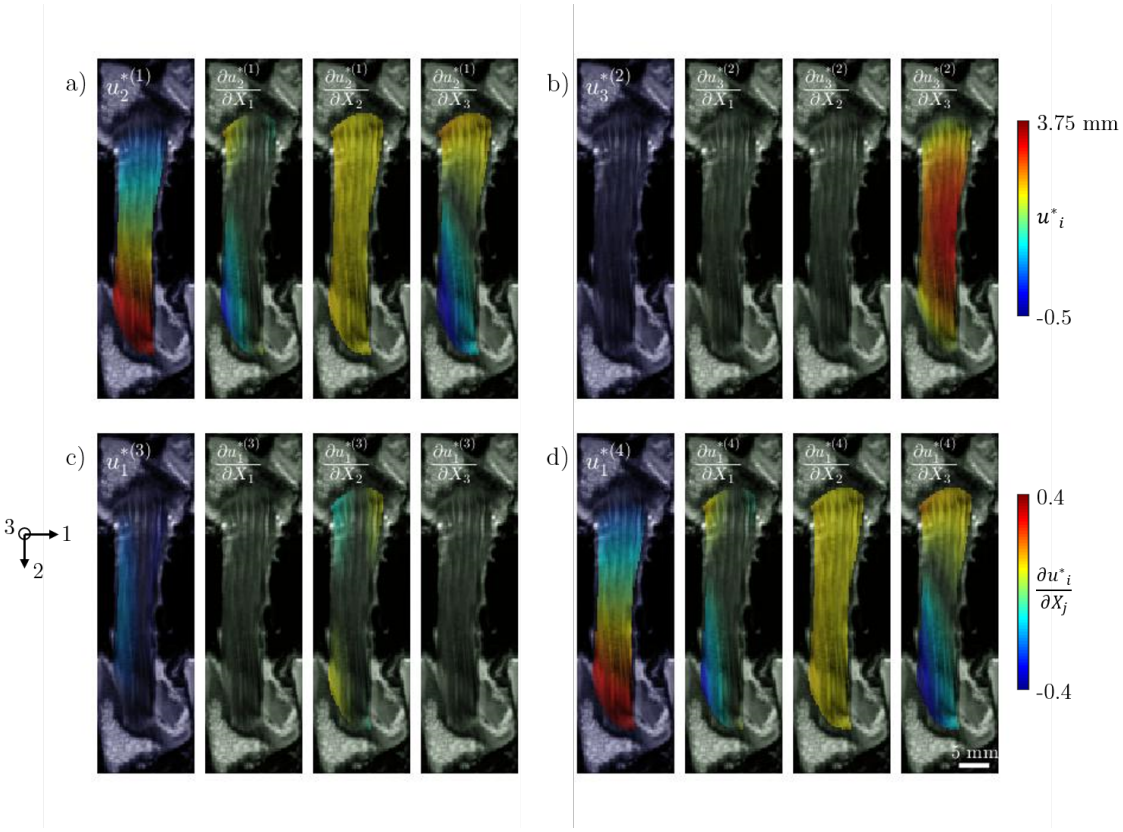

Figure 5.4: Four specimen-specific virtual fields were created using the polynomial models of the entheses described by Eq. 5.23. The four non-zero virtual displacements for each field are shown for a slice through the same AM bundle example used in Figs. 5.1-5.3, in addition to their derivatives. Virtual field 1 (a) probes the normal response in the fiber direction, fields 2 (b) and 3 (c) explore the normal response in the non-collagenous matrix, and field 4 (d) probes the material's response in shear along the fibers.

where. Similarly, the third virtual field used was virtual contraction in the thickest dimension,

$$\begin{aligned} u_2^{*(3)} &= u_3^{*(3)} = 0 \\ u_1^{*(3)} &= \tfrac{(X_2-y_1)(X_2-y_2)}{L^2} X_1. \end{aligned} \tag{5.26}$$

While virtual fields 2 and 3 both probe the normal stretch-deformation response of the isotropic phase, the experimentally measured normal Lagrange strains in the

$\mathbf{e}_2$ are typically compressive, while normal strains in $\mathbf{e}_1$ are often tensile. By using virtual fields that probe the normal response in both directions, the material model fit for the isotropic phase should consider both the compressive and tensile responses.

Finally, to probe the bulk shear response of the ligaments, a virtual shear field was introduced,

$$\begin{aligned} u_2^{*(1)} &= u_3^{*(1)} = 0 \\ u_1^{*(1)} &= \tfrac{X_2 - y_1}{y_2 - y_1} \Delta L \end{aligned} \tag{5.27}$$

where shear exists in the $\mathbf{e}_1 - \mathbf{e}_2$ plane. Note that all virtual displacements are constant along y_1 and y_2, but not zero ($u_{1\partial\Omega_0}^{*(1)} \neq 0$). However, this displacement is not in the direction of the applied load ($\mathbf{e}_2$), so it does not contribute to the external virtual work. Thus, the virtual boundary conditions for virtual fields 2-4 are $u_{\partial\Omega_0}^{*(2)} = u_{\partial\Omega_0}^{*(3)} = u_{\partial\Omega_0}^{*(4)} = 0$. The virtual fields are depicted in a slice through an example AM bundle in Fig. 5.4.

5.2.7 Statistical comparisons between groups

Best-fit parameters were found using the methods described above for each constitutive model (HGO, HGO-MAC, and tFJC) for all 15 specimens tested (5 AM bundles, 5 PL bundles, and 5 PTs). Three two-tailed t-tests with unequal variances were performed for each parameter to compare the distributions between groups: AM bundle vs. PL bundle, AM bundle vs. PT, and PL bundle vs. PT.

5.2.8 Assessment of parameter identifiability

Numerical approximation is the standard method used to solve nonlinear inverse problems such as the one presented in this work. However, because numerical solutions can be greatly influenced by experimental noise, cost function construction, and diversity of experimental data (i.e. the breadth of information the data contains), it is important to assess the identifiability of the parameters found. In the case of hyperelastic material modeling, some parameters are inherently more identifiable than others due to nature of information provided by obtainable states of deformation. For example, model predictions for states like shear, uniaxial tension/compression, or

biaxial tension/compression are largely unaffected by bulk modulus estimates. Thus, the insensitivity of the model fit to the bulk modulus estimate makes it notoriously difficult to identify [60].

To examine the identifiability each constitutive parameter, normalized sensitivity matrices (S_{ij}) were constructed for each model fit [55],

$$S_{ij} = \frac{\partial^2 \phi}{\partial \xi_i \partial \xi_j} / \min\left(\frac{\partial^2 \phi}{\partial \xi_i \partial \xi_j}\right) \tag{5.28}$$

where the diagonal element S_{ii} represents the sensitivity of the cost function (ϕ) to small perturbations in parameter ξ_i, and an off-diagonal element S_{ij} describes cost function sensitivity to paired perturbations in parameters ξ_i and ξ_j. Relatively small S_{ij} could indicate parameter covariance, if parameters' on-diagonal elements (S_{ii} and S_{jj}) are large in comparison. This means the parameters ξ_i and ξ_j are not independently identifiable – i.e., one or both are likely unnecessary. Partial derivatives were numerically estimated using small perturbations on ξ_i and ξ_j near the identified minima.

5.3 Results

Best-fit constitutive parameters for the HGO and HGO-MAC models are shown in Figs. 5.5 and 5.6, respectively, grouped by specimen type (AM bundle, PL bundle, or PT). Group mean and standard deviation for each parameter are reported in Table 5.1.

For the HGO model, the parameter κ was significantly smaller for AM bundles compared to PL bundles ($p = 0.0011$), as well as smaller for PT specimens compared to PL bundles ($p = 0.070$), although not significant at the $p < 0.05$ level. The parameter k_1 was significantly larger among PT specimens compared to PL bundles ($p = 0.047$), and larger among AM bundles compared to PL bundles, although not significant ($p = 0.12$). No significant differences were found between groups for C_{10}, B, or k_2.

The parameters found for the HGO-MAC model showed similar but not identical

	Isotropic phase			Volumetric
HGO	C_{10} (MPa)			B (kPa)
AM	1.05 ± 0.51			74.4 ± 95.5
PL	1.12 ± 0.40			23.0 ± 27.3
PT	1.38 ± 1.64			679 ± 559
HGO-MAC	C_r (MPa)	ρ_0	Λ	B (kPa)
AM	0.47 ± 0.19	0.40 ± 0.29	3.92 ± 2.35	22.9 ± 43.2
PL	0.50 ± 0.12	0.50 ± 0.93	4.48 ± 2.00	1.50 ± 0.69
PT	0.48 ± 0.17	1.57 ± 1.17	3.73 ± 1.95	36.9 ± 45.4

	Anisotropic phase		
HGO	k_1 (MPa)	k_2	κ (10^{-3})
AM	29.5 ± 13.8	2.14 ± 1.30	$9.76 \pm 4.42^{\ddagger}$
PL	$15.8 \pm 10.9^{\S}$	1.29 ± 0.70	$23.9 \pm 4.55^{\ddagger}$
PT	$31.8 \pm 10.8^{\S}$	17.1 ± 28.2	12.1 ± 10.8
HGO-MAC	k_1 (MPa)	k_2	κ (10^{-3})
AM	29.0 ± 13.8	2.04 ± 1.24	$2.29 \pm 1.41^{\dagger}$
PL	$15.0 \pm 10.6^{\S}$	1.09 ± 0.61	$6.11 \pm 3.04^{\dagger}$
PT	$31.1 \pm 11.1^{\S}$	16.9 ± 31.1	$0.54 \pm 0.44^{\dagger}$

Table 5.1: Mean and standard deviation of best fit HGO and HGO-MAC constitutive parameters for AM bundle, PL bundle, and PT groups. For the HGO model, statistically significant constitutive differences were found in κ between the AM bundle and PL bundle ($p < 0.01$) and in k_1 between the PL bundle and PT ($p < 0.05$), indicated by ‡ and §, respectively. For the HGO-MAC model, κ showed significant differences between all groups ($p < 0.05$), and k_1 was significantly larger for the PT group compared to PL bundles ($p < 0.05$). No other parameters were significantly different between groups.

trends. The parameter κ was significantly smaller for AM bundles and PT specimens compared to PL bundles ($p = 0.046$ and $p = 0.014$, respectively). Additionally, κ was significantly smaller for PT specimens compared to AM bundles ($p = 0.048$). The parameter k_1 was, again, significantly larger among PT specimens compared to PL bundles ($p = 0.046$), and larger among AM bundles compared to PL bundles, although not significant ($p = 0.11$). No significant differences were found between groups for C_r, ρ_0, Λ, B, or k_2.

Best-fit constitutive parameters for the tFJC model are displayed for each spec-

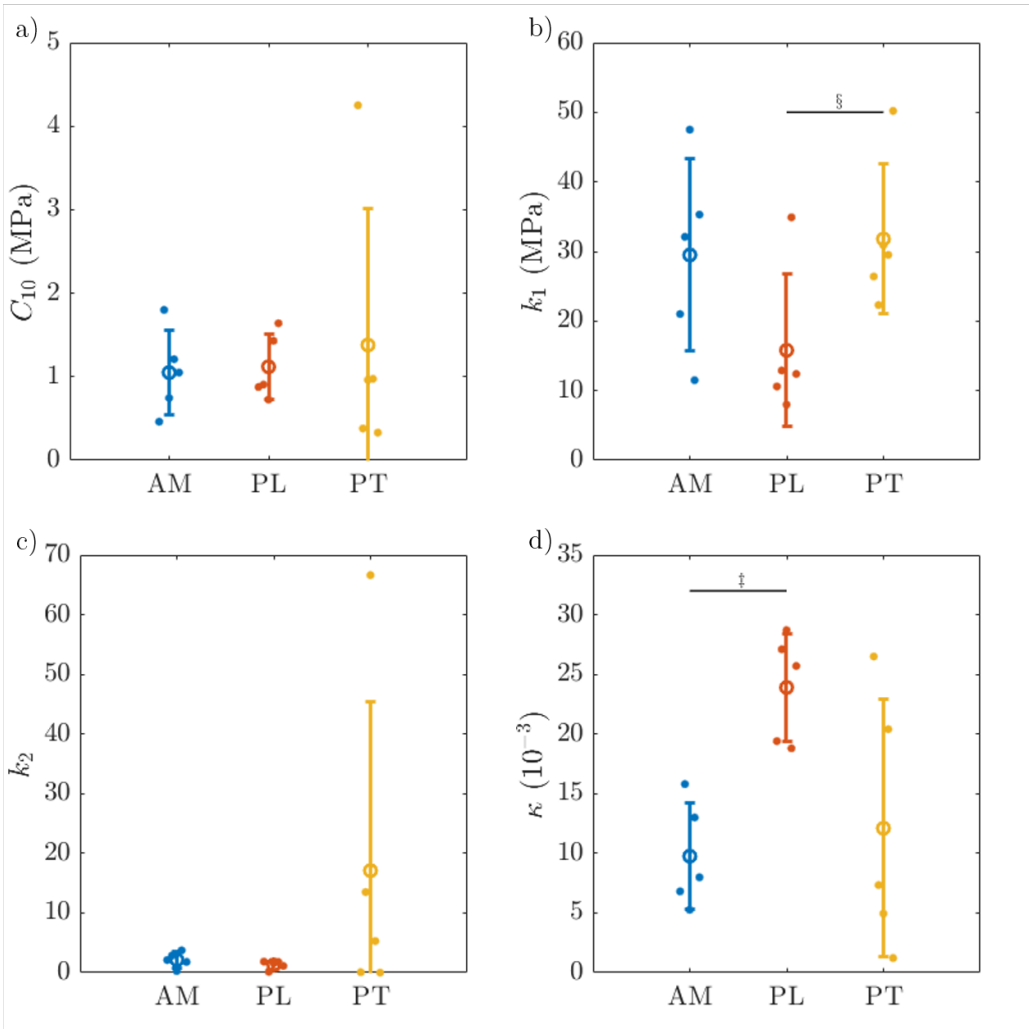

Figure 5.5: Best-fit HGO constitutive parameters for each specimen tested, grouped by specimen type (AM bundle, PL bundle, or PT). Parameters found for individual specimens are shown in filled dots. Group means for each parameter are shown in open circles and error bars represent the standard deviation. The parameter k_1 (b) was significantly larger among PT specimens compared to PL bundles ($p < 0.05$), indicated by §. Additionally, κ (d) was significantly smaller for AM bundles compared to PL bundles ($p < 0.01$), indicated by ‡. No significant differences were found between groups for C_{10} (a), k_2 (c), or B.

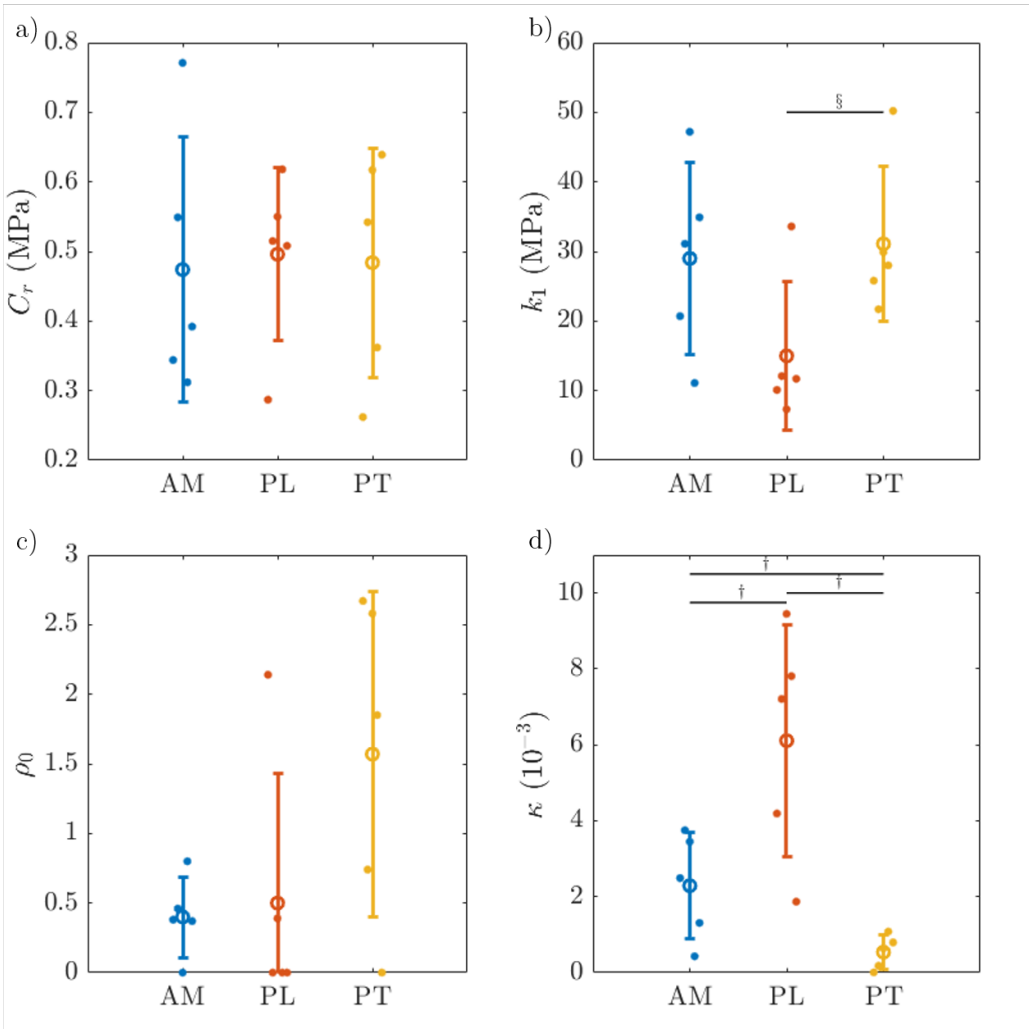

Figure 5.6: Best-fit HGO-MAC constitutive parameters for each specimen tested (shown in filled dots), grouped by specimen type. Similar to the results for the HGO model, k_1 (b) was significantly larger among PT specimens compared to PL bundles ($p < 0.05$), indicated by §. The parameter κ (d) was significantly smaller for AM bundles and PT specimens compared to PL bundles, as well as for PT specimens compared to AM bundles ($p < 0.05$), indicated by †. No significant differences were found between groups for C_r (a), ρ_0 (c), Λ, B, or k_2.

imen in Fig. 5.7, while mean and standard deviation for each specimen group are reported in Table 5.2. Parameters found for the tFJC model exhibited no significant

	Chain stiffness	RVE anisotropy		Volumetric
tFJC	C_r (MPa)	a	b	B (kPa)
AM	6.04 ± 3.06	0.17 ± 0.15	2.40 ± 0.07	117 ± 259
PL	4.01 ± 1.99	0.30 ± 0.13	2.50 ± 0.17	2.85 ± 2.33
PT	18.9 ± 13.5	0.22 ± 0.26	3.11 ± 0.79	354 ± 511

Table 5.2: Mean and standard deviation of best fit tFJC constitutive parameters for AM bundle, PL bundle, and PT groups. No parameters were significantly different between groups.

differences between groups. The parameter a tended to be smaller for AM bundles compared to PL bundles, but this difference was not significant ($p = 0.19$). Additionally, PT specimens generally had larger best-fit values for C_r and b compared to AM and PL bundles, but again, these differences were not significant: $p = 0.10$ and $p = 0.07$, respectively, for C_r, and $p = 0.11$ and $p = 0.16$ for b.

Changes to the initial conditions (i.e., initial guess for constitutive parameters, $\boldsymbol{\xi}$) did not affect the solutions, so fits appear to be unique. All solutions converged in 30 minutes to 3 hours, after $\sim$100 iterations on average, with minimum cost function values $4E-08 < \phi < 5E-06$.

A sensitivity matrix for each constitutive model is given in Table 5.3 for an example specimen (the same AM bundle shown in Figs. 5.1 and 5.3). Sensitivity matrices for other specimens followed very similar trends.

5.4 Discussion

5.4.1 Constitutive parameters indicate microstructural differences between groups

The goal of this study was to build hyperelastic constitutive models of the ovine PT and ACL bundles, while accounting for deformation heterogeneity, material direction heterogeneity, and curved displacement boundary conditions. To accomplish this, displacement-encoded MRI was used to measure full-volume deformation fields in five samples of each specimen type (AM bundle, PL bundle, and PT), each at five

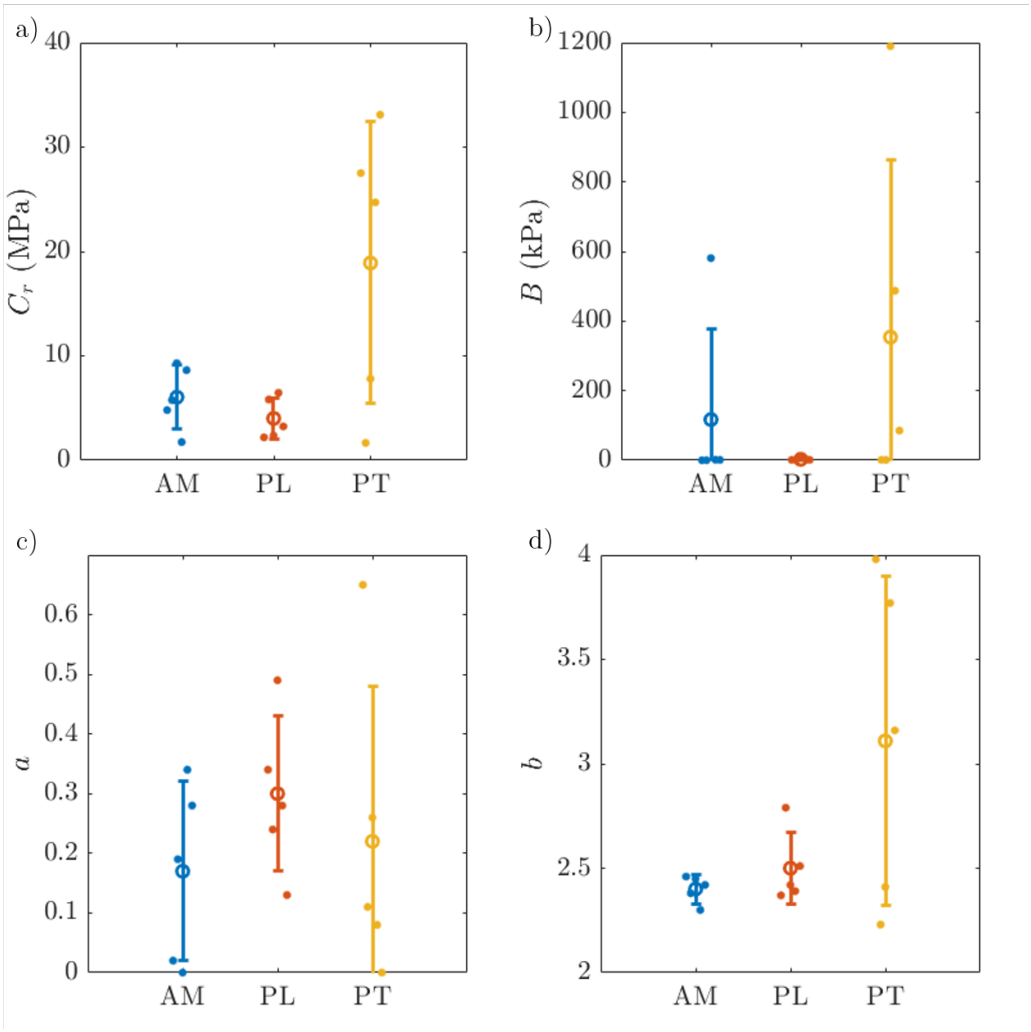

Figure 5.7: Best-fit tFJC constitutive parameters for each specimen tested (shown in filled dots), grouped by specimen type. No significant differences were found between groups for C_r (a), B (b), a (c), or b (d).

deformation states. The VFM (a full-field inverse method) was used in combination with specimen-specific descriptions of the material direction (fiber) field and enthesis boundary conditions to calibrate material models with this full-field data.

Each of the material models used in this study have constitutive parameters that describe the degree of anisotropy, or collagen fiber alignment within the ligament

HGO	C_{10}	B	k_1	k_2	κ
C_{10}	4.4E14	0	2.1E7	7.7E18	9.6E20
B		0	0	0	0
k_1			1	3.7E11	4.6E13
k_2				**1.4E23**	1.7E25
κ	sym				**2.1E27**

HGO-MAC	C_r	ρ_0	Λ	B	k_1	k_2	κ
C_r	2.5E3	6.6E5	3.0E4	5.0E1	1.4E7	3.0E6	7.4E8
ρ_0		1.7E8	7.8E6	1.3E4	3.7E9	7.9E8	1.9E11
Λ			3.6E5	6.0E2	1.7E8	3.6E7	8.8E9
B				1	2.9E5	6.0E4	1.5E7
k_1					**8.1E10**	1.7E10	4.2E12
k_2						**3.6E9**	8.9E11
κ	sym						**2.2E14**

tFJC	C_r	a	b	B
C_r	1.3E2	4.7E7	2.9E9	1.2E1
a		**1.7E13**	1.0E15	4.1E6
b			**6.4E16**	2.5E8
B	sym			1

Table 5.3: Symmetric sensitivity matrices, computed with Eq. 5.28, for the AM bundle shown in Figs. 5.1 and 5.3 indicate which parameters are most and least identifiable. The largest parameter sensitivities for each constitutive model are shown in bold text. These correspond to the parameters which are most identifiable. Sensitivity matrices for other specimens exhibited consistent trends in the relative parameter sensitivities.

material. For the HGO and HGO-MAC models, κ is a parameter ranging from 0 (perfectly aligned) to 1/3 (isotropically distributed). For the tFJC model, the parameters a and b can control the alignment of FJC chains by changing the anisotropy of the RVE; in this study, larger b and smaller a both indicate greater fiber alignment.

While most of the constitutive parameters found were consistent between groups, significantly smaller values of κ were found for the AM bundles of the ACL compared to PL bundles, for both the HGO and HGO-MAC models. This difference indicates a significantly higher degree of collagen fiber alignment in AM bundles compared to PL bundles. This result is congruent with the findings of previous studies which used birefringence measurements to detect microstructural collagen alignment differences

between the ACL bundles [140, 141]. The current study, however, is the first to detect this microstructural difference with mechanical measurements alone.

Additionally, calibrations of the HGO-MAC model found significantly smaller values of κ for PT specimens compared to both ACL bundles, which suggests that collagen fibers are more highly aligned in the PT. However, this difference was not found when the HGO model (which has a different model form for the isotropic phase) was used.

Both the HGO and HGO-MAC model found significantly larger values of k_1 for PT specimens compared to PL bundles. This suggests that either 1) collagen fibers in the PT are stiffer than those in the PL bundle, or 2) there is a larger volume fraction of type-I collagen fibers in the PT compared to the PL bundle. At least one study describes a difference in the micro-organization of collagen fibrils within collagen fibers between the ACL and PT [161]. However, other studies have found that collagen constitutes $\sim$90% of PT dry weight in humans, but $<$80% of ACL dry weight in mature rabbits [6, 86]. Still, without a same species comparison, the cause of this constitutive difference cannot be concluded.

5.4.2 Material model comparisons demonstrate the mechanical significance of non-collageneous components

Two of the constitutive models – the HGO and HGO-MAC models – had the same anisotropic phase description. The anisotropic parameters k_1 and k_2 were nearly identical between the HGO and HGO-MAC model best-fits for each specimen. However, κ decreased by 75% for the ACL bundles and 95% for the PT when the isotropic phase changed from a neo-Hookean model (HGO) to an 8-chain Macintosh model (HGO-MAC). This indicates that the calibration of κ is dependent upon the material model form used for the isotropic phase, and thus, highlights the importance of understanding the real material physics of the non-collageneous ECM.

Furthermore, whereas the HGO and HGO-MAC models have both isotropic and anisotropic phases to describe the separate mechanical contributions of the non-collageneous and collageneous ECM, respectively, the tFJC model has only one phase

which attempts to represent both. This may explain why the constitutive parameters that describe material anisotropy in the tFJC model (a and b) showed no significant differences between specimen groups. The HGO and HGO-MAC constitutive forms can calibrate the ligament mechanical response along and transverse to the collagen fiber direction independently, but these orthogonal modes of deformation are likely at odds in the calibration of the tFJC model. Nevertheless, the best-fit tFJC parameters for all specimens tested indicated a high degree of anisotropy, with b almost an order of magnitude larger than a. Additionally, trends in a suggest slightly higher degrees of collagen alignment for AM bundles and PT specimens compared to PL bundles, and a larger mean value of b for PT specimens suggest greater anisotropy compared to the ACL bundles, but these trends were not significant. However, unlike the HGO and HGO-MAC models, which showed no discernible trends in parameters unrelated to anisotropy, the tFJC parameter C_r was larger (in general) for PT specimens compared to the ACL bundles, although, again, not significant.

These results indicate that, in terms of constitutive modeling, the non-collageneous ECM is of critical importance. A better understanding of its mechanical response is necessary to build models which can adequately describe ligament material behavior.

5.4.3 Parameter identifiability

The bulk modulus (B) appears relatively unidentifiable, as was concluded in previous work [48]. It was by far the least identifiable parameter for both the HGO-MAC and tFJC models, for each of the specimens tested. The bulk modulus was entirely unidentifiable in the HGO model, meaning the cost function was completely unaffected by small changes in this parameter near the identified minima.

Importantly, κ was the most identifiable parameter for the HGO and HGO-MAC models, for all of the specimens tested. This gives added confidence to our assertion that a significant difference in collagen fiber alignment was detected between the AM and PL bundles with these methods.

It should be noted that parameter identifiability is dependent on the choice of virtual fields and the experimental data provided. Other types of mechanical tests

or other sets of virtual fields could make the cost function more sensitive to parameters that were less identifiable in this study. However, based on the methods and sensitivity analysis reported here, it does not appear that any of the material models suffered from parameter covariance.

5.4.4 Study limitations and suggestions for future work

This study has several limitations, some of which should be addressed in future work. First, the virtual displacement fields (or test functions) used were user-defined, and certainly not optimal. Methods for automatically constructing optimal virtual fields have only recently been developed, such as sensitivity-based VFM, which optimizes for parameter identifiability, or eigenfunction VFM, which extracts orthogonal sets of information [102, 103, 111]. Future work will aim to increase parameter identifiability with these techniques.

The construction of the full-volume fiber direction fields could also be improved. Local material direction was estimated based on linear interpolations from each specimen's outer edges. If local fiber direction could be estimated from anatomical images or by some other direct measurement, it could reduce the error that arises from the discrepancy between the true and estimated material direction.

It is likely that more data may have revealed more significant differences between groups. For example, k_1 was generally larger for AM bundles compared to PL bundles, but with a sample size of $n = 5$, the difference was not significant.

Additionally, the PT samples were very long ($\sim$50 mm), and extended nearly the entire length of the radio frequency (RF) coil used. This may have yielded poor signal to noise near the edges of the PT specimens, negatively affecting the results for this ligament group.

Furthermore, this study considered material nonlinearity and anisotropy. However, ligaments are also viscoelastic, meaning their response is time/history dependent. Ligament samples in this study were cyclically loaded with a square wave at 0.33 Hz. Force was monitored continuously, and continued to relax over the course of loading. Thus, the initial peak force was used in the VFM. Future work will aim

to use the complete loading history (accounting for stress relaxation) using nonlinear viscoelasticity models.

Despite the shortcomings of this work, we believe its importance should not be understated. This is the first study to use full-volume deformation measurements to characterize biological tissues with the VFM. The detection of real differences in material microstructure is indicative of the untapped potential of the techniques presented here. Future work will attempt to use these methods to characterize other tissues and detect other microstructural properties.

CHAPTER 6

Conclusions and Future Work

6.1 General conclusions

This work began with the objective of identifying the factors which most predispose an individual to ACL injury using computational mechanics models. In Chapter 2, the effect of the ACL femoral enthesis shape and attachment angle were investigated with analytical and finite element models. Three material models were fit to the same experimental data and used in the same finite element models to predict strain fields. The results suggested that the material models used were not well-calibrated; a single computational model geometry with different material descriptions (fit to the same data) yielded very different results, both locally and globally. Qualitatively, they agreed: concave enthesis shapes and more accute attachment angles likely increase effective strain concentrations in the ACL. However, quantitatively, they lacked consensus. The fidelity of computational models lies in the accuracy of their inputs, which includes a description of material behavior in the form of a constitutive model, and it was clear from the results of this work that the constitutive models were inadequate. The results also revealed that even small differences in enthesis shape created significant deformation heterogeneity, which affected the predicted global mechanical response. This suggests that enthesis geometry must be taken into account in the material modeling process.

In an effort to measure the extent of deformation heterogeneity, displacements un-

der applied loading by MRI (dualMRI) was used to measure full-volume deformation fields in ovine ACL bundles in Chapter 3. Results demonstrated that deformation in uniaxially loaded ACL bundles is far from homogeneous uniaxial tension. Large and inhomogeneous shear strains were measured throughout the volumes of all specimens tested. Additionally, positive transverse normal strains were measured that were on the order of (or larger than) the axial strain which was applied by the testing apparatus. It was hypothesized that this unexpected lateral expansion was the result of collagen fiber splay.

Collagen fibers spread, or splay, near the enthesis to minimize stress concentrations at the ligament-bone interface. In Chapter 4, analytical, computational, and experimental methods were used to examine how fiber splay affects the global mechanical response of the ACL bundles and the patellar tendon (PT), a commonly used graft ligament for ACL reconstruction. Results from all three approaches demonstrate that fiber splay creates strain heterogeneity which decreases the apparent, or grip-to-grip, tangent modulus of ligaments. This effect makes the ACL bundles appear much more compliant than the PT tendon graft, as it has considerably less fiber splay than the ACL bundles. Thus, this heterogeneity in material direction, or fiber splay, must also be accounted for in the construction of material models.

The results of Chapters 2-4 make clear that deformation heterogeneity is unavoidable in mechanically loaded ligaments. This reality invalidates the use of traditional material modeling methods, which necessitate the assumption of strain homogeneity. Thus, in Chapter 5, the lessons learned from the previous three chapters were combined to build constitutive models of the ACL bundles and PT using full-field mechanics methods. Displacement-encoded MRI was used to measure full-volume, heterogeneous deformation fields in uniaxially loaded ACL bundles and PTs, and material models were calibrated with this data using the virtual fields method (VFM). The specific methods used accounted for strain heterogeneity, material direction heterogeneity, and curved boundary conditions.

Importantly, with full-field methods, the material model calibration does not just account for these complexities; it actually benefits from them. A heterogeneous strain field contains far more information than a homogeneous one, and full-field

methods can extract this information, making more anisotropic material parameters identifiable with a single mechanical test. For the original Holzapfel-Gasser-Ogden (HGO) material model, as well as a modified version (HGO-MAC), the most identifiable constitutive parameter was κ, which describes the degree of microscopic collagen fiber alignment. Interestingly, in both models, best-fit values identified for κ were significantly larger for PL bundles compared to AM bundles, indicating more collagen fiber alignment in AM bundles, and this result is congruent with findings from other studies [140, 141].

While both the HGO and HGO-MAC models detected this microstructural difference between the ACL bundles, the values identified for κ were considerably larger for the HGO model compared to the HGO-MAC model, which indicates that the model form used for the isotropic phase can influence the fit for this anisotropic phase parameter. Little is known about the mechanical response of the ground substance, or non-collagenous ECM, so it is difficult to identify the most appropriate model choice.

The collection of work detailed throughout these chapters represents a paradigm shift in constitutive modeling of biological tissues. With the advent of full-field methods, deformation homogeneity no longer needs to be assumed when it is experimentally unachievable or impractical. The use of full-field methods to characterize the material behavior of ligaments underscored the importance of the non-collagenous ECM and detected real microstructural differences between the ACL bundles.

6.2 Suggestions for future work

Chapters 2 and 4 identified two structural properties that influence ligament deformation, but more may exist. All future work in constitutive modeling of biological tissues should be keen to recognize features which need to be considered in the modeling process. Furthermore, the methods used in Chapter 5 are far from optimal, and there are several ways to improve upon them in future work. Parameter identifiability could be enhanced for parameters that were less identifiable using sensitivity-based VFM [103] or different mechanical tests [55]. Development of methods for assessing

how well a material model can capture observed material physics would be immensely beneficial. Viscoelasticity should ultimately be introduced. Additionally, investigations should be done to discern what the requirements are for imaging factors like voxel size and magnetic field strength, so that experiments might be done more quickly, or with less expense. Finally, constitutive models which demonstrate good parameter identifiability for all parameters should be implemented in a finite element framework to study injury risk, as this work initially set out to do.

APPENDICES

APPENDIX A

Derivation and details of the analytical model of fiber splay

Consider a 2D idealized version of a ligament with flat bony attachments (entheses) and a symmetric, infinite set of fibers with curvatures in the reference configuration that can be described by a quadratic polynomial (see Fig. 4.1a). If the fibers are equally spaced at the entheses and the mid-substance, the equation for the curve of any fiber passing through x_0 (the horizontal coordinate at $y = 0$) can be described by

$$x(y) = a_f \left(y - \frac{L_0}{2} \right)^2 + \frac{w_{min}}{w_{max}} x_0 \tag{A.1}$$

where

$$a_f = \frac{4}{L_0^2} \frac{w_{max} - w_{min}}{w_{max}} x_0. \tag{A.2}$$

L_0 is the length of the whole ligament in its reference configuration, w_{max} is the average width of the entheses, and w_{min} is the width at the mid-substance. The apparent tangent modulus (the slope of the macroscopic stress-strain curve) of this idealized ligament in the y-direction is desired.

We assume that a fiber does not hold any load until straightened, meaning the fibers are not connected (i.e. the ligament has no shear stiffness) and that they also have no bending stiffness. In other words, the force held by a given fiber, f, is

zero if the current macroscopic length of the ligament is less than that of the fiber's contour length in the reference configuration, L_f. The fiber's force-strain relationship is assumed to be linear once straightened,

$$f(\lambda, x_0) = \begin{cases} E\left(\frac{\lambda L_0 - L_f(x_0)}{L_f(x_0)}\right), & -x_{lim} \leq x_0 \leq x_{lim} \\ 0, & \text{otherwise} \end{cases} \tag{A.3}$$

where E is the elastic modulus of the fiber, λ is the macroscopic ligament stretch, and $[-x_{lim}, x_{lim}]$ describe the set of engaged fibers (see Fig. 4.1b). The fiber contour length can be computed from Eqs. A.1 and A.2,

$$L_f(x_0) = \int_0^{L_0} \sqrt{\frac{dx}{dy}^2 + 1} dy = \frac{L_0}{2}\sqrt{a_f^2 L_0^2 + 1} + \frac{\text{arcsinh}\left(a_f L_0\right)}{2a_f} \tag{A.4}$$

and simplified using a Taylor series approximation,

$$L_f(x_0) \approx L_0 + \frac{8}{3L_0}\left(\frac{w_{max} - w_{min}}{w_{max}}\right)^2 x_0^2. \tag{A.5}$$

The boundaries between engaged and unengaged fibers were found by solving $\lambda L_0 = L_f(x_0)$ for x_0, using Eq. A.5,

$$\pm x_{lim}(\lambda) = \pm\frac{\sqrt{6}}{4}\frac{L_0 w_{max}}{w_{max} - w_{min}}\sqrt{\lambda - 1}. \tag{A.6}$$

Now that the force contribution from individual fibers (Eq. A.3) and the limit between engaged and unengaged fibers (Eq. A.6) are known, the total force exerted by the ligament for a given stretch is computed by integrating f over $[-x_{lim}$,$x_{lim}]$,

$$F(\lambda) = E\int_{-x_{lim}(\lambda)}^{x_{lim}(\lambda)} \frac{(\lambda L_0 - L_f(x_0))}{L_f(x_0)} dx_0. \tag{A.7}$$

The apparent, or average, stress per unit thickness is defined as

$$\bar{\sigma}(\lambda) = \frac{F(\lambda)}{w_{min}} \tag{A.8}$$

and thus, the apparent modulus of the ligament is

$$\bar{E} = \frac{d\bar{\sigma}}{d\lambda} = \frac{1}{w_{min}} \frac{dF}{d\lambda}. \tag{A.9}$$

Whereas Eq. A.7 is difficult to solve analytically, its derivative in Eq. A.9 can readily be solved using Leibniz's integral rule to yield

$$\frac{\bar{E}}{E} = \frac{\sqrt{6}}{2} \frac{L_0}{(w_{max} - w_{min})} \frac{w_{max}}{w_{min}} \arctan(\sqrt{\lambda - 1}) \tag{A.10}$$

for $1 \leq \lambda \leq \frac{2}{3}(\frac{w_{max} - w_{min}}{L_0})^2 + 1$. Thus, for a given macroscopic stretch (λ) and true elastic modulus (E), a ligament with splayed fibers will have an apparent tangent modulus proportional to

$$\bar{E} \propto \frac{L_0}{(w_{max} - w_{min})} \frac{w_{max}}{w_{min}}. \tag{A.11}$$

This quantity describes the influence of splay-related dimensions on the apparent tangent modulus of the ligament, so it is referred to as the splay ratio. For context, the splay ratio will approach infinity as collagen fibers become perfectly aligned, with no fiber splay.

To visualize the effect of the splay ratio on the macroscopic response of the PT and ACL regions, the fraction of engaged fibers and non-dimensional apparent stress were computed for the average dimensions of each ligament of interest (Table 4.1) as a function of macroscopic stretch. An equation for the fraction of engaged fibers was derived directly from Eq. A.6,

$$p_e = \begin{cases} \frac{2x_{lim}}{w_{max}} = \frac{\sqrt{6}}{2} \frac{L_0}{w_{max} - w_{min}} \sqrt{\lambda - 1}, & \text{if } 1 \leq \lambda \leq \lambda_{lim} \\ 1, & \lambda > \lambda_{lim} \end{cases} \tag{A.12}$$

where λ_{lim} is the stretch limit for full fiber engagement, $\lambda_{lim} = \frac{2}{3}(\frac{w_{max}-w_{min}}{L_0})^2 + 1$. The non-dimensional apparent stress was derived using Eqs. A.9 and A.10,

$$\frac{\bar{\sigma}}{E} = \int_1^{\lambda} E(\lambda)d\lambda = \frac{\sqrt{6}}{2}\frac{L_0}{w_{max}-w_{min}}\frac{w_{max}}{w_{min}}\int_1^{\lambda}\arctan(\sqrt{\lambda-1})d\lambda \tag{A.13}$$

with a small angle approximation for $\sqrt{\lambda-1}$,

$$\frac{\bar{\sigma}}{E} = \begin{cases} \frac{\sqrt{6}}{3}\frac{L_0}{w_{max}-w_{min}}(\lambda-1)^{3/2}, & \text{if } 1 \le \lambda \le \lambda_{lim} \\ \left(\frac{4}{9}\frac{w_{max}}{w_{min}} - \frac{2}{3}\right)\left(\frac{w_{max}-w_{min}}{L_0}\right)^2 + \lambda - 1, & \lambda > \lambda_{lim}. \end{cases} \tag{A.14}$$

It should be noted that the stretch limit for full fiber engagement, λ_{lim}, is quite small for the ligaments described in Table 4.1 (< 1.01). Due to the assumption of linear elastic fibers, the apparent modulus of the analytical model becomes equal to the true modulus past full engagement. In reality, collagen fibers exhibit nonlinear behavior, so the inhomogeneity in fiber stretch would affect the macroscopic response past this limit. Thus, the splay ratio was used in the analysis of the experimental and computational data collected at finite strain. The use of the splay ratio for data beyond full fiber engagement is discussed in greater detail in the Discussion section.

BIBLIOGRAPHY

BIBLIOGRAPHY

[1] Hussein S Abdul-Rahman, Munther A Gdeisat, David R Burton, Michael J Lalor, Francis Lilley, and Christopher J Moore. Fast and robust three-dimensional best path phase unwrapping algorithm. *Applied optics*, 46(26): 6623–6635, 2007.

[2] Julie Agel, Todd Rockwood, and David Klossner. Collegiate acl injury rates across 15 sports: national collegiate athletic association injury surveillance system data update (2004-2005 through 2012-2013). *Clinical journal of sport medicine*, 26(6):518–523, 2016.

[3] Carlos Adrian Vargas Aguilera. ndnanfilter.m. *MATLAB Central File Exchange*, 2020.

[4] Eduard Alentorn-Geli, Gregory D Myer, Holly J Silvers, Gonzalo Samitier, Daniel Romero, Cristina Lázaro-Haro, and Ramón Cugat. Prevention of non-contact anterior cruciate ligament injuries in soccer players. part 2: a review of prevention programs aimed to modify risk factors and to reduce injury rates. *Knee surgery, sports traumatology, arthroscopy*, 17(8):859–879, 2009.

[5] Eduard Alentorn-Geli, Xavier Pelfort, Felipe Mingo, Xavier Lizano-Díez, Joan Leal-Blanquet, Raúl Torres-Claramunt, Pedro Hinarejos, Lluís Puig-Verdié, and Joan Carles Monllau. An evaluation of the association between radiographic intercondylar notch narrowing and anterior cruciate ligament injury in men: the notch angle is a better parameter than notch width. *Arthroscopy: The Journal of Arthroscopic & Related Surgery*, 31(10):2004–2013, 2015.

[6] David Amiel, Scott D Kuiper, C Douglas Wallace, Frederick L Harwood, and Jerry S Vandeberg. Age-related properties of medial collateral ligament and anterior cruciate ligament: a morphologic and collagen maturation study in the rabbit. *Journal of gerontology*, 46(4):B159–B165, 1991.

[7] Andrew A Amis. The functions of the fibre bundles of the anterior cruciate ligament in anterior drawer, rotational laxity and the pivot shift. *Knee surgery, sports traumatology, arthroscopy*, 20(4):613–620, 2012.

[8] Allen F Anderson, David C Dome, Shiva Gautam, Mark H Awh, and Gregory W Rennirt. Correlation of anthropometric measurements, strength, anterior cruciate ligament size, and intercondylar notch characteristics to sex differences in anterior cruciate ligament tear rates. *The American journal of sports medicine*, 29(1):58–66, 2001.

[9] Afshin Anssari-Benam, Kirsten Legerlotz, Dan L Bader, and Hazel RC Screen. On the specimen length dependency of tensile mechanical properties in soft tissues: gripping effects and the characteristic decay length. *Journal of biomechanics*, 45(14):2481, 2012.

[10] CL Ardern, S Sonesson, M Forssblad, and J Kvist. Comparison of patient-reported outcomes among those who chose acl reconstruction or non-surgical treatment. *Scandinavian journal of medicine & science in sports*, 27(5):535–544, 2017.

[11] Clare L Ardern, Nicholas F Taylor, Julian A Feller, and Kate E Webster. Return-to-sport outcomes at 2 to 7 years after anterior cruciate ligament reconstruction surgery. *The American journal of sports medicine*, 40(1):41–48, 2012.

[12] Clare L Ardern, Joanna Kvist, and Kate E Webster. Psychological aspects of anterior cruciate ligament injuries. *Operative Techniques in Sports Medicine*, 24(1):77–83, 2016.

[13] RGC Arridge and MJ Folkes. Effect of sample geometry on the measurement of mechanical properties of anisotropic materials. *Polymer*, 17(6):495–500, 1976.

[14] Ellen M Arruda and Mary C Boyce. A three-dimensional constitutive model for the large stretch behavior of rubber elastic materials. *Journal of the Mechanics and Physics of Solids*, 41(2):389–412, 1993.

[15] Theresa S Atkinson, Benjamin J Ewers, and Roger C Haut. The tensile and stress relaxation responses of human patellar tendon varies with specimen cross-sectional area. *Journal of biomechanics*, 32(9):907–914, 1999.

[16] Stéphane Avril, Pierre Badel, and Ambroise Duprey. Anisotropic and hyperelastic identification of in vitro human arteries from full-field optical measurements. *Journal of biomechanics*, 43(15):2978–2985, 2010.

[17] Björn Barenius, Sari Ponzer, Adel Shalabi, Robert Bujak, Louise Norlén, and Karl Eriksson. Increased risk of osteoarthritis after anterior cruciate ligament reconstruction: a 14-year follow-up study of a randomized controlled trial. *The American journal of sports medicine*, 42(5):1049–1057, 2014.

[18] Mélanie L Beaulieu. *On the Fatigue Life of the Human Anterior Cruciate Ligament: Experimental Studies of the Effects of Limited Internal Femoral Rotation and Microscopic Entheseal Anatomy.* PhD thesis, 2015.

[19] Mélanie L Beaulieu, Grace E Carey, Stephen H Schlecht, Edward M Wojtys, and James A Ashton-Miller. Quantitative comparison of the microscopic anatomy of the human acl femoral and tibial entheses. *Journal of Orthopaedic Research*, 33(12):1811–1817, 2015.

[20] Mélanie L Beaulieu, Edward M Wojtys, and James A Ashton-Miller. Risk of anterior cruciate ligament fatigue failure is increased by limited internal femoral rotation during in vitro repeated pivot landings. *The American Journal of Sports Medicine*, 43(9):2233–2241, 2015.

[21] Mélanie L Beaulieu, Grace E Carey, Stephen H Schlecht, Edward M Wojtys, and James A Ashton-Miller. On the heterogeneity of the femoral enthesis of the human acl: microscopic anatomy and clinical implications. *Journal of experimental orthopaedics*, 3(1):1–9, 2016.

[22] Bruce D Beynnon, John S Hall, Daniel R Sturnick, Mike J DeSarno, Mack Gardner-Morse, Timothy W Tourville, Helen C Smith, James R Slauterbeck, Sandra J Shultz, Robert J Johnson, et al. Increased slope of the lateral tibial plateau subchondral bone is associated with greater risk of noncontact acl injury in females but not in males: a prospective cohort study with a nested, matched case-control analysis. *The American journal of sports medicine*, 42 (5):1039–1048, 2014.

[23] JE Bischoff, EA Arruda, and K Grosh. A microstructurally based orthotropic hyperelastic constitutive law. *Journal of Applied Mechanics*, 69(5):570–579, 2002.

[24] Katherine M Bojicic, Mélanie L Beaulieu, Daniel Y Imaizumi Krieger, James A Ashton-Miller, and Edward M Wojtys. Association between lateral posterior tibial slope, body mass index, and acl injury risk. *Orthopaedic Journal of Sports Medicine*, 5(2):2325967116688664, 2017.

[25] KA Bonilla, AM Pardes, BR Freedman, and LJ Soslowsky. Supraspinatus tendons have different mechanical properties across sex. *Journal of biomechanical engineering*, 141(1):011002, 2019.

[26] Theodoros Bouras, Peter Fennema, Stephen Burke, and Hilary Bosman. Stenotic intercondylar notch type is correlated with anterior cruciate ligament injury in female patients using magnetic resonance imaging. *Knee Surgery, Sports Traumatology, Arthroscopy*, 26(4):1252–1257, 2018.

[27] Henry E Bourke, Lucy J Salmon, Alison Waller, Victoria Patterson, and Leo A Pinczewski. Survival of the anterior cruciate ligament graft and the contralateral acl at a minimum of 15 years. *The American journal of sports medicine*, 40(9):1985–1992, 2012.

[28] Mark L Brandon, Paul T Haynes, Joel R Bonamo, MaryIrene I Flynn, Gene R Barrett, and Mark F Sherman. The association between posterior-inferior tibial slope and anterior cruciate ligament insufficiency. *Arthroscopy: The Journal of Arthroscopic & Related Surgery*, 22(8):894–899, 2006.

[29] Thomas D Brown, Richard C Johnston, Charles L Saltzman, J Lawrence Marsh, and Joseph A Buckwalter. Posttraumatic osteoarthritis: a first estimate of incidence, prevalence, and burden of disease. *Journal of orthopaedic trauma*, 20(10):739–744, 2006.

[30] David L Butler, Matthew D Kay, and Donald C Stouffer. Comparison of material properties in fascicle-bone units from human patellar tendon and knee ligaments. *Journal of biomechanics*, 19(6):425–432, 1986.

[31] David L Butler, Edward S Grood, Frank R Noyes, Marvin L Olmstead, R Bruce Hohn, Steven P Arnoczky, and Mark G Siegel. Mechanical properties of primate vascularized vs. nonvascularized patellar tendon grafts; changes over time. *Journal of orthopaedic research*, 7(1):68–79, 1989.

[32] Ryan M Castile, Nathan W Skelley, Behzad Babaei, Robert H Brophy, and Spencer P Lake. Microstructural properties and mechanics vary between bundles of the human anterior cruciate ligament during stress-relaxation. *Journal of biomechanics*, 49(1):87–93, 2016.

[33] Ji Hyeon Cha, Sang Hoon Lee, Myung Jin Shin, Byeong Kyoo Choi, and Sung Il Bin. Relationship between mucoid hypertrophy of the anterior cruciate ligament (acl) and morphologic change of the intercondylar notch: Mri and arthroscopy correlation. *Skeletal radiology*, 37(9):821–826, 2008.

[34] Deva D Chan and Corey P Neu. Transient and microscale deformations and strains measured under exogenous loading by noninvasive magnetic resonance. *PloS one*, 7(3):e33463, 2012.

[35] Deva D Chan and Corey P Neu. Intervertebral disc internal deformation measured by displacements under applied loading with mri at 3t. *Magnetic resonance in medicine*, 71(3):1231–1237, 2014.

[36] Deva D Chan, David Toribio, and Corey P Neu. Displacement smoothing for the precise mri-based measurement of strain in soft biological tissues. *Computer methods in biomechanics and biomedical engineering*, 16(8):852–860, 2013.

[37] Deva D Chan, Luyao Cai, Kent D Butz, Stephen B Trippel, Eric A Nauman, and Corey P Neu. In vivo articular cartilage deformation: noninvasive quantification of intratissue strain during joint contact in the human knee. *Scientific reports*, 6, 2016.

[38] Naveen Chandrashekar, James Slauterbeck, and Javad Hashemi. Sex-based differences in the anthropometric characteristics of the anterior cruciate ligament and its relation to intercondylar notch geometry a cadaveric study. *The American journal of sports medicine*, 33(10):1492–1498, 2005.

[39] Naveen Chandrashekar, Hossein Mansouri, James Slauterbeck, and Javad Hashemi. Sex-based differences in the tensile properties of the human anterior cruciate ligament. *Journal of biomechanics*, 39(16):2943–2950, 2006.

[40] Naveen Chandrashekar, Javad Hashemi, James Slauterbeck, and Bruce D Beynnon. Low-load behaviour of the patellar tendon graft and its relevance to the biomechanics of the reconstructed knee. *Clinical Biomechanics*, 23(7): 918–925, 2008.

[41] Ajit M Chaudhari and Thomas P Andriacchi. The mechanical consequences of dynamic frontal plane limb alignment for non-contact acl injury. *Journal of biomechanics*, 39(2):330–338, 2006.

[42] Rita S Chorba, David J Chorba, Lucinda E Bouillon, Corey A Overmyer, and James A Landis. Use of a functional movement screening tool to determine injury risk in female collegiate athletes. *North American journal of sports physical therapy: NAJSPT*, 5(2):47, 2010.

[43] Ming-Jay Chow, Raphaël Turcotte, Charles P Lin, and Yanhang Zhang. Arterial extracellular matrix: a mechanobiological study of the contributions and interactions of elastin and collagen. *Biophysical journal*, 106(12):2684–2692, 2014.

[44] A Cohen. A padé approximant to the inverse langevin function. *Rheologica acta*, 30(3):270–273, 1991.

[45] Michael I Danto and Savio L-Y Woo. The mechanical properties of skeletally mature rabbit anterior cruciate ligament and patellar tendon over a range of strain rates. *Journal of Orthopaedic Research*, 11(1):58–67, 1993.

[46] Sina David, Igor Komnik, Markus Peters, Johannes Funken, and Wolfgang Potthast. Identification and risk estimation of movement strategies during cutting maneuvers. *Journal of Science and Medicine in Sport*, 2017.

[47] Marcin Domzalski, Piotr Grzelak, and Peter Gabos. Risk factors for anterior cruciate ligament injury in skeletally immature patients: analysis of intercondylar notch width using magnetic resonance imaging. *International orthopaedics*, 34(5):703–707, 2010.

[48] Jonathan B Estrada, Callan M Luetkemeyer, Ulrich M Scheven, and Ellen M Arruda. Mr-u: material characterization using 3d displacement-encoded magnetic resonance and the virtual fields method. *Experimental Mechanics*.

[49] Yuan Feng, Chung-Hao Lee, Lining Sun, Songbai Ji, and Xuefeng Zhao. Characterizing white matter tissue in large strain via asymmetric indentation and inverse finite element modeling. *Journal of the mechanical behavior of biomedical materials*, 65:490–501, 2017.

[50] AS Fox, J Bonacci, SG McLean, and N Saunders. Efficacy of acl injury risk screening methods in identifying high-risk landing patterns during a sport-specific task. *Scandinavian journal of medicine & science in sports*, 27(5): 525–534, 2017.

[51] Peter Fratzl. Collagen: structure and mechanics, an introduction. In *Collagen*, pages 1–13. Springer, 2008.

[52] T Christian Gasser, Ray W Ogden, and Gerhard A Holzapfel. Hyperelastic modelling of arterial layers with distributed collagen fibre orientations. *Journal of the royal society interface*, 3(6):15–35, 2006.

[53] Ruben Gatt, Michelle Vella Wood, Alfred Gatt, Francis Zarb, Cynthia Formosa, Keith M Azzopardi, Aaron Casha, Tonio P Agius, Pierre Schembri-Wismayer, Lucienne Attard, et al. Negative poisson's ratios in tendons: an unexpected mechanical response. *Acta biomaterialia*, 24:201–208, 2015.

[54] Richard M Goldstein, Howard A Zebker, and Charles L Werner. Satellite radar interferometry: Two-dimensional phase unwrapping. *Radio science*, 23 (4):713–720, 1988.

[55] SN Grama, SJ Subramanian, and F Pierron. On the identifiability of anand visco-plastic model parameters using the virtual fields method. *Acta Materialia*, 86:118–136, 2015.

[56] Michel Grédiac and Fabrice Pierron. Identifying constitutive parameters from heterogeneous strain fields using the virtual fields method. *Procedia IUTAM*, 4:48–53, 2012.

[57] Michel Grediac, Fabrice Pierron, Stéphane Avril, and Evelyne Toussaint. The virtual fields method for extracting constitutive parameters from full-field measurements: a review. *Strain*, 42(4):233–253, 2006.

[58] Letha Y Griffin, Marjorie J Albohm, Elizabeth A Arendt, Roald Bahr, Bruce D Beynnon, Marlene DeMaio, Randall W Dick, Lars Engebretsen, William E Garrett, Jo A Hannafin, et al. Understanding and preventing noncontact anterior cruciate ligament injuries a review of the hunt valley ii meeting, january 2005. *The American journal of sports medicine*, 34(9):1512–1532, 2006.

[59] Rachel B Groves, Sion A Coulman, James C Birchall, and Sam L Evans. An anisotropic, hyperelastic model for skin: experimental measurements, finite element modelling and identification of parameters for human and murine skin. *Journal of the mechanical behavior of biomedical materials*, 18:167–180, 2013.

[60] Stefan Hartmann and Rose Rogin Gilbert. Identifiability of material parameters in solid mechanics. *Archive of Applied Mechanics*, 88(1-2):3–26, 2018.

[61] Javad Hashemi, Naveen Chandrashekar, Hossein Mansouri, James R Slauterbeck, and Daniel M Hardy. The human anterior cruciate ligament: sex differences in ultrastructure and correlation with biomechanical properties. *Journal of orthopaedic research*, 26(7):945–950, 2008.

[62] Javad Hashemi, Naveen Chandrashekar, Hossein Mansouri, Brian Gill, James R Slauterbeck, Robert C Schutt, Eugene Dabezies, and Bruce D Beynnon. Shallow medial tibial plateau and steep medial and lateral tibial slopes new risk factors for anterior cruciate ligament injuries. *The American journal of sports medicine*, 38(1):54–62, 2010.

[63] David Hawkins, Corey Lum, Diane Gaydos, and Russell Dunning. Dynamic creep and pre-conditioning of the achilles tendon in-vivo. *Journal of biomechanics*, 42(16):2813–2817, 2009.

[64] Heath B Henninger, Clayton J Underwood, Steven J Romney, Grant L Davis, and Jeffrey A Weiss. Effect of elastin digestion on the quasi-static tensile response of medial collateral ligament. *Journal of Orthopaedic Research*, 31 (8):1226–1233, 2013.

[65] Heath B Henninger, William R Valdez, Sara A Scott, and Jeffrey A Weiss. Elastin governs the mechanical response of medial collateral ligament under shear and transverse tensile loading. *Acta Biomaterialia*, 25(1):304–312, 2015.

[66] Heath B Henninger, William R Valdez, Sara A Scott, and Jeffrey A Weiss. Elastin governs the mechanical response of medial collateral ligament under shear and transverse tensile loading. *Acta biomaterialia*, 25:304–312, 2015.

[67] Mackenzie M Herzog, Stephen W Marshall, Jennifer L Lund, Virginia Pate, and Jeffrey T Spang. Cost of outpatient arthroscopic anterior cruciate ligament reconstruction among commercially insured patients in the united states, 2005-2013. *Orthopaedic journal of sports medicine*, 5(1):2325967116684776, 2017.

[68] Timothy E Hewett, Gregory D Myer, Kevin R Ford, Robert S Heidt, Angelo J Colosimo, Scott G McLean, Antonie J Van den Bogert, Mark V Paterno, and Paul Succop. Biomechanical measures of neuromuscular control and valgus loading of the knee predict anterior cruciate ligament injury risk in female athletes a prospective study. *The American Journal of Sports Medicine*, 33(4): 492–501, 2005.

[69] Timothy E Hewett, Kevin R Ford, Yingying Y Xu, Jane Khoury, and Gregory D Myer. Utilization of acl injury biomechanical and neuromuscular risk profile analysis to determine the effectiveness of neuromuscular training. *The American journal of sports medicine*, 44(12):3146–3151, 2016.

[70] GA Holzapfel, Gasser TC, and Ray W Ogden. A new constitutive framework for arterial wall mechanics and a comparative study of material models. *Journal of Elasticity*, 61(1-3):1–48, 2000.

[71] Gerhard A Holzapfel, Thomas C Gasser, and Ray W Ogden. A new constitutive framework for arterial wall mechanics and a comparative study of material models. *Journal of elasticity and the physical science of solids*, 61(1-3):1–48, 2000.

[72] Cornelius O Horgan. On saint-venant's principle in plane anisotropic elasticity. *Journal of Elasticity*, 2(3):169–180, 1972.

[73] Cornelius O Horgan. Some remarks on saint-venant's principle for transversely isotropic composites. *Journal of Elasticity*, 2(4):335–339, 1972.

[74] Cornelius O Horgan. Saint-venant end effects in composites. *Journal of Composite Materials*, 16(5):411–422, 1982.

[75] Chun-Yuh Huang, Vincent M Wang, Robert J Pawluk, John S Bucchieri, William N Levine, Louis U Bigliani, Van C Mow, and Evan L Flatow. Inhomogeneous mechanical behavior of the human supraspinatus tendon under uniaxial loading. *Journal of orthopaedic research*, 23(4):924–930, 2005.

[76] Patrick Ienny, Anne-Sophie Caro-Bretelle, and Emmanuel Pagnacco. Identification from measurements of mechanical fields by finite element model updating strategies: a review. *European Journal of Computational Mechanics/Revue Européenne de Mécanique Numérique*, 18(3-4):353–376, 2009.

[77] Lauren E Imwalle, Gregory D Myer, Kevin R Ford, and Timothy E Hewett. Relationship between hip and knee kinematics in athletic women during cutting maneuvers: a possible link to noncontact anterior cruciate ligament injury and prevention. *Journal of strength and conditioning research/National Strength & Conditioning Association*, 23(8):2223, 2009.

[78] Victoria L Johnson, Justin P Roe, Lucy J Salmon, Leo A Pinczewski, and David J Hunter. Does age influence the risk of incident knee osteoarthritis

after a traumatic anterior cruciate ligament injury? *The American journal of sports medicine*, 44(9):2399–2405, 2016.

[79] J Kastelic, I Palley, and E Baer. A structural mechanical model for tendon crimping. *Journal of biomechanics*, 13(10):887–893, 1980.

[80] MA Kessler, H Behrend, Samuel Henz, G Stutz, A Rukavina, and MS Kuster. Function, osteoarthritis and activity after acl-rupture: 11 years follow-up results of conservative versus reconstructive treatment. *Knee Surgery, Sports Traumatology, Arthroscopy*, 16(5):442–448, 2008.

[81] Mohammad Shahnawaz Khan, Jong Keun Seon, and Eun Kyoo Song. Risk factors for anterior cruciate ligament injury: assessment of tibial plateau anatomic variables on conventional mri using a new combined method. *International orthopaedics*, 35(8):1251–1256, 2011.

[82] Michael Kjær. Role of extracellular matrix in adaptation of tendon and skeletal muscle to mechanical loading. *Physiological reviews*, 84(2):649–698, 2004.

[83] Tron Krosshaug, Atsuo Nakamae, Barry P Boden, Lars Engebretsen, Gerald Smith, James R Slauterbeck, Timothy E Hewett, and Roald Bahr. Mechanisms of anterior cruciate ligament injury in basketball video analysis of 39 cases. *The American Journal of Sports Medicine*, 35(3):359–367, 2007.

[84] Michael P Leathers, Alexa Merz, Jeffrey Wong, Trevor Scott, Jeffrey C Wang, and Sharon L Hame. Trends and demographics in anterior cruciate ligament reconstruction in the united states. *Journal of Knee Surgery*, 28(05):390–394, 2015.

[85] Kirsten Legerlotz, Graham P Riley, and Hazel RC Screen. Specimen dimensions influence the measurement of material properties in tendon fascicles. *Journal of biomechanics*, 43(12):2274–2280, 2010.

[86] Jennifer K LeMoine, Jonah D Lee, and Todd A Trappe. Impact of sex and chronic resistance training on human patellar tendon dry mass, collagen content, and collagen cross-linking. *American Journal of Physiology-Regulatory, Integrative and Comparative Physiology*, 296(1):R119–R124, 2009.

[87] Mari Leppänen, Kati Pasanen, Urho M Kujala, Tommi Vasankari, Pekka Kannus, Sami Äyrämö, Tron Krosshaug, Roald Bahr, Janne Avela, Jarmo Perttunen, et al. Stiff landings are associated with increased acl injury risk in

young female basketball and floorball players. *The American journal of sports medicine*, 45(2):386–393, 2017.

[88] James G Levins, Erin C Argentieri, Daniel R Sturnick, Mack Gardner-Morse, Pamela M Vacek, Timothy W Tourville, Robert J Johnson, James R Slauterbeck, and Bruce D Beynnon. Geometric characteristics of the knee are associated with a noncontact acl injury to the contralateral knee after unilateral acl injury in young female athletes. *The American journal of sports medicine*, 45 (14):3223–3232, 2017.

[89] Toby Leys, Lucy Salmon, Alison Waller, James Linklater, and Leo Pinczewski. Clinical results and risk factors for reinjury 15 years after anterior cruciate ligament reconstruction: a prospective study of hamstring and patellar tendon grafts. *The American journal of sports medicine*, 40(3):595–605, 2012.

[90] David B Lipps, Edward M Wojtys, and James A Ashton-Miller. Anterior cruciate ligament fatigue failures in knees subjected to repeated simulated pivot landings. *The American journal of sports medicine*, page 0363546513477836, 2013.

[91] L Stefan Lohmander, P Martin Englund, Ludvig L Dahl, and Ewa M Roos. The long-term consequence of anterior cruciate ligament and meniscus injuries osteoarthritis. *The American journal of sports medicine*, 35(10):1756–1769, 2007.

[92] Stephen Lombardo, Paul M Sethi, and Chad Starkey. Intercondylar notch stenosis is not a risk factor for anterior cruciate ligament tears in professional male basketball players an 11-year prospective study. *The American journal of sports medicine*, 33(1):29–34, 2005.

[93] Callan M Luetkemeyer, Luyao Cai, Corey P Neu, and Ellen M Arruda. Full-volume displacement mapping of anterior cruciate ligament bundles with dualmri. *Extreme Mechanics Letters*, 19:7–14, 2018.

[94] Callan M Luetkemeyer, Benjamin C Marchi, James A Ashton-Miller, and Ellen M Arruda. Femoral entheseal shape and attachment angle as potential risk factors for anterior cruciate ligament injury. *Journal of the mechanical behavior of biomedical materials*, 88:313–321, 2018.

[95] Thomas Luyckx, Matthias Verstraete, Karel De Roo, Catherine Van Der Straeten, and Jan Victor. High strains near femoral insertion site of the

superficial medial collateral ligament of the knee can explain the clinical failure pattern. *Journal of Orthopaedic Research*, 34(11):2016–2024, 2016.

[96] Nathan A Mall, Peter N Chalmers, Mario Moric, Miho J Tanaka, Brian J Cole, Bernard R Bach Jr, and George A Paletta Jr. Incidence and trends of anterior cruciate ligament reconstruction in the united states. *The American journal of sports medicine*, 42(10):2363–2370, 2014.

[97] Kaitlyn F Mallett and Ellen M Arruda. Digital image correlation-aided mechanical characterization of the anteromedial and posterolateral bundles of the anterior cruciate ligament. *Acta biomaterialia*, 56:44–57, 2017.

[98] Benjamin Marchi. *Soft Tissue Constitutive Forms and Their Implications for Whole Knee Computational Models*. PhD thesis, 2017.

[99] Benjamin C Marchi and Ellen M Arruda. A study on the role of articular cartilage soft tissue constitutive form in models of whole knee biomechanics. *Biomechanics and modeling in mechanobiology*, 16(1):117–138, 2017.

[100] Benjamin C Marchi, Callan M. Luetkemeyer, and Ellen M Arruda. Evaluating continuum level descriptions of the medial collateral ligament. *International Journal of Solids and Structures*, In Press, 2018.

[101] Benjamin C Marchi, Callan M Luetkemeyer, and Ellen M Arruda. Evaluating continuum level descriptions of the medial collateral ligament. *International journal of solids and structures*, 138:245–263, 2018.

[102] Aleksander Marek, Frances M Davis, and Fabrice Pierron. Sensitivity-based virtual fields for the non-linear virtual fields method. *Computational Mechanics*, 60(3):409–431, 2017.

[103] Aleksander Marek, Frances M Davis, Marco Rossi, and Fabrice Pierron. Extension of the sensitivity-based virtual fields to large deformation anisotropic plasticity. *International Journal of Material Forming*, 12(3):457–476, 2019.

[104] JMP Martins, A Andrade-Campos, and S Thuillier. Comparison of inverse identification strategies for constitutive mechanical models using full-field measurements. *International Journal of Mechanical Sciences*, 145:330–345, 2018.

[105] Scott G McLean, Kaitlyn F Mallett, and Ellen M Arruda. Deconstructing the anterior cruciate ligament: What we know and do not know about function,

material properties, and injury mechanics. *Journal of Biomechanical Engineering*, 137(2):020906, 2015.

[106] Rupert Meller, Elmar Willbold, Eric Hesse, Beatrix Dreymann, Michael Fehr, Carl Haasper, Christof Hurschler, Christian Krettek, and Frank Witte. Histologic and biomechanical analysis of anterior cruciate ligament graft to bone healing in skeletally immature sheep. *Arthroscopy: The Journal of Arthroscopic & Related Surgery*, 24(11):1221–1231, 2008.

[107] Eric G Meyer, Timothy G Baumer, Jill M Slade, Walter E Smith, and Roger C Haut. Tibiofemoral contact pressures and osteochondral microtrauma during anterior cruciate ligament rupture due to excessive compressive loading and internal torque of the human knee. *The American journal of sports medicine*, 36(10):1966–1977, 2008.

[108] Marco Milella, Maria Giovanna Belcastro, Christoph PE Zollikofer, and Valentina Mariotti. The effect of age, sex, and physical activity on entheseal morphology in a contemporary italian skeletal collection. *American Journal of Physical Anthropology*, 148(3):379–388, 2012.

[109] Corey P Neu and Jeffrey H Walton. Displacement encoding for the measurement of cartilage deformation. *Magnetic resonance in medicine*, 59(1):149–155, 2008.

[110] TD Nguyen and BL Boyce. An inverse finite element method for determining the anisotropic properties of the cornea. *Biomechanics and modeling in mechanobiology*, 10(3):323–337, 2011.

[111] N Nigamaa and SJ Subramanian. Identification of orthotropic elastic constants using the eigenfunction virtual fields method. *International Journal of Solids and Structures*, 51(2):295–304, 2014.

[112] FRANK R Noyes and EDWARD S Grood. The strength of the anterior cruciate ligament in humans and rhesus monkeys. *The Journal of Bone & Joint Surgery*, 58(8):1074–1082, 1976.

[113] Britt Elin Øiestad, Inger Holm, Lars Engebretsen, and May Arna Risberg. The association between radiographic knee osteoarthritis and knee symptoms, function and quality of life 10–15 years after anterior cruciate ligament reconstruction. *British journal of sports medicine*, 45(7):583–588, 2011.

[114] Xiao Ouyang, Yu Hao Wang, Jian Wang, Shi Dong Hong, Feng Xin, Lin Wang, Xiao Wei Yang, Jing Rong Wang, Li Ming Wang, Bo Wei, et al. Mri measurement on intercondylar notch after anterior cruciate ligament rupture and its correlation. *Experimental and therapeutic medicine*, 11(4):1275–1278, 2016.

[115] Thomas D O'Brien, Neil D Reeves, Vasilios Baltzopoulos, David A Jones, and Constantinos N Maganaris. Mechanical properties of the patellar tendon in adults and children. *Journal of biomechanics*, 43(6):1190–1195, 2010.

[116] NJ Pagano and JC Halpin. Influence of end constraint in the testing of anisotropic bodies. In *Mechanics of Composite Materials*, pages 2–16. Springer, 1994.

[117] Bing Pan, Kemao Qian, Huimin Xie, and Anand Asundi. Two-dimensional digital image correlation for in-plane displacement and strain measurement: a review. *Measurement science and technology*, 20(6):062001, 2009.

[118] Xin Pang, Jian-Ping Wu, Garry T Allison, Jiake Xu, Jonas Rubenson, Ming-Hao Zheng, David G Lloyd, Bruce Gardiner, Allan Wang, and Thomas Brett Kirk. Three dimensional microstructural network of elastin, collagen, and cells in achilles tendons. *Journal of Orthopaedic Research*, 35(6):1203–1214, 2017.

[119] Ioanna Papathanasiou, Sotirios Michalitsis, Michael E Hantes, Marianna Vlychou, Lydia Anastasopoulou, Konstantinos N Malizos, and Aspasia Tsezou. Molecular changes indicative of cartilage degeneration and osteoarthritis development in patients with anterior cruciate ligament injury. *BMC musculoskeletal disorders*, 17(1):21, 2016.

[120] AM Pardes, BR Freedman, GW Fryhofer, NS Salka, PR Bhatt, and LJ Soslowsky. Males have inferior achilles tendon material properties compared to females in a rodent model. *Annals of biomedical engineering*, 44(10): 2901–2910, 2016.

[121] Hyung-Soon Park, Chulhyun Ahn, David T Fung, Yupeng Ren, and Li-Qun Zhang. A knee-specific finite element analysis of the human anterior cruciate ligament impingement against the femoral intercondylar notch. *Journal of biomechanics*, 43(10):2039–2042, 2010.

[122] Abby E Peters, Riaz Akhtar, Eithne J Comerford, and Karl T Bates. Tissue material properties and computational modelling of the human tibiofemoral joint: a critical review. *PeerJ*, 6:e4298, 2018.

[123] Fabrice Pierron and Michel Grédiac. *The virtual fields method: extracting constitutive mechanical parameters from full-field deformation measurements*. Springer Science & Business Media, 2012.

[124] Chadwick C Prodromos, Yung Han, Julie Rogowski, Brian Joyce, and Kelvin Shi. A meta-analysis of the incidence of anterior cruciate ligament tears as a function of gender, sport, and a knee injury–reduction regimen. *Arthroscopy: The Journal of Arthroscopic & Related Surgery*, 23(12):1320–1325, 2007.

[125] Benedikt L Proffen, Megan McElfresh, Braden C Fleming, and Martha M Murray. A comparative anatomical study of the human knee and six animal species. *The Knee*, 19(4):493–499, 2012.

[126] Nattawit Promma, Bumedijen Raka, Michel Grediac, Evelyne Toussaint, J-B Le Cam, Xavier Balandraud, and François Hild. Application of the virtual fields method to mechanical characterization of elastomeric materials. *International Journal of Solids and Structures*, 46(3-4):698–715, 2009.

[127] KM Quapp and JA Weiss. Material characterization of human medial collateral ligament. *Journal of Biomechanical Engineering*, 120(6):757–763, 1998.

[128] WJP Radford, AA Amis, and AC Stead. The ovine stifle as a model for human cruciate ligament surgery. *Veterinary and Comparative Orthopaedics and Traumatology*, 9(03):134–9, 1996.

[129] A Redaelli, S Vesentini, M Soncini, P Vena, S Mantero, and FM Montevecchi. Possible role of decorin glycosaminoglycans in fibril to fibril force transfer in relative mature tendons—a computational study from molecular to microstructural level. *Journal of biomechanics*, 36(10):1555–1569, 2003.

[130] Aapo Ristaniemi, Lauri Stenroth, Santtu Mikkonen, and Rami K Korhonen. Comparison of elastic, viscoelastic and failure tensile material properties of knee ligaments and patellar tendon. *Journal of biomechanics*, 79:31–38, 2018.

[131] Bryant C Roberts, Egon Perilli, and Karen J Reynolds. Application of the digital volume correlation technique for the measurement of displacement and strain fields in bone: a literature review. *Journal of biomechanics*, 47(5):923–934, 2014.

[132] L Schatzmann, P Brunner, and HU Stäubli. Effect of cyclic preconditioning on the tensile properties of human quadriceps tendons and patellar ligaments. *Knee Surgery, Sports Traumatology, Arthroscopy*, 6(1):S56–S61, 1998.

[133] Ulrich M Scheven, Jonathan B Estrada, Callan M Luetkemeyer, and Ellen M Arruda. Robust high resolution strain imaging by alternating pulsed field gradient stimulated echo imaging (apgstei) at 7 tesla. *Journal of Magnetic Resonance*, 310:106620, 2020.

[134] Stephen H Schlecht. Understanding entheses: bridging the gap between clinical and anthropological perspectives. *The Anatomical Record*, 295(8):1239–1251, 2012.

[135] Hazel RC Screen, David E Berk, Karl E Kadler, Francesco Ramirez, and Marian F Young. Tendon functional extracellular matrix. *Journal of Orthopaedic Research*, 33(6):793–799, 2015.

[136] Padmanabhan Seshaiyer and Jay D Humphrey. A sub-domain inverse finite element characterization of hyperelastic membranes including soft tissues. *Journal of biomechanical engineering*, 125(3):363–371, 2003.

[137] Behzad Seyfi, Nasser Fatouraee, and Milad Imeni. Mechanical modeling and characterization of meniscus tissue using flat punch indentation and inverse finite element method. *Journal of the Mechanical Behavior of Biomedical Materials*, 77:337–346, 2018.

[138] RA Simon, JS Everhart, HN Nagaraja, and AM Chaudhari. A case-control study of anterior cruciate ligament volume, tibial plateau slopes and intercondylar notch dimensions in acl-injured knees. *Journal of biomechanics*, 43 (9):1702–1707, 2010.

[139] Neeraj Singh. International epidemiology of anterior cruciate ligament injuries. *Orthopedic Res Online J*, 1, 2018.

[140] Nathan W Skelley, Ryan M Castile, Timothy E York, Viktor Gruev, Spencer P Lake, and Robert H Brophy. Differences in the microstructural properties of the anteromedial and posterolateral bundles of the anterior cruciate ligament. *The American journal of sports medicine*, 43(4):928–936, 2015.

[141] Nathan W Skelley, Ryan M Castile, Paul C Cannon, Christian I Weber, Robert H Brophy, and Spencer P Lake. Regional variation in the mechanical and microstructural properties of the human anterior cruciate ligament. *The American journal of sports medicine*, 44(11):2892–2899, 2016.

[142] Jess G Snedeker and Jasper Foolen. Tendon injury and repair–a perspective on the basic mechanisms of tendon disease and future clinical therapy. *Acta biomaterialia*, 2017.

[143] Kurt P Spindler and Rick W Wright. Anterior cruciate ligament tear. *New England Journal of Medicine*, 359(20):2135–2142, 2008.

[144] Manon Sterba, Carl-Éric Aubin, Eric Wagnac, Leo Fradet, and Pierre-Jean Arnoux. Effect of impact velocity and ligament mechanical properties on lumbar spine injuries in posterior-anterior impact loading conditions: a finite element study. *Medical & biological engineering & computing*, 57(6):1381–1392, 2019.

[145] Lazar Stijak, Richard F Herzog, and Pascal Schai. Is there an influence of the tibial slope of the lateral condyle on the acl lesion? *Knee surgery, sports traumatology, arthroscopy*, 16(2):112–117, 2008.

[146] Daniel R Sturnick, Pamela M Vacek, Michael J DeSarno, Mack G Gardner-Morse, Timothy W Tourville, James R Slauterbeck, Robert J Johnson, Sandra J Shultz, and Bruce D Beynnon. Combined anatomic factors predicting risk of anterior cruciate ligament injury for males and females. *The American journal of sports medicine*, 43(4):839–847, 2015.

[147] Dai Sugimoto, Gregory D Myer, Kim D Barber Foss, and Timothy E Hewett. Specific exercise effects of preventive neuromuscular training intervention on anterior cruciate ligament injury risk reduction in young females: meta-analysis and subgroup analysis. *Br J Sports Med*, pages bjsports–2014, 2014.

[148] David M Swenson, Christy L Collins, Thomas M Best, David C Flanigan, Sarah K Fields, and R Dawn Comstock. Epidemiology of knee injuries among us high school athletes, 2005/06–2010/11. *Medicine and science in sports and exercise*, 45(3):462, 2013.

[149] Spencer E Szczesny, John M Peloquin, Daniel H Cortes, Jennifer A Kadlowec, Louis J Soslowsky, and Dawn M Elliott. Biaxial tensile testing and constitutive modeling of human supraspinatus tendon. *Journal of biomechanical engineering*, 134(2):021004, 2012.

[150] Chavaunne T Thorpe, Helen L Birch, Peter D Clegg, and Hazel RC Screen. The role of the non-collagenous matrix in tendon function. *International journal of experimental pathology*, 94(4):248–259, 2013.

[151] Lisa Tibor, Priscilla H Chan, Tadashi T Funahashi, Ronald Wyatt, Gregory B Maletis, and Maria CS Inacio. Surgical technique trends in primary acl reconstruction from 2007 to 2014. *JBJS*, 98(13):1079–1089, 2016.

[152] Michael S Todd, Steve Lalliss, and E'Stephan Garcia. The relationship between posterior tibial slope and anterior cruciate ligament injuries. *The American journal of sports medicine*, 38(1):63–67, 2010.

[153] Pamela M Vacek, James R Slauterbeck, Timothy W Tourville, Daniel R Sturnick, Leigh-Ann Holterman, Helen C Smith, Sandra J Shultz, Robert J Johnson, Kelly J Tourville, and Bruce D Beynnon. Multivariate analysis of the risk factors for first-time noncontact acl injury in high school and college athletes: a prospective cohort study with a nested, matched case-control analysis. *The American journal of sports medicine*, 44(6):1492–1501, 2016.

[154] Floor M van Diek, Megan R Wolf, Christopher D Murawski, Carola F van Eck, and Freddie H Fu. Knee morphology and risk factors for developing an anterior cruciate ligament rupture: an mri comparison between acl-ruptured and non-injured knees. *Knee Surgery, Sports Traumatology, Arthroscopy*, 22 (5):987–994, 2014.

[155] Rachel V Vitali, Stephen M Cain, Ryan S McGinnis, Antonia M Zaferiou, Lauro V Ojeda, Steven P Davidson, and Noel C Perkins. Method for estimating three-dimensional knee rotations using two inertial measurement units: Validation with a coordinate measurement machine. *Sensors*, 17(9):1970, 2017.

[156] Sharon HA Vrooijink, Femke Wolters, Carola F Van Eck, and Freddie H Fu. Measurements of knee morphometrics using mri and arthroscopy: a comparative study between acl-injured and non-injured subjects. *Knee Surgery, Sports Traumatology, Arthroscopy*, 19(1):12–16, 2011.

[157] Frederick K Weitz, Petri J Sillanpää, and Ville M Mattila. The incidence of paediatric acl injury is increasing in finland. *Knee Surgery, Sports Traumatology, Arthroscopy*, pages 1–6, 2019.

[158] Brian C Werner, Scott Yang, Austin M Looney, and Frank Winston Gwathmey. Trends in pediatric and adolescent anterior cruciate ligament injury and reconstruction. *Journal of Pediatric Orthopaedics*, 36(5):447–452, 2016.

[159] Darryl C Whitney, Daniel R Sturnick, Pamela M Vacek, Mike J DeSarno, Mack Gardner-Morse, Timothy W Tourville, Helen C Smith, James R Slauterbeck,

Robert J Johnson, Sandra J Shultz, et al. Relationship between the risk of suffering a first-time noncontact acl injury and geometry of the femoral notch and acl: a prospective cohort study with a nested case-control analysis. *The American journal of sports medicine*, 42(8):1796–1805, 2014.

[160] SL-Y Woo, GA Johnson, and BA Smith. Mathematical modeling of ligaments and tendons. 1993.

[161] L-H Yahia and G Drouin. Microscopical investigation of canine anterior cruciate ligament and patellar tendon: collagen fascicle morphology and architecture. *Journal of Orthopaedic Research*, 7(2):243–251, 1989.

[162] Kyoko Yoshida, Mala Mahendroo, Joy Vink, Ronald Wapner, and Kristin Myers. Material properties of mouse cervical tissue in normal gestation. *Acta biomaterialia*, 36:195–209, 2016.

[163] Thore Zantop, Peter U Brucker, Armando Vidal, Boris A Zelle, and Freddie H Fu. Intraarticular rupture pattern of the acl. *Clinical orthopaedics and related research*, 454:48–53, 2007.

[164] David Zbrojkiewicz, Christopher Vertullo, and Jane E Grayson. Increasing rates of anterior cruciate ligament reconstruction in young australians, 2000–2015. *Medical Journal of Australia*, 208(8):354–358, 2018.